

MEASUREMENT AND MODELING OF THE TWO-POINT CORRELATION
TENSOR IN A PLANE WAKE FOR BROADBAND NOISE PREDICTION

Report to NASA Langley under grant NAG 1-1942
Technical Monitors: C. L. Burley and T F Brooks

William J. Devenport, Chittiappa Muthanna and Roulong Ma,
Department of Aerospace and Ocean Engineering,
Virginia Tech, 215 Randolph Hall, Blacksburg VA 24061.
Tel. (540) 231 4456 Email: devenport@aoe.vt.edu

Stewart A. L. Glegg,
Department of Ocean Engineering,
Florida Atlantic University, Boca Raton, FL 33431

Report VPI-AOE-263
May 1999

ERRATA: July 2001

Due to a programming error figures 29 through 38, parts (b) and (c) were inadvertently plotted with the sign of the w velocity component reversed. These figures should be interpreted with this in mind

The same error would have affected output from the subroutine *corrn.m* (i.e. reversing the sign of uw and vw correlations returned) distributed with the zip file containing the two-point data and Matlab programs. This zip file (available at <http://www.aoe.vt.edu/flowdata>) has now been amended to eliminate this error.

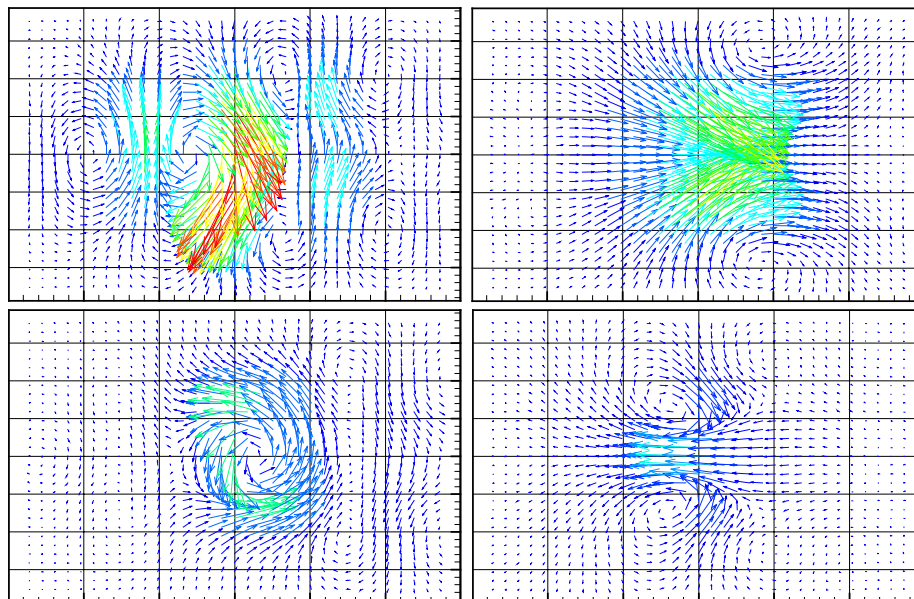
MEASUREMENT AND MODELING OF THE TWO-POINT CORRELATION TENSOR IN A PLANE WAKE FOR BROADBAND NOISE PREDICTION

Report to NASA Langley under grant NAG 1-1942
Technical Monitors: C. L. Burley and T F Brooks

William J. Devenport, Chittiappa Muthanna and Roulong Ma,
Department of Aerospace and Ocean Engineering,
Virginia Tech, 215 Randolph Hall, Blacksburg VA 24061.
Tel. (540) 231 4456 Email: devenport@aoe.vt.edu

Stewart A. L. Glegg,
Department of Ocean Engineering,
Florida Atlantic University, Boca Raton, FL 33431

Report VPI-AOE-263
May 1999



ABSTRACT

Single and two-point turbulence measurements have been made in the plane turbulent wake of momentum thickness Reynolds number 3060 shed from a NACA 0012 airfoil at zero angle of attack. The single point measurements reveal the evolution of the wake to a fully developed state and its symmetry and two dimensionality. They also show the wake to be similar to the fully developed flows of previous studies. The two-point measurements, made in the fully developed region, provide a complete description of the 4-dimensional two-point correlation tensor of the wake. A compact representation of this function, suitable for use in aeroacoustic calculations, is made publicly available. These data can be used to determine the upwash space-time correlation function seen by any blade cutting the wake on any path. We demonstrate that they can also be used to estimate the space-time correlations produced by distorted wakes. The data also allow examination of the 'characteristic eddies' of the turbulence through proper orthogonal decomposition and linear stochastic estimation.

A simple generic technique has been developed to extrapolate the correlation tensor function from the Reynolds stress field based upon the hypothesis that its form is largely determined by the constraints imposed by inhomogeneity and continuity. Estimates for the plane wake compare favorably with measurements and, interestingly, proper orthogonal modes and characteristic eddy structures inferred from the estimates are similar to those obtained from measurements.

CONTENTS

1. INTRODUCTION	5
2. APPARATUS AND INSTRUMENTATION	7
3. COORDINATE SYSTEM, TEST CONDITIONS	9
4. SINGLE-POINT TURBULENCE MEASUREMENTS	10
<i>4.1 Test Matrix</i>	10
<i>4.2 Data Availability</i>	10
<i>4.3 Results and discussion</i>	11
5. TWO-POINT TURBULENCE MEASUREMENTS	15
<i>5.1 Test Matrix</i>	15
<i>5.2 Data Reduction</i>	16
<i>5.3 Data availability</i>	20
<i>5.4 Example applications using the data</i>	21
<i>5.5 Further applications</i>	22
<i>5.6 Results and discussion</i>	23
<u>5.6.1 Form of the correlation tensor function</u>	24
<u>5.6.2 Characteristic eddy decomposition</u>	26
<u>5.6.3 Estimation of correlation functions for a curved wake</u>	30

6. MODELING OF THE TWO-POINT CORRELATION TENSOR FUNCTION	33
<i>6.1 Introduction</i>	33
<i>6.2 Form of q_{ln} for homogeneous turbulence</i>	35
<i>6.3 Relationship to Proper Orthogonal Decomposition</i>	38
<i>6.4 Modeling approach and application to the wake flow</i>	40
<i>6.5 Results and discussion</i>	41
7. CONCLUSIONS	43
8. REFERENCES	46
TABLE 1	50
FIGURES	

1. INTRODUCTION

The motivation behind the present work is the desire for a more realistic representation of turbulence for use in computing broadband noise resulting from blade-wake interactions in helicopter rotors, stator-wake interactions in large aspect ratio aircraft engines, and similar situations. Such calculations (e.g. Amiet, 1975, Glegg *et al.*, 1997, Glegg 1998) require the two-point space time correlation of the upwash velocity component seen by the lifting surface. Since this information is not generally available the turbulence is usually assumed to behave as though it were homogenous and isotropic and von Karman's interpolation formula or a similar function is used. In a series of measurements (see Devenport *et al.*, 1998, Devenport *et al.*, 1997, Wittmer *et al.*, 1997, Wenger *et al.*, 1998), we have established that the upwash correlation function in several wake flows is actually quite different than that implied by von Karman's interpolation. The form of the correlation function is dominated by the anisotropy and inhomogeneity visible in the mean flow, and its expression in the large eddy structure of the turbulence. Devenport *et al.* (1998) show that these differences can have a significant effect on the broadband noise generated.

The investigation described in this report has involved experimental and theoretical studies aimed at more providing more realistic representations of the correlation function for wake flows. Experiments have been performed to measure the complete two-point space-time correlation tensor of the fully-developed plane turbulent wake formed downstream of an airfoil. Along with single-point measurements of velocity statistics and spectra, these data have been analyzed to reveal, as far as possible, the important turbulence structure of the wake from the point of view of broadband noise

prediction. Particular attention is paid to the proper orthogonal modes (Lumley, 1967) of the wake since, as demonstrated by Glegg and Devenport (1997), these provide the rigorously correct description of an inhomogeneous turbulence for broadband noise calculations. The correlation measurements have also been reduced to the form of a MATLAB[®] function that could be directly incorporated into aeroacoustic calculation methods. (This function, along with the rest of the measurements and codes used in the present investigation are available over the Internet at <http://www.aoe.vt.edu/flowdata>.) With aeroacoustic calculations in mind we show that this plane wake data can be used to estimate the space time correlation function of a distorted wake, by taking a distorted path through the correlation function. Such estimates are not exact – one is ignoring the effects of wake stretching, curvature, interaction etc. upon the turbulence – but are significantly more realistic than assuming homogeneous isotropic turbulence.

The theoretical component of the present investigations has involved the development of a generic modeling technique for extrapolating the two-point correlation tensor function purely from Reynolds stress data. Such techniques are needed to couple aeroacoustic calculations to RANS calculations. The present approach is based on the hypothesis that much of the form of the correlation function is a direct result of the inhomogeneity of the turbulence field coupled with the constraints of continuity. The simplest viable model consistent with this hypothesis has been developed and applied to the wake flow. The model reproduces many of the key features of the measured correlation function including the proper orthogonal modes and their associated flow patterns. Given that the model is not ‘tuned’ to the wake flow – (indeed it could be used to estimate the correlation function of any turbulent flow for which the Reynolds stress

field is known and a length scale can be estimated) – this result suggests that our hypothesis is sound. The form of the model permits the inclusion of flow-specific information if greater accuracy is desired.

This report is divided into sections describing the experimental apparatus (§2), coordinate system and test conditions (§3), single point wake measurements (§4), two-point correlation measurements (§5), theoretical modeling (§6), and conclusions (§7).

2. APPARATUS AND INSTRUMENTATION

Measurements were made in the 0.610×0.914×6.10m test section of the Virginia Tech 3×2 Low Speed Wind Tunnel (figure 1). The empty test section of this tunnel, 0.610m high and 0.914m wide, produces a low turbulence (<0.2%), closely uniform flow with near zero streamwise pressure gradient, see Engel (1995). Tapered fillets installed in the corners of the wind tunnel test section eliminate most of the streamwise pressure gradient associated with boundary layer growth. Figure 2 shows the streamwise pressure distribution in the empty test section.

A NACA 0012 airfoil, 0.203m in chord, was mounted at the mid height of the test section, at zero sweep and zero angle of attack, with its leading edge 1.524m downstream of the test section entrance (figure 1). A distributed roughness trip, consisting of 0.5mm-diameter glass welding beads glued in a random pattern at a density of approximately 200beads/cm² covering the first 40% of the chordlength of the airfoil, was used to generate relatively high Reynolds number turbulent boundary layers on both sides of the airfoil. The wake of the airfoil, allowed to develop unhindered over the remainder of the test section length, is the subject of the present investigation.

Single and two-point turbulence measurements were made in the wake using Auspex Corp. miniature four-sensor hot-wire probe, type AVOP-4-100 (figure 3). This type of probe, consisting of two orthogonal X-wire arrays, was chosen because it is capable of simultaneous three-component measurements from a relatively compact (0.5mm^3) measurement volume. It also overcomes some of the gradient error problems associated with a standard triple-wire probe in trailing vortex flows (see Wittmer, 1996, and Wittmer *et al.*, 1998). Sensors were operated using Dantec 56C17/56C01 anemometer units (matched frequency response better than 20 kHz) interfaced to an IBM AT compatible computer using an Analogic 12 bit HSDAS-12 analog-to-digital converter and a series of buck and gain amplifiers of calibrated frequency response.

Probes were calibrated separately for velocity and angle response. Velocity calibrations were performed frequently using King's law to correlate the wire output voltages with the cooling velocities. Angle calibrations were performed periodically using the direct method of Wittmer *et al.* (1998) which involves placing the probe in the potential core of a uniform jet and pitching and yawing over all likely flow angle combinations from $+45^\circ$ to -45° .

Since measurement of the two-point correlation tensor involves the measurement of the cross-spectrum tensor between the velocity fluctuations at pairs of points over a broad range of frequencies, it is essential that the dynamic response of the individual sensors on each probe, and the response of the sensors on the different probes be closely matched. To observe the dynamic response, calibrations were performed for each sensor and its associated electronics using a pulsed YAG laser. The sensor was placed in a flow with the same velocity as the wind tunnel free stream, and illuminated by the laser, which produces nano-second-long pulses at a rate of about 10Hz. The electrical output from the

corresponding anemometer bridge, which reveals the impulse response of the system, was recorded using a Rapid Systems R2000 8-bit 20Msample/sec A/D converter system. Impulse response curves, phase aligned using the trigger signal from the laser, were averaged over many realizations and then Fourier transformed to reveal the amplitude and phase response characteristics. It was found through this process that the strongest factor controlling the form of the (otherwise optimized) frequency response was the length of the probe cables. By choosing the cable lengths the amplitude and phase response characteristics shown in figure 5 were obtained. Note the flat amplitude and well matched phase response characteristics, out to well beyond 20KHz - more than sufficient for the present turbulence measurement which showed little energy beyond about 13kHz.

A two-axis computer controlled traverse gear was used to position one of the four-sensor probes in the test section. For the two-point measurements, the second four-sensor probe was held using an unmotorized support. Previous studies by Miranda (1996) suggest that interference between the probes would have been minimal, even for very close probe spacings. This conclusion is supported by the results of the present measurements.

3. COORDINATE SYSTEM, TEST CONDITIONS

Figure 1 shows the coordinate system used in presenting results. Coordinate x is measured downstream along the test-section axis from the airfoil leading edge, coordinate y is measured downward from the chordline of the airfoil and therefore the wake centerline, and coordinate z is measured in the spanwise direction from the center of the test section so as to complete a right handed system. Mean and fluctuating velocity

components (U, V, W) and (u, v, w) are defined in the directions (x, y, z) respectively. Distances are often normalized on the wing chord c equal to 8". Velocities are often normalized on the approach free-stream velocity U_e , sensed using a Pitot-static probe located near the corner of the test section close to its upstream end. Throughout the measurements, this velocity was set to $27.4\text{m/s} \pm 1\%$, corresponding to a chord Reynolds number of $339000 \pm 2\%$.

4. SINGLE-POINT TURBULENCE MEASUREMENTS

4.1 Test Matrix

Single-point velocity and turbulence measurements were made in y -profiles through the wake on the tunnel centerline at 18 streamwise locations extending from $x/c=1.67$ to 12.07. All mean-velocity, Reynolds stress and triple-product components were measured. At selected locations three-component spectra of velocity fluctuations were also measured. The purpose of these measurements was to document the statistical and spectral properties of the wake and their evolution to a fully developed state. At one station within the fully developed region, $x/c=9.34$, a full cross-section of single-point measurements were made to verify the two-dimensionality of the wake. Uncertainty estimates for single-point measurements are presented in table 1.

4.2 Data Availability

All measurements presented in this section are available in numerical form over the World Wide Web at <http://www.aoe.vt.edu/flowdata>.

4.2 Results and discussion

The mean axial (x -wise) velocity profile of a plane turbulent wake typically has the Gaussian-like form shown schematically in figure 5. This profile is used to define the local wake length and velocity scales at a particular x station. The velocity scale U_w is taken as the centerline axial velocity deficit. The half-wake width L_w is defined as the distance from the centerline to the point where the axial velocity deficit is half its centerline value. The wake momentum thickness θ is defined as $\theta \equiv \int_{-\infty}^{\infty} \frac{U}{U_e} \left(1 - \frac{U}{U_e}\right) dy$ and should be constant with respect to streamwise distance since it is directly related to the drag coefficient on the airfoil, $C_d = 2\theta/c$. Figure 6 shows the streamwise evolution of U_w/U_e , L_w/c and θ/c , determined from the measured mean velocity profiles, as functions of the distance from the airfoil trailing edge $x/c-1$. Figures 6a and b show that the wake half width L_w/c grows approximately with the square root of streamwise distance, from an origin close to the trailing edge. Conversely the velocity scale U_w/U_e decays approximately with the square root of streamwise distance from a similar origin. Square-root variations are expected for a fully developed turbulent wake (see, for example, Townsend , 1956) but, as revealed below, this does not imply that the wake was fully developed over its entire length. As expected, the momentum thickness (figure 6c) is almost constant at a value of about $0.0093c$, implying a wake momentum thickness Reynolds number $U_e\theta/\nu$ of 3060 and an airfoil drag coefficient of 0.0187. This value appears reasonable - according to standard roughness formulae (Schlichting, 1968) a flat plate with the same roughness distribution and chordlength of the present airfoil would produce a drag coefficient of 0.0128. Following Wygnanski *et al.* (1986), the

preservation of the wake momentum deficit can also be examined by plotting θ/L_w vs.

U_w/U_e which should follow a relationship of the form $\frac{\theta}{L_w} = \frac{U_w}{U_e} \left(\mathfrak{I}_1 - \frac{U_w}{U_e} \mathfrak{I}_2 \right)$. The present results, plotted in figure 6d, very closely follow this form, with $\mathfrak{I}_1 = 2.058$ and $\mathfrak{I}_2 = 1.503$ (determined by least-squares fit) - almost identical to the values of 2.06 and 1.505 inferred by Wygnanski *et al* from their measurements.

Figure 7 through 9 show the mean velocity, turbulence stress and triple product profiles measured at all 18 stations. Figures 10 through 12 show the same quantities for the cross section measured at $x/c=9.33$. Velocity time spectra measured at the 18 stations are presented in figures 13 and 14. All profiles are presented normalized on U_w and L_w . Once the wake achieves a fully developed self-similar state, profiles plotted in this form should be invariant with streamwise distance. The spectra similarly show the progression to a self-similar state. Autospectra G (units of velocity squared per Hertz) are normalized as $GU_e/(U_w^2 L_w)$ and plotted against frequency f (in Hertz) normalized as fL_w/U_e - the presumption being that the turbulence is convected at approximately U_e .

The mean U velocity profiles (figure 7) appear self-similar over the whole measured length of the flow. The profile shape is quite accurately described by the exponential function $\frac{U_e - U}{U_w} = \exp\left(-k_1 \frac{y^2}{L_w^2} - k_2 \frac{y^4}{L_w^4}\right)$ where k_1 and k_2 are 0.632 and 0.0612 respectively. Wygnanski *et al.* (1986) found a good fit to the same equation with constants of 0.637 and 0.056 respectively. Self similarity takes longer to appear in the Reynolds stress and triple product profiles (figures 8 and 9). The most important Reynolds stresses $\overline{u^2}$, $\overline{v^2}$, $\overline{w^2}$, and \overline{uv} and triple products $\overline{u^3}$, $\overline{v^3}$, $\overline{u^2 v}$, $\overline{uv^2}$, $\overline{vw^2}$, $\overline{uw^2}$ appear to reach self-similarity at about $x/c = 9.34$. Interestingly, of all these quantities $\overline{v^2}$,

after overshooting its fully developed level, takes easily the longest to reach self similarity. The shape of the self similar Reynolds shear stress \overline{uv} profile is very close to that measured by Wygnanski *et al.* (1986) for an airfoil wake, as is the peak value of this stress $0.04U_w^2$. The turbulence kinetic energy production in the wake is dominated by this stress and reaches its largest value, of close to $0.03U_w^3/L_w$, at this peak. Assuming the dissipation rate matches the production, this number implies a Kolmogorov microscale for this flow of $0.010L_w$ in the fully developed region ($=0.17\text{mm}$ at $x/c=9.34$). Both upstream and downstream of $x/c = 9.34$ all the profiles are closely symmetric or anti symmetric about the wake centerline - consistent with accuracy in the measurements.

In an exactly two-dimensional plane wake the stresses and triple products \overline{uw} , \overline{vw} , $\overline{w^3}$, $\overline{u^2w}$, $\overline{wv^2}$, \overline{uvw} are identically zero because of the symmetry constraints on w . The profiles here show these quantities to be small, but not exactly zero. One could of course attribute these residual levels to measurement uncertainty. However, the shapes of these profiles suggests some connection with the small W component velocities measured in the wake (figure 7c). While only a few percent of the axial velocity deficit, the W profiles suggest the presence of weak streamwise vorticity in the wake. Specifically, many of the profiles suggest a jump in W through the wake of between 8 and 2% U_w (ignoring those profiles most obviously influenced by drift in the measurement of this small quantity). At $x/c=2.68$, for example, the velocity jump is about 7.5% U_w . This would imply a vortex sheet embedded in the wake with a strength of 7.5% $U_w = 1\% U_e$. Such a sheet could be generated by a variation of about ± 0.1 degrees in the effective angle of attack of the airfoil across its span. The presence of such a variation seems extremely likely - one imagines that almost all wind tunnel test sections have flow angle non-uniformities of at

least this magnitude. So, while the residual values of these mean velocity, stress and triple product components are some indication of departures from precise two-dimensionality, it would clearly require an unusually precise test-section flow to do much better.

The geometric two-dimensionality of the wake flow is apparent in the cross-sectional measurements made at $x/c = 9.34$, figures 10 to 12. Except in the (rather uncertain) contours of V and W these measurements show no significant spanwise variations of any of the measured quantities. These measurements cover the region in which all the two-point velocity measurements were made.

The auto and cross-spectra measured at the wake centerline (figures 13) and approximately one half-wake width from the centerline (figure 14) reveal the distribution of energy amongst the various length scales of the flow. As with the Reynolds stresses, the autospectrum of upwash (v) velocity fluctuations (figures 13b and 14b) is the last to achieve a self-similar form. The v spectra display a distinct peak near $fL_w/U_e = 0.25$, usually thought to be associated with the passage frequency of the dominant coherent structures, and it is around this peak that the self-similar spectral shape takes longest to develop. The u and w autospectra measured near $y/L_w = -1$ display inertial subranges (of $-5/3$ slope) over about 1 decade of frequency range. Similar smaller regions are visible in the spectra measured on the centerline. The cross spectrum of u and v velocity fluctuations measured at $y/L_w = -1$ (figure 14d) shows that, in the fully developed region, almost all the Reynolds shear stress is generated by motions at frequencies less than the apparent passage frequency of dominant structures ($fL_w/U_e = 2.5$). Below this frequency

the coherence between u and v fluctuations is constant at about 0.4. Above this frequency the coherence is zero, the change occurring surprisingly rapidly near $fL_w/U_e=2.5$.

5. TWO-POINT TURBULENCE MEASUREMENTS

5.1 Test Matrix

All two-point measurements were made at $x/c=9.34$. Seventeen sets of measurements were made. For each set, one of the four sensor probes was set at a fixed y location in the wake on the tunnel centerplane ($z=0$). This probe (the 'fixed' probe) was closely aligned with the tunnel axis and thus the flow direction. A second four-sensor probe (the 'moveable' probe) was then positioned at some 400 points around the fixed probe (e.g. figure 15) using the two-axis traverse gear. Each point corresponded to a different spanwise separation between the probes Δz (up to a maximum of between -2 and $-3L_w$) and a different normal separation, Δy (up to a maximum of between ± 3 and $\pm 4.1L_w$). Measurements were made for both positive and negative y -separations, but only for negative z -separations, since the correlation function was expected to be symmetric about $\Delta z=0$. As show in figure 15, points were taken at a greater density for smaller separations than for larger separations, in anticipation of the shape of the correlation function. The moving probe was yawed at some 13 degrees to the tunnel axis to enable its measurement volumes to be brought as close as possible to that of the fixed probe. The minimum probe separation thus achieved was 2.5mm and the minimum change in probe separation between points was 1.2mm. At each point 50 records, each 3072 points in length, were recorded from each of the 8 sensors at a rate of 50kHz - sufficient to calculate a low uncertainty estimate of the cross-spectrum tensor between the probes. The

four sensors of each probe were sampled simultaneously using the HSDAS-12 analog-to-digital converter, but there was a delay of 10 μ sec between the sampling of the two probes. The effect of this delay is to introduce a slight phase shift into the cross-spectrum tensor, which was corrected during post processing.

As mentioned above, seventeen such sets of measurements were made, each for a different y location of the fixed probe. We intended to take measurements for an evenly spaced set of fixed-probe y locations but day to day uncertainty in setting the absolute traverse position resulted in an irregularly spaced set extending from $y/L_w = 0.1$ and -2.7 . Almost all the measurements were made with the fixed probe on one side of the wake, since the wake was expected to be symmetric about its centerline.

Uncertainty estimates for two-point measurements are presented in table 1.

5.2 Data Reduction

All measurements were recorded in time-series form as binary A/D converter representations of the sensor voltages. The complete unreduced data set filled some 40 half-Gigabyte CDROM disks. The primary objective of reducing these was to obtain an accurate explicit empirical description of the two-point correlation tensor in a form that could be used directly in broadband noise calculations. Using index notation for the velocity components (i.e. u_i = velocity component in direction i) we define the two-point correlation tensor function as $R_{ij} = R_{ij}(y, \Delta y, \Delta z, \tau) = \overline{u_i(y, z, t)u_j(y + \Delta y, z + \Delta z, t + \tau)}$ where the overbar denotes expected value. R_{ij} is independent of absolute z and time t because the flow was closely homogeneous in these directions. Note that we define the time delay τ as positive for an event that occurs at the moveable probe (at $y + \Delta y, z + \Delta z$) after a

correlated event at the fixed probe (at y and z). We will also refer to the correlation function using the notation $R_{ij} = R_{ij}(y, y', z', \tau) = \overline{u_i(y, z, t) u_j(y', z', t + \tau)}$ where y' and z' denote the absolute location of the moveable probe.

The two point measurements were first reduced by converting the binary voltage representations to estimates of the instantaneous velocity vector at the two probe locations. Fairly early on in the analysis an intermittent problem was detected in the outputs of one of the sensors of the moving probe. Under different circumstances such a problem could be catastrophic since it would have an unknown influence over all of the measurement results. However, when it comes to measuring the instantaneous value of the three components of velocity, the four-sensor probe has a redundant sensor. We were therefore able to reformulate the hot-wire reduction equations using velocity estimates based only on the outputs of the three reliable sensors, and recompute the direct angle calibration of the probe based upon these new equations. The net effect was that the faulty sensor could be ignored with out adversely affecting the accuracy of the instantaneous velocity measurements.

With this problem corrected the instantaneous velocity records obtained at each probe separation were processed by breaking them into 1024 point records (with a 50% overlap) and computing the average (over 250 realizations) of the cross-spectrum tensor between the two velocity signals. Average autospectra measured by the fixed probe were also computed to provide data for zero Δy and Δz . Average spectra were corrected for the slight phase shift associated with the non-simultaneous sampling of the probes, rotated to account for the different alignment of the two-probes relative to the flow, and inverse Fourier transformed to obtain 1024-point estimates of the time-delay correlation. Finally the probe coordinates associated with each time delay correlation tensor ($y, \Delta y, \Delta z$) were

rotated slightly to account for a roll angle of about 1.3 degrees between the vertical and horizontal axes of the wind-tunnel traverse and the y and z axes of the plane wake.

These data, which are final in the sense that they encapsulate in reduced and corrected form all the empirical information gathered about the two-point correlation tensor, do not form a convenient or useable expression of that function. The size of the reduced data set alone (some 500Mbytes) makes manipulation impractical on most computers. The irregular grids in y , Δy and Δz make that manipulation slow and awkward even when sufficient memory is available. For these reasons the data were linearly interpolated onto a smaller and more easily referenced 4-dimensional grid. Considerable care was taken at each step of the interpolation to ensure that the interpolated data contained a faithful representation of the original points, in the sense that all significant features of the original data could be recreated from them.

Linear interpolation for probe separation and time delay was performed on to a rectangular grid corresponding to integer values of the transformed normalized variables

$$\begin{aligned}\alpha &= 32 \operatorname{sgn}(\tau) \sqrt{|\tau U_e / L_w| / 8.048} + 33 & -8.048 \leq \tau U_e / L_w \leq 8.048 \\ \beta &= 20 \operatorname{sgn}(\Delta y) \sqrt{|\Delta y / L_w| / 3.497} + 21 & -3.497 \leq \Delta y / L_w \leq 3.497 \\ \gamma &= -20 \operatorname{sgn}(\Delta z) \sqrt{|\Delta z / L_w| / 3.497} + 1 & -3.497 \leq \Delta z / L_w \leq 0.0\end{aligned}$$

The transformed variables provide finer resolution around zero separation and time delay than at large separations and time delays, reflecting the form and relative importance of the different parts of the correlation function.

Interpolation in time delay was carried out only over the range $-8.048 \leq \tau U_e / L_w \leq 8.048$ (data were available for $-16.096 \leq \tau U_e / L_w \leq 16.096$) since no significant correlations were observed beyond this range. Figure 16 illustrates the quality of this interpolation using, as an example, the magnitudes of the six components of the spectrum measured by the fixed probe at $y/L_w=0.077$. The 512 point spectra obtained

directly from the time-series data are compared with reconstructions obtained from the interpolated data by re-interpolating it using cubic splines in α back on to evenly spaced time delay values and then Fourier transforming the result. The original and reconstructed autospectra agree very closely at all frequencies.

Interpolation in Δy and Δz was carried out over a range of $3.497L_w$. In some cases, where this exceeded the Δz range of the data, extrapolation was performed assuming a Gaussian decay with respect to $\sqrt{\Delta y^2 + \Delta z^2}$. Figure 17 shows, in terms of the zero-time delay correlation in u velocity fluctuations measured with the fixed probe at $y/L_w=0.077$, the influence of this procedure. Figure 17a is an (unsmoothed) contour plot of the original uninterpolated data. Figure 17b shows a similar contour plot of the interpolated data set, and figure 17c shows that same data set with the extrapolation included. The interpolated data appears to be a faithful representation of the original measurements and the extrapolation appears to eliminate any discontinuity at the edge of the measured data set (its purpose). It is also clear from this picture that, at least at some points, the farfield decay of the correlation function in Δz was clipped by the limited range of the measurements. No clipping was observed in Δy .

Lastly the data were linearly interpolated to evenly spaced intervals in y from $y/L_w = 0$ to -2.74 in 16 steps of 0.1712 . In other words the data were interpolated to integer values of the variable δ , where

$$\delta = -16y / L_w / 2.74 + 1 \quad -2.74 \leq y / L_w \leq 0$$

The range and step size of this interpolation put many of the interpolated points at, or close to, actual fixed probe locations. As a result the effect of the interpolation at these

points was small. The size of the final interpolated representation of the two-point correlation tensor function is about 68Mbytes.

5.3 Data availability

These data and sample analysis programs are available as MATLAB files over the World Wide Web from <http://www.aoe.vt.edu/flowdata/flowdata.html> under 'DATA' and then 'Plane Wake'. We have expended significant effort to make these data user friendly so that they may be used by other researchers and perhaps incorporated directly into aeroacoustic calculations.

The two-point correlation function is contained within the file *ruiuj.mat* as the array *ruiuj*. To access this array, simply type 'load ruiuj' followed by a carriage return from the MATLAB command window. Depending on the speed and capacity of your computer the data may take about 15 seconds to load¹. The array *ruiuj* is a 6-dimensional array of the form $b[3\ 3\ 17\ 41\ 21\ 65]$ containing the correlation data normalized on the wake velocity scale U_w . The 1st and 2nd indices (dimensions 3 and 3) denote respectively the velocity component index at the fixed probe i and at the moving probe j . The third index (dimension 17) gives the value of the variable δ representing y . The 4th and 5th indices (dimensions 41 and 21) give the values of the transformed variables β and γ representing the Δy and Δz separation. The final index (dimension 65) is the value of the transformed variable α representing time delay τ .

Provided with the data is the MATLAB function *corr.m*. This function interpolates the correlation tensor function at points specified in terms of the 'primitive'

¹ All calculations in this report were performed on a 200MHz Pentium PC with 128Mbytes of RAM.

normalized variables, y/L_w , $\Delta y/L_w$, $\Delta z/L_w$ and $\tau U_e/L_w$. In other words it is the literal MATLAB expression of the function $R_{ij} = R_{ij}(y, \Delta y, \Delta z, \tau)$ with distances and time normalized on wake parameters. The wake parameters for this station are $L_w/c = 0.0858$ and $U_w/U_e = 0.0556$. The function returns the correlation normalized on U_w^2 . It accepts inputs for y/L_w between -2.74 and 2.74, for $\Delta y/L_w$ and $\Delta z/L_w$ between -3.497 and 3.497, for $\tau U_e/L_w$ between -8.048 and 8.048. Inputs outside these ranges return the MATLAB identifier NaN (not a number) which can easily be converted to zero (assuming that is what is desired). Values for positive y/L_w and $\Delta z/L_w$ are obtained by using the expected symmetry of the correlation function.

5.4 Example applications using the data

Included with the data are a number of MATLAB programs that illustrate some simple uses of the data set. To run each of these programs it is necessary first to load the correlation data with the commands 'clear' and 'load ruiuj'.

profile.m Plots the form of the Reynolds stress profiles for the wake, as shown in figure 18. Compare with single-point data in figure 8.

upspec.m Plots the v (upwash) component of the velocity autospectrum at selected locations across the wake (figure 19). Compare with single-point data in figures 13 and 14.

kwspec.m Plots the upwash wave number frequency spectrum $\Phi_{vv}(y, k_z, \omega)$ seen on a z -wise cut through the as a function of the cut position y (figures 20). Note the anisotropy in the spectrum and the maximum at zero spanwise wavenumber, presumably associated with the passage frequency of large organized eddies.

zerotcor.m Plots the zero-time delay correlation as a function of the reference position y (figure 21).

spod1d.m Plots the proper orthogonal decomposition of the velocity component u in the y direction in terms of its eigenvalue spectrum and first 10 modes (figure 22), see below.

5.5 Further applications

The example applications illustrate only a small fraction of the results that can be obtained with this function. One could use *corr.m* to determine the full upwash time delay correlation function in the leading edge plane of a blade of any geometry cutting the wake at any roll angle or, the upwash time-delay correlation for a curved blade cutting a plane wake. Alternatively, as per our hypothesis, one can estimate the correlation seen by a straight blade cutting a curved wake - this particular application is discussed further in the following sections.

Using Taylor's hypothesis (which one would expect to be fairly accurate in this flow) one can also obtain estimates of the time-delay correlation function between any two components at any two points in space moving in any frame of reference. To show this we first use Taylor's hypothesis to relate the full space time correlation function $\mathcal{R}_{ij}(y, \Delta x, \Delta y, \Delta z, \tau)$ to that measured $R_{ij}(y, \Delta y, \Delta z, \tau)$, i.e.

$$\mathcal{R}_{ij}(y, \Delta x, \Delta y, \Delta z, \tau) = R_{ij}(y, \Delta y, \Delta z, \tau - \Delta x/U_e)$$

Consider then the time delay correlation Q between the velocity component u_i at some point A at (x, y, z) and the component u_j at another point B at $(x + \Delta x, y + \Delta y, z + \Delta z)$ both attached to a blade that is translating through the wake with velocity vector \mathbf{V} . This

correlation will have the functional form $Q_{ij}(y, \Delta x, \Delta y, \Delta z, t, \tau)$. The dependence on absolute time t (referenced say to the instant when the point A cuts the wake centerline) results from the possibility that the blade is moving in the inhomogeneous y direction. Writing this correlation in terms of the velocity field $u_i(x, y, z, t)$ seen in the fixed frame of reference we have

$$Q_{ij}(y, \Delta x, \Delta y, \Delta z, t, \tau) = \langle u_i(x + V_x t, y + V_y t, z + V_z t, t) u_j(x + \Delta x + V_x(t + \tau), y + \Delta y + V_y(t + \tau), z + \Delta z + V_z(t + \tau), t + \tau) \rangle$$

Where the triangular brackets indicated the expected value taken over multiple realizations of the flow at the same absolute time t . This is the same as

$$Q_{ij}(y, \Delta x, \Delta y, \Delta z, t, \tau) = \mathcal{R}_{ij}(\Delta x + V_x \tau, y + V_y t, \Delta y + V_y \tau, \Delta z + V_z \tau, \tau)$$

which further reduces to

$$Q_{ij}(y, \Delta x, \Delta y, \Delta z, t, \tau) = R_{ij}(y + V_y t, \Delta y + V_y \tau, \Delta z + V_z \tau, \tau - (\Delta x + V_x \tau)/U_e)$$

Thus obtaining $Q_{ij}(y, \Delta x, \Delta y, \Delta z, t, \tau)$ simply involves the appropriate evaluation of the MATLAB function for R_{ij} . A similar analysis can be used to write the correlation between two points moving in different frames of reference (such as points on the leading edge of a fan blade) in terms of R_{ij} . This usefulness of the correlation function simply results from the fact that once completely defined, it contains all the double velocity correlation information contained within the flow field.

5.6 Results and discussion

In this section we present and discuss some of the two-point measurements. First several cuts through the correlation tensor function are discussed. Such simple representations are informative but provide only a very limited view of this four-

dimensional tensor function. In an attempt to reveal the physical information encapsulated in the function in a more explicit and compact form, the methods of linear stochastic estimation and proper orthogonal decomposition are then applied to the data. Proper orthogonal decomposition is of particular interest since it provides a compact representation of the turbulence suited to the computation of broadband noise resulting from interactions between a lifting surface and inhomogeneous turbulence (see Glegg and Devenport, 1997). Finally, we examine the range of application of the two-point wake data by using it to estimate correlation functions and wavenumber frequency spectra measured previously in the spiral wake surrounding a tip vortex.

5.6.1 Form of the correlation tensor function

Figure 23 shows a cut through the correlation tensor function zero time delay and zero spanwise separation $R_{ij}(y, y', z', \tau) = R_{ij}(y, y', 0, 0)$. The plots show all 9 components of the correlation function. The lines $y=y'$ represent the Reynolds stress profiles. The measured data are fairly symmetric about the bottom left to top right diagonal - an indication that they are closely consistent with the requirement that $R_{ij}(y, y', 0, 0) = R_{ji}(y', y, 0, 0)$. Most of the contours of the normal correlations R_{11} , R_{22} and R_{33} are eye-shaped indicating correlations over greater y distances near the wake centerline than at its edges. Not surprisingly correlations of the vertical velocity component R_{22} extend over the greatest vertical distance, those of the spanwise velocity fluctuations R_{33} over the smallest distance. There are also some more subtle features that may be of significance - lobes of negative correlation at larger separation in R_{33} , 'wings' in the R_{11} correlation near the wake center and asymmetry in the R_{12} correlation associated with the

dominant Reynolds shear stress.

Figure 21, 24 and 25 show cuts through the normal components of the correlation function R_{ii} at zero time delays for fixed probe locations $y/L_w=0, 1$ and 2 . These pictures reveal quite a different view of the function in which we see one feature of the relationship between velocity fluctuations in different parts of the wake. For $y/L_w=0$ the correlation maps are fairly symmetric in Δy and Δz as they should be. The contours show a preference for upwash correlations (figure 21) in the vertical direction, and spanwise velocity correlations in the spanwise direction (figure 25), as might be expected. For $y/L_w=1$ and 2 , the correlation maps become more complex and skewed or appended in the negative Δy direction. This implies a preference for correlations with velocity fluctuations near the wake centerline, perhaps a simple consequence of the presence of large-scale turbulence structures in the wake and their tendency to occupy positions near the wake centerline.

Figure 26 shows this local asymmetry in the correlation function as a function of time delay, as seen on a cut at zero-spanwise separation for fixed probe locations $y/L_w=1.16$. The axial velocity correlation map (figure 26a) diagonal legs that extend to the corners of the map and are strongest below the fixed probe location - toward the wake centerline. The spanwise velocity map (figure 26c) reveals lobes of positive and negative correlation that, rather interestingly, have axes rotated from the vertical in the counterclockwise direction by about 45 degrees. The upwash correlation (figure 26b) is the most anisotropic and shows vertically aligned bands of positive and negative correlation. These oscillations in the upwash correlation are connected to the peak seen in time spectra (figures 13b, 14b) and wave-number frequency spectra (figure 20) attributed

to quasi-periodicity in the large eddy structure of the wake.

5.6.2 Characteristic eddy decomposition

It is tempting to use figures 23 to 26 to speculate in detail about the form of the instantaneous eddy structures responsible for the measured correlation maps. However, one must remember that these figures shows only single cuts through a four-dimensional function and, even at the resolution of the measured data, one could plot some 10000 such cuts for all the possible combinations of z' and τ . One therefore seeks a more objective and efficient method for extracting physical information about the structure of the instantaneous flow, particularly those aspects of the structure responsible for broadband noise.

Linear stochastic estimation (LSE) and proper orthogonal decomposition (POD) are both methods for extracting eddy-like velocity fields from correlation functions. LSE (Adrian, 1996) gives the best linear estimate of the instantaneous velocity field given some pre-determined condition, such as the value of a velocity component at one point $u_i(y)$. In this case the estimated velocity field is simply given by the two-point correlation function itself,

$$u_j(y', z', \tau)|_{LSE} = R_{ij}(y, y', z', \tau) \frac{u_i(y)}{u_i(y)^2} \quad (1)$$

(no summation implied).

POD (Lumley, 1967) provides a means to compute the optimum basis of the instantaneous velocity field, i.e. a series of orthogonal functions, or modes, that on average provide the best fit to the instantaneous velocity field. If the instantaneous flow can be characterized as a superposition of frequently appearing eddy types, then one

might reasonably expect the modes produced by POD to represent the form of those eddies. By maximizing the correlation with the instantaneous velocity field, Lumley shows that the modes are eigenfunctions of the two-point correlation tensor and that their spectrum is given by the corresponding eigenvalues. POD appears to work well in inhomogeneous directions, such as the y direction in the present flow. One can, for example, perform a one dimensional POD of the wake by solving the Fredholm integral (with summation),

$$\int R_{ij}(y, y', 0, 0) \phi_j(y') dy' = \lambda \phi_i(y) \quad (2)$$

This integral has multiple eigenfunction solutions $\phi_i^{(n)}(y)$ representing the orthogonal modes of the instantaneous wake velocity profile, and corresponding eigenvalues $\lambda^{(n)}$ (the spectrum) that reveal the proportion of the turbulence kinetic energy produced by each mode.

POD does not work so well in homogeneous directions since here it reduces to Fourier decomposition and sinusoids are obviously not good representations of eddies. The three-dimensional POD of the wake flow involves Fourier transforming with respect to z' and τ (or x) and then solution of the integral,

$$\int R_{ij}(y, y', k_z, k_x) \phi_j(y', k_z, k_x) dy' = \lambda(k_z, k_x) \phi_i(y, k_z, k_x)$$

where k_z is spanwise wavenumber and k_x represents frequency or streamwise wavenumber and summation is implied. Again there is a multiplicity of solutions, but each is modulated by sinusoidal variations in the homogeneous directions. To construct a three-dimensionally compact representation of an eddy from these modes Berkooz *et al.* (1993) suggest extracting only the dominant mode at each wavenumber combination and

then inverse Fourier transforming the result having made assumptions about the relative phasing of these modes. One potential problem with this approach is that it appears to assume a correlation between the dominant modes, when in fact the POD implies the absence of any such correlation.

An alternative approach, which we employ here, is to use POD only to extract the modal profiles in the inhomogeneous direction using equation (1). We then use LSE to obtain the best linear estimate of the three-dimensional instantaneous velocity field associated with each complete mode. For the n th mode $\phi_I^{(n)}(y)$ we obtain

$$u_j^{(n)}(y', z', \tau) |_{CM} = \frac{1}{\lambda^{(n)}} \int \phi_i^{(n)}(y) R_{ij}(y, y', z', \tau) dy \quad (3)$$

(summation implied). We refer to this approach as the 'combined method'.

It is important to note that the proper orthogonal decomposition of the turbulence is of direct relevance to aeroacoustics. As shown by Glegg and Devenport (1997) the computations of broadband noise generated by inhomogeneous turbulent flows are most efficiently carried out if the turbulence is described in terms of its proper orthogonal decomposition (as opposed to Fourier spectrum).

Figure 27 shows the eigenvalue spectrum from the solution to equation 2 and figure 28 shows the first 4 modal vector profiles. The measurement resolution allowed for the calculation of about 100 modes, of which the first 40 appeared free of any significant aliasing effects. Figures 29 through 32 show slices through the three-dimensional velocity fields of the characteristic eddy structures corresponding to these 4 modes, obtained using the combined method .

The eigenvalue spectrum (figure 27) shows that the first two modes contain significantly more energy than the others. Together these account for about 27% of the

total turbulence kinetic energy of the wake. The corresponding modal profiles (figures 28) are clearly associated with the generation of the Reynolds shear stress since they combine symmetric and antisymmetric u and v profiles. The third and fourth modes appear to imply more complex motions. Note that no w component appears in the first 4 modes. The corresponding characteristic eddies computed using equation 3 (figures 29 through 32) appear to be predominantly spanwise roller-type structures appearing either singly (modes 1 and 3) or in symmetric pairs (modes 1, 2 and 4). The remainder of these velocity fields away from the $z=0$ plane reveal no new significant structure. In particular, there is no sign of the so-called double roller eddy seen by Payne and Lumley (1967), among others, in cylinder wakes. The absence of such a structure is not in itself surprising since it is well known that the structure of a fully developed wake is strongly dependent on its initial condition.

It is also possible to obtain three-dimensional velocity fields of 'characteristic wake eddies' using LSE alone. This requires the choice of a velocity component and reference location (i.e. $u_i(y)$). These calculations, shown in figures 33 through 38, reveal eddy structures very similar to those seen using the combined method and the first two proper orthogonal modes.

It is tempting to speculate about the physical origins and role of these structures in the wake flow by assuming they are indeed representative of typical instantaneous motions (a frequent presumption in earlier work). It is also tempting to argue about the significance of these proper orthogonal modes for the prediction of broadband noise in blade-wake interaction problems. However, bearing in mind the results of our modeling efforts, we delay this discussion until chapter 6.

5.6.3 Estimation of correlation functions for a curved wake

While the present measurements can provide fairly complete information about the correlations that would be experienced by any blade cutting a plane wake flow, it is interesting to speculate that they may also be able to provide realistic estimates of the upwash correlations and spectra produced by curved and distorted wakes. Curved and distorted wakes are formed around the tip vortices shed from helicopter rotors, and in the tangential velocity fields downstream of engine fans, where they are implicated as significant noise generators.

Our hypothesis is that the plane wake data can be used to estimate the space time correlation function of a distorted wake, by taking a distorted path through the correlation function. The hope is that, while such estimates cannot be exact – one is ignoring the effects of wake stretching, curvature, interaction etc. upon the turbulence – they will be significantly more realistic than assuming homogeneous isotropic turbulence. This hypothesis has been tested by re-examining the data of Devenport *et al.* (1998), who measured upwash wave-number frequency spectra in a spiral wake under conditions very similar to those of the present experiment. Their experiment was performed in the tip vortex wake shed by a rectangular NACA 0012 half wing at a chord Reynolds number of 320,000. The wing was at 5 degrees angle of attack, and their measurements were made 10 chordlengths downstream of the wing leading edge in the Virginia Tech 3×2 Low Speed Wind Tunnel.

Figure 39 shows the cross-sectional structure of Devenport *et al.*'s (1998) flow in terms of axial turbulence normal stress $\overline{u^2}/U_e^2$. In this picture the vortex center is located

at the origin of the coordinate system (point D). The rotating velocity field of the vortex has rolled up the wake into a spiral form. A fairly detailed analysis of the variation in wake properties along this spiral, performed by Miranda (1996), is available. Devenport *et al.* made 4 sets of two-point measurements in this flow. For each set, the fixed probe was placed at the point marked with the solid circle, and the moveable probe was traversed to a number of points along the intersecting line. These measurements were used to obtain estimates of the correlation functions and wave-number frequency spectra that would be seen about a point on the leading edge of a horizontal blade cutting this flow.

We concentrate our efforts here on the measurements made for the fixed-probe point C, in the region where the wake is suffering very intense lateral curvature and stretching (see Miranda, 1996). Figure 40(a) shows in detail the geometry of the wake centerline (locus of minimum streamwise mean velocity) and two-point traverse line in this region. The measurements made along are related to those made in the present plane wake by assuming that distances and velocities measured parallel and perpendicular to the wake centerline are equivalent in the two cases, when normalized on the respective half wake widths L_w and velocity scales. Thus a curved path through the plane wake flow, defined by the cartesian coordinates y , Δy , Δz and velocity components v and w (see figure 40b), is equated to the straight path through the spiral wake described by equivalent curvilinear coordinates and components measured perpendicular and parallel to the centerline (figure 40a).

The principal source of uncertainty in this process is the specification of the appropriate half-wake width L_w for the spiral wake since the mean velocity field around

point C is significantly influenced by the axial velocity deficit of the nearby vortex core. Miranda (1996) gives the half wake width at location C as $0.0276c$, based only on the upper half of a mean velocity profile measured perpendicular to the centerline. However, this estimate, which is one third of the half width of the unrolled up portion of the wake ($0.0827c$), is at odds with the form of the Reynolds stress fields (e.g. figure 39) which suggest a wake half-width near C of about two-thirds that seen in the unrolled up portion (i.e. $0.0551c$).

We present results in figures 41 through 44. Figure 41a shows the space time correlation maps for the three velocity components measured by Devenport *et al.* (1998). Figures 41b through 41d show estimates obtained from the plane wake data for each of the possible lengthscale choices ($0.0276c$, $0.0580c$, and $0.0827c$). The results are presented in terms of the spiral-wake cartesian coordinate system (x_s, y_s, z_s) (u_s, v_s, w_s) defined in figures 39 and 40. We define the space time correlation of streamwise velocity fluctuations u_s as $R_{u_s u_s}(y_s, z_s, \Delta z_s, \tau) = \overline{u_s(y_s, z_s, t) u_s(y_s, z_s + \Delta z_s, t + \tau)}$, with similar definitions for the upwash v_s and spanwise w_s components. Here y_s and z_s denote the position of the fixed probe, and thus remain constant. Correlations are normalized on the mean-square fluctuation of the velocity component in question at the fixed probe location.

Figures 42 through 44 compare the Fourier transforms of the correlation maps - i.e. the pointwise wavenumber frequency spectra - defined for u_s as

$$\phi_{u_s u_s}(y_s, z_s, k_{z_s}, K_{x_s}) = \frac{U_e}{4\pi^2} \int_{-\infty}^{\infty} R_{u_s u_s}(y_s, z_s, \Delta z_s, \tau) e^{-jU_e K_{x_s} \tau - jk_{z_s} \Delta z_s} d\tau d\Delta z_s \text{ with similar definitions for}$$

v_s and w_s . Here K_{x_s} represents the angular frequency ω in terms of the nominal

streamwise wavenumber $K_{xs}=\omega/U_e$. The Fourier transform is performed by assuming the correlation function is symmetric about $\Delta z_s=0$.

The large variation in the plane wake estimates visible in figures 41 through 44 reveal how important the length scale choice is. However, with the lengthscale based upon the turbulence field ($0.0551c$) the correlation maps (figure 41c) and wavenumber frequency spectra (figure 43) estimated from the plane wake data show reasonable overall agreement with Devenport *et al.*'s measurements. The estimates display most of the important features - the negative lobes in the upwash v_s correlation map, the spectral peak in the upwash spectrum, as well as some of the anisotropy seen in all the correlations and spectra. They also show some significant disagreement, however - the shape of the u_s correlation is poorly estimated in all cases, the anisotropy of the upwash spectrum is overpredicted, for example. These shortcomings are not unexpected since by using the plane wake data we are ignoring the effects of wake stretching, curvature, interaction etc. upon the turbulence. However, the estimates based on the plane wake data still appear significantly more realistic than the homogeneous isotropic functions that are implied by the use of von Karman's interpolation formula or similar models. This approach may therefore offer some improvement for broadband noise calculations if the wake characteristics can be accurately be determined.

6. MODELING OF THE TWO-POINT CORRELATION TENSOR FUNCTION

6.1 Introduction

The objective of the modeling effort was to develop a simple technique for

extrapolating the two-point correlation tensor function from single-point Reynolds stress data that could be tested using the wake flow measurements. We were inspired by the need for such models in aeroacoustics, by the smooth form revealed by the two-point correlation tensor measurements, and by the hypothesis that much of this form might be a direct result of the inhomogeneity of the turbulence field coupled with the constraints of continuity. Our philosophy was to develop the simplest and most generic method consistent with this hypothesis. For the purposes of modeling we deal exclusively with the space correlation function, in the knowledge that for low turbulence flows space time correlations can be inferred from this function using Taylor's hypothesis (see for example section 5.5). We therefore write the two-point correlation tensor as

$$R_{ij}(\vec{r}, \vec{r}') = \overline{u_i(\vec{r}) u_j(\vec{r}')} \quad (4)$$

where $\vec{r} = x_i = (x, y, z)$ and $\vec{r}' = x'_i = (x', y', z')$ denote the two points and u_i ($i=1,2,3$) denotes the velocity components in the directions of x , y and z . In incompressible flow R_{ij} must be divergence free with respect to both indices, i.e.

$$\frac{\partial R_{ij}}{\partial x_i} = 0 \quad (5)$$

$$\frac{\partial R_{ij}}{\partial x_j} = 0 \quad (6)$$

using summation subscript notation. This property that can be guaranteed (Chandrasekhar, 1950) by writing it as the double curl of another tensor function,

$$R_{ij}(\vec{r}, \vec{r}') = \epsilon_{ikl} \epsilon_{jmn} \frac{\partial^2 q_{ln}(\vec{r}, \vec{r}')}{\partial x'_m \partial x_k} \quad (7)$$

The unit alternating tensor ϵ_{abc} is equal to unity if a, b, c are in cyclic order (1 2 3 1 2 3 1....), -1 if a, c, b are in cyclic order, and zero otherwise. To demonstrate that the result of equation (6) has the correct properties we substitute this expression into equations (2) and (3), yielding

$$\frac{\partial R_{ij}}{\partial x_i} = \epsilon_{ikl} \epsilon_{jmn} \frac{\partial^3 q_{ln}}{\partial x'_m \partial x_k \partial x_i} \equiv 0 \quad (8)$$

$$\frac{\partial R_{ij}}{\partial x_j} = \epsilon_{ikl} \epsilon_{jmn} \frac{\partial^3 q_{ln}}{\partial x'_m \partial x_k \partial x_j} \equiv 0$$

By analogy with vector calculus, we refer to q_{ln} as the 'tensor potential'.

6.2 Form of q_{ln} for homogeneous turbulence

It is well known (see for example Hinze, 1975) that the two point correlation tensor for homogenous isotropic turbulence can be written as,

$$R_{ij}(\vec{r}, \vec{r}') = u^2 \left[\frac{f(s) - g(s)}{s^2} (x_i - x'_i)(x_j - x'_j) + g(s) \delta_{ij} \right] \quad (9)$$

where $s = |\vec{r} - \vec{r}'|$, $f()$ is the longitudinal correlation coefficient function, $g()$ is the lateral correlation coefficient function, u the velocity scale of the turbulence, and δ_{ij} is the Kronecker delta. Alternatively, using the relationship between $g()$ and $f()$, namely

$$g(s) = f(s) + \frac{1}{2} s \frac{\partial f(s)}{\partial s} \quad (10)$$

this expression is written as

$$R_{ij}(\vec{r}, \vec{r}') = u^2 \left[-\frac{(x_i - x_i')(x_j - x_j')}{2s} \frac{\partial f(s)}{\partial s} + \delta_{ij} \left(f(s) + \frac{1}{2} s \frac{\partial f(s)}{\partial s} \right) \right] \quad (11)$$

We will now show that the tensor potential description of this two-point correlation tensor function is simply,

$$q_{ln} = -\frac{1}{2} u^2 h(s) \delta_{ln} \quad (12)$$

where $h(s) = \int_0^s s f(s) ds$. This can be demonstrated simply by substituting equation (12) into equation (6) and performing the differentiation.

$$\begin{aligned} R_{ij}(\vec{r}, \vec{r}') &= -\frac{u^2}{2} \epsilon_{ikl} \epsilon_{jmn} \frac{\partial^2 h(s)}{\partial x_m \partial x_k} \delta_{ln} \\ &= -\frac{u^2}{2} \epsilon_{ikl} \epsilon_{jml} \frac{\partial^2 h(s)}{\partial x_m \partial x_k} \end{aligned} \quad (13)$$

Now,

$$\frac{\partial h(s)}{\partial x_m} = s f(s) \frac{\partial s}{\partial x_m} \quad (14)$$

and so,

$$\frac{\partial^2 h(s)}{\partial x_m \partial x_k} = (f(s) + s \frac{\partial f(s)}{\partial s}) \frac{\partial s}{\partial x_m} \frac{\partial s}{\partial x_k} + s f(s) \frac{\partial^2 s}{\partial x_m \partial x_k} \quad (15)$$

where

$$\frac{\partial s}{\partial x_m} = \frac{x_m' - x_m}{s}, \quad \frac{\partial s}{\partial x_k} = \frac{x_k - x_k'}{s}, \quad \frac{\partial^2 s}{\partial x_m \partial x_k} = \frac{(x_m - x_m')(x_k - x_k')}{s^3} - \frac{\delta_{mk}}{s} \quad (16)$$

Substituting back into equation (13) we get,

$$\begin{aligned} R_{ij}(\vec{r}, \vec{r}') &= \frac{u^2}{2} \epsilon_{ikl} \epsilon_{jml} \left[(f(s) + s \frac{\partial f(s)}{\partial s}) \frac{(x_m - x_m')(x_k - x_k')}{s^2} - f(s) \left(\frac{(x_m - x_m')(x_k - x_k')}{s^2} - \delta_{mk} \right) \right] \\ &= \frac{u^2}{2} \epsilon_{ikl} \epsilon_{jml} \left[\frac{\partial f(s)}{\partial s} \frac{(x_m - x_m')(x_k - x_k')}{s} + f(s) \delta_{mk} \right] \end{aligned} \quad (17)$$

for $i \neq j$ this equation reduces to

$$R_{ij}(\vec{r}, \vec{r}') = -\frac{u^2}{2} \left[\frac{\partial f(s)}{\partial s} \frac{(x_i - x_i')(x_j - x_j')}{s} \right] \quad (18)$$

for $i=j$ it becomes

$$R_{ii}(\vec{r}, \vec{r}') = \frac{u^2}{2} \left[\frac{\partial f(s)}{\partial s} \frac{s^2 - (x_i - x_i')^2}{s} + 2f(s) \right] \quad (19)$$

which are identical to equation (11).

The compact nature of the tensor potential representation (equation 12) compared to the conventional form (equation 11) is encouraging and suggests that it may be an efficient modeling tool.

6.3 Relationship to Proper Orthogonal Decomposition

In proper orthogonal decomposition (Lumley, 1967) the instantaneous velocity field of a flow is decomposed into a sum of orthogonal modes $\phi^{(p)}$ multiplied by uncorrelated coefficients $a_p(t)$,

$$u_i(\vec{r}, t) = \sum_p a_p(t) \phi_i^{(p)}(\vec{r}) \quad (20)$$

The modes are determined from the two-point correlation tensor as the eigenfunction solutions to the equation,

$$\int_V R_{ij}(\vec{r}, \vec{r}') \phi_i^{(p)}(\vec{r}') dV(\vec{r}') = \lambda_p \phi_j^{(p)}(\vec{r}) \quad (21)$$

where the eigenvalues λ_p give the mean square values of the coefficients a_p and dV denotes a volume element. The correlation tensor may be reconstructed from the modes by the summation

$$R_{ij}(\vec{r}, \vec{r}') = \sum_p \lambda_p \phi_i^{(p)}(\vec{r}) \phi_j^{(p)}(\vec{r}') \quad (22)$$

The POD is optimal in the sense that it guarantees, on average, reconstruction of the velocity field to a given accuracy from the fewest number of modes. It also maximizes the projection of u_i onto the modes, and thus it is often supposed that the modes will represent the averaged form of the coherent structures. Indeed POD has been claimed as providing an objective definition of the term coherent structure, at least in inhomogeneous flows (Paine and Lumley, 1967).

Since the modes and eigenvalues are determined from R_{ij} the question of their relationship to the tensor potential arises. This relationship can be determined by considering the proper orthogonal decomposition of the vector potential, i.e.

$$q_{ln}(\vec{r}, \vec{r}') = \sum_p \xi_p \psi_l^{(p)}(\vec{r}) \psi_n^{(p)}(\vec{r}') \quad (23)$$

where the modes $\psi^{(p)}$ and eigenvalues are obtained from an equation analogous to (22). Substituting this expression into equation (7) we obtain

$$R_{ij}(\vec{r}, \vec{r}') = \sum_p \xi_p \left(\epsilon_{ikl} \frac{\partial \psi_l^{(p)}(\vec{r})}{\partial x_k} \right) \left(\epsilon_{jmn} \frac{\partial \psi_n^{(p)}(\vec{r}')}{\partial x_m} \right) \quad (24)$$

Thus the eigenvalues for R_{ij} are the same as those for q_{ij} and the proper orthogonal modes of R_{ij} are the curl of the proper orthogonal modes of q_{ij} . Physically then, the modes of q_{ln} must provide the optimal reconstruction of the *vector* potential of the instantaneous velocity field. This implies some potentially useful efficiencies in the form of q_{ln} . Since it is a curl function, one can add any gradient field to the vector potential of velocity without altering the velocity field. This implies that the vector potential can be specified using only two components. The tensor potential can therefore be specified completely in

only four components (see equation 23). We do not use this simplification here, but feel it may well be valuable in more refined modeling efforts.

6.4 Modeling approach and application to the wake flow

Since our objective is the development of a simple technique for extrapolating the two-point correlation tensor function from single-point turbulence data, we need a method for prescribing the tensor potential in a manner consistent with a specified Reynolds stress field. Conceptually, we envision q_{ln} as the product of two functions. A scaling function that ensures consistency of the correlation function with the specified Reynolds stress field (and thus the inhomogeneity of the flow), and a decay function that becomes unity when $\vec{r} = \vec{r}'$ and represents (in vector potential terms) the normalized correlation.

The simplest possible expression for q_{ln} that can work for inhomogeneous turbulence is equation 12 but with u^2 is replaced by a scaling function that makes R_{ij} consistent with the single point Reynolds stress data. The expression,

$$q_{ln}(\vec{r}, \vec{r}') = [\alpha_{lo}(\vec{r})\alpha_{on}(\vec{r}') - \frac{1}{2}\delta_{ln}\alpha_{op}(\vec{r})\alpha_{po}(\vec{r}')]h(|\vec{r} - \vec{r}'|) \quad (25)$$

where α_{ij} is the square root of the specified Reynolds stress tensor, is one such form. The term in the square brackets becomes equal to the Reynolds stress tensor less half its trace when $\vec{r} = \vec{r}'$. If $h()$ retains the properties of the first moment of a correlation coefficient function (i.e. paraboloidal with unit second derivative and zero value at $\vec{r} = \vec{r}'$) then the double curl operation recovers the Reynolds stress tensor.

This form of the model is not very sophisticated but it is completely generic and could be applied to any turbulent flow of known Reynolds stress field. Furthermore,

equation 25 is a fairly straightforward application, and thus test, of our underlying hypothesis that much of this form of the two-point correlation tensor may result from the inhomogeneity of the turbulence field coupled with the constraints of continuity. We are in no doubt that the equation 25 could be improved by incorporating more complex variations (e.g. a non-isotropic decay function $h()$ that depends on location) but we have resisted this temptation preferring, instead, to test the performance of the model without such flow-specific information.

To apply this equation 25 to the airfoil wake we specified the Reynolds stress field from the measured profiles at $x/c=8.33$ and chose $h()$ to be the first moment of a von Karman spectrum with the same length scale ($0.73L_w$) at all points throughout the wake. This value of the length scale was obtained by examining experimental time delay correlations at the wake centerline.

6.5 Results and discussion

Results are presented in figures 45 through 47. Figure 45 shows a cut through the modeled correlation tensor function zero time delay and zero spanwise separation $R_{ij}(y,y',z',\tau)=R_{ij}(y,y',0,0)$ which may be compared directly with the experimental data in figure 23. Many of the gross features of the correlations are quite well reproduced by the model. A number of differences are also visible most notably in the extent of the R_{22} correlation and in the predicted symmetry of R_{12} (symmetry is not necessarily dictated by equation 25). Figure 46 shows cut at zero-spanwise separation through the model correlation function for fixed probe locations $y/L_w=1.16$, and may be directly compared with figure 26. This comparison shows that the model reproduces some fairly subtle

details of the measurements - the diagonal legs in the axial velocity correlation map that extend below the fixed probe location toward the wake centerline, the positive and negative lobes in the spanwise velocity map and the counterclockwise rotation of their axes. The most significant difference between model and measurement is in the time delay correlation of upwash fluctuations. The oscillatory form of the measured correlation function is absent from the model results. This is not surprising. The oscillations are associated with the quasi-periodicity of the large-scale structures in the wake, and our model includes no such physics.

We can also use the predicted correlation tensor function to calculate proper orthogonal modes and associated characteristic eddy structures for the wake. Intuitively, one would not expect the model to reproduce the form of the modes or eddies, which are often thought of as representative of typical instantaneous motions, since it contains no physics beyond the Reynolds stress profile and a single length scale so one would not expect it to. Despite this, the modal spectrum (figure 27) obtained from the model is very similar to that measured and the model seems to provide an accurate prediction of the modal profiles (figure 28). Furthermore the model reproduces the dominant features of all the associated three-dimensional characteristic eddy structures (figure 47).

One could interpret these results as demonstrating that the instantaneous form of the dominant wake eddies can be predicted merely from the Reynolds stress distribution and a length scale. The alternative (and perhaps more realistic) interpretation is that the characteristic eddy structures are in fact not representative of the instantaneous eddies at all, but merely eddy-like representations of the correlation function. Either way, it appears that the modes and associated velocity fields can, at least approximately, be

predicted from the Reynolds stress field. This in turn implies that the modes are self-similar. Both observations provide important simplifications to the aeroacoustic problem of calculating the response of a downstream airfoil or structure to a wake flow.

7. CONCLUSIONS

Single and two-point turbulence measurements have been made in the plane turbulent wake shed from a NACA 0012 airfoil at zero angle of attack for a chord Reynolds number of 339,000. These measurements provide information and insight into the structure of the turbulence from the point of view of broadband noise generation through blade-wake interactions in helicopter rotors and aircraft engines.

The single point measurements of mean velocity, Reynolds stresses, triple products lead to the following conclusions.

1. All measurements showed the wake to be closely two-dimensional, and symmetric about its centerline.
2. Residual spanwise mean velocities and associated stresses and triple products were small, consistent with two-dimensionality. It is plausible that these residual levels are not spurious products of the measurement system, but could be generated by slight free-stream non-uniformity across the airfoil span.
3. The wake momentum thickness Reynolds number was 3060.
4. The wake reached a fully developed state about 900 momentum thicknesses downstream of the trailing edge.
5. The shape and development of the mean velocity field and the parameters describing it (half width and centerline axial velocity deficit) and the shape of

the Reynolds shear stress profiles are closely consistent with data and correlations from previous studies of plane wakes.

6. Upwash (v -component) spectra and turbulence normal stress profiles are the last of the statistical quantities measured to reach a fully developed state.
7. The Kolmogorov microscale for this flow is 1% of the half wake width in the fully developed region (0.17mm at the two-point measurement station).
8. Consistent with earlier studies the v autospectra measured in the fully developed wake display a distinct peak near $fL_w/U_e = 0.25$, usually attributed to the passage frequency of the dominant coherent structures.
9. The u and w autospectra display inertial subranges (of $-5/3$ slope) over about 1 decade of frequency range.
10. Almost all the Reynolds shear stress is generated by motions at frequencies less than the apparent passage frequency of dominant structures ($fL_w/U_e = 2.5$).

Two point turbulence measurements were made 9.34 chordlengths downstream of the airfoil leading edge at the start of the fully developed region. One of the probes was placed at 17 ‘fixed-probe’ locations across half of the wake width. For each of these positions, the second moveable probe was positioned at 400 locations around the fixed probe and the full cross-spectrum tensor between the fluctuating velocity vectors at the two stations was measured.

1. These data were reduced to obtain a complete description of the 4-dimensional two-point correlation tensor function of the fully developed

turbulent wake.

2. A compact representation of this function, suitable for use in aeroacoustic calculations, has been extracted from these measurements, and is publicly available in MATLAB[®] format. Sample codes are also available.
3. These data can be used to determine the upwash space-time correlation function seen by any blade cutting the wake on any path.
4. Comparison with earlier measurements made in the spiral wake around a tip vortex show that these data can also be used to estimate the upwash space-time correlations experienced by a blade cutting a distorted wake, as long as a suitable wake half-width is chosen.
5. The methods of linear stochastic estimation and proper orthogonal decomposition applied to these data reveal the modes, eigenvalue spectra and ‘characteristic eddy structures’ of the wake. Proper orthogonal decomposition is of particular interest since it provides a compact representation of the turbulence suited to the computation of broadband noise resulting from interactions between a lifting surface and inhomogeneous turbulence.
6. A simple generic technique has been developed to extrapolate the form of the two-point correlation tensor function from the Reynolds stress field of any flow.
7. Applied to the wake this reproduces many of the gross features of the correlation function, including the dominant proper orthogonal modes, their spectrum and the ‘characteristic eddy structures’ inferred from the experimental data.

8. This implies either that the instantaneous form of the dominant wake eddies can be predicted merely from the Reynolds stress distribution and a length scale or, that the characteristic eddy structures are in fact not representative of the instantaneous eddies at all, but merely eddy-like representations of the correlation function.
9. It also indicates that the modes are self-similar.
10. Both of these observations provide important simplifications to the aeroacoustic problem of calculating the response of a downstream airfoil or structure to a wake flow.

This report, and the data it describes are available over the World Wide Web at

<http://www.aoe.vt.edu/flowdata>.

8. REFERENCES

Adrian R J, 1996, "Stochastic Estimation of the Structure of Turbulent Fields", *Eddy Structure Identification*, Ed. J P Bonnet, pp. 145-195, Springer, New York.

Amiet R K, 1975, "Acoustic Radiation from an Airfoil in a Turbulent Stream", *Journal of Sound and Vibration*, vol. 41, no. 4, pp. 407.

Berkooz G, Holmes P, and Lumley J L, 1993, "The Proper Orthogonal Decomposition in the Analysis of Turbulent Flows", *Annual Reviews of Fluid Mechanics*, vol. 25, pp. 539-575.

Chandrasekhar S, 1950, "The Theory of Axisymmetric Turbulence", Philosophical Transactions of the Royal Society A, vol. 242, pp 557-577.

Devenport W J, Wittmer K S and Wenger C W, 1997, "The Spectral and Statistical Properties of Turbulence Generated by a Vortex/Blade-Tip Interaction", Final report to NASA Langley under Grant NAG 1 1539, January 1997.

Devenport W J, Wenger C W, Glegg S A L and Miranda J A, 1998, "Wave Number Frequency Spectra of a Lifting Wake for Broadband Noise Prediction", *AIAA Journal*, vol. 36, no. 6, pp. 881-887, June.

Engel M, 1995, "A wind-tunnel investigation of a wing-tip trailing vortex", M.S. Thesis, Virginia Tech.

Glegg S A L and Devenport W J, "Descriptions of turbulence for hydroacoustic applications", 5th International Congress on Sound and Vibration, University of Adelaide, South Australia, December 15-18, 1997.

Glegg S A L, Wittmer, K S, Devenport W J, Pope D S, 1997, "Broadband Helicopter Noise Generated by Blade Wake Interactions", AHS Technical Specialists Meeting for Rotorcraft Acoustics and Aerodynamics, October 28-30, Williamsburg VA.

Glegg S A L, 1998, "Broadband Fan Noise Generated by Small Scale Turbulence", Final Report to NASA under Grant NAG 1-1202, presented at the AST Engine Noise Workshop, April 21-23, Cleveland, Ohio.

Hinze J O, 1975, *Turbulence*, 2nd Edition, McGraw Hill, New York.

Lumley J, 1967, "The Structure of Inhomogeneous Turbulent Flows", Atmospheric Turbulence and Radio Wave Propagation, Eds. A M Yaglom and V I Tatarsky, pp. 166-176, Nauka, Moscow.

Miranda J, 1996, "The structure of a trailing vortex wake", M.S. Thesis, Virginia Tech.

Payne F R and Lumley J L, 1967, "Large Eddy Structure in the Turbulent Wake Behind a Circular Cylinder", Physics of Fluids Supplement, pp. S194-S196.

Schlichting H, 1968, "Boundary-Layer Theory", 6th Edition, McGraw Hill, New York.

Townsend A A, 1956, "The Structure of Turbulent Shear Flow", Cambridge University Press, Cambridge.

Wenger C W, Devenport W J, Wittmer K S and Muthanna C, 1998, "Two-Point Measurements in the Wake of a Compressor Cascade", 29th AIAA Fluid Dynamics Conference, June 15-18, Albuquerque, NM. AIAA-98-2556.

Wittmer K. S., 1996, "Turbulent flowfield downstream of a perpendicular airfoil-vortex interaction", PhD thesis, VPI&SU, Blacksburg, VA 24061.

Wittmer K S, Devenport W J and Wenger C W, 1997, "Turbulence Structure Resulting from a Vortex/Blade-Tip Interaction", AIAA 35th Aerospace Sciences Meeting, Reno, NV, January 6-10. Paper AIAA-97-0047.

Wittmer K. S., Devenport W. J. and Zsoldos J. S., 1998, "A four-sensor hot-wire probe system for three-component velocity measurement", Experiments in Fluids, vol. 24, pp. 416.

Wynanski I, Champagne F and Marasli B, 1986, "On the Large Scale Structures in Two-Dimensional Small Deficit Turbulent Wakes", Journal of Fluid Mechanics, vol. 168, pp. 31-71.

Single-Point Measurements

Uncertainty in $(U - U_w)/U_w$, V/U_w , W/U_w	0.008
Absolute uncertainty in u^2/U_∞^2	0.0023
Absolute uncertainty in v^2/U_∞^2	0.0077
Absolute uncertainty in w^2/U_∞^2	0.0062
Absolute uncertainty in $u'v'/U_\infty^2$	0.0025
Absolute uncertainty in $v'w'/U_\infty^2$	0.0013
Absolute uncertainty in $u'w'/U_\infty^2$	0.0013
Relative uncertainty in spectral levels	0.18

Two-Point Measurements

Uncertainty in $R_{ij}(y, \Delta y, \Delta z, \tau)/R_{ij}(y, 0, 0, 0)$	0.035
Relative uncertainty in spectral levels	0.18

Table 1. Uncertainty estimates at 20:1 odds based on measurements made near the wake centerline at $x/c=9.34$.

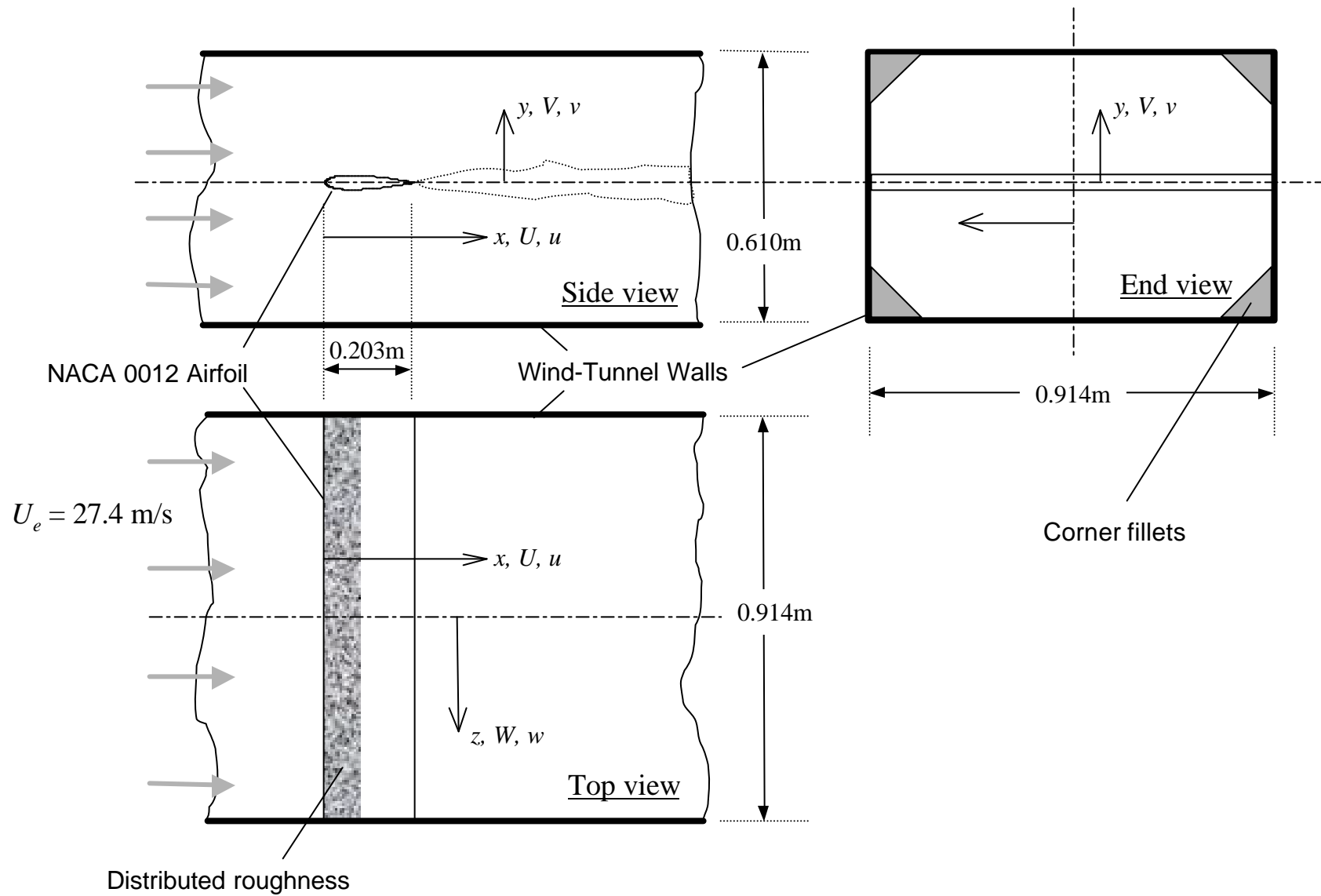


Figure 1. Schematic of the 3x2 wind tunnel and wing showing the coordinate system used

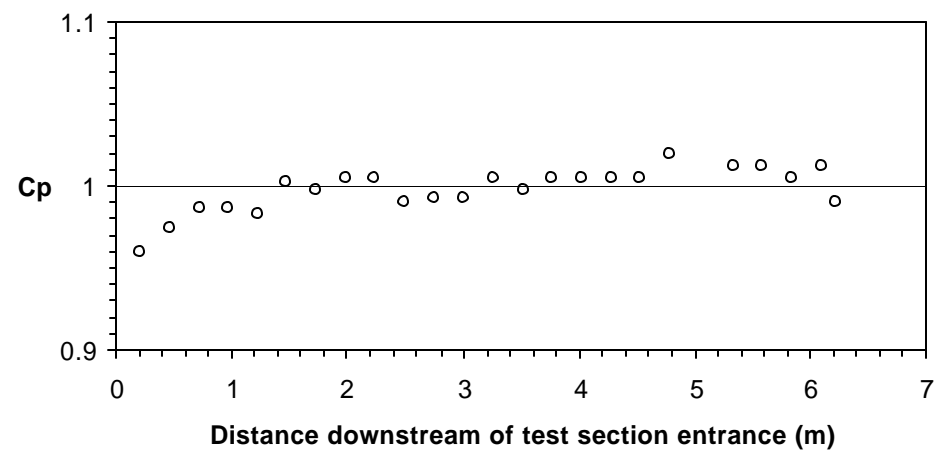


Figure 2. Streamwise pressure coefficient distribution in the empty 3'x2' wind tunnel test section with corner fillets at $U_e = 27.4\text{m/s}$.

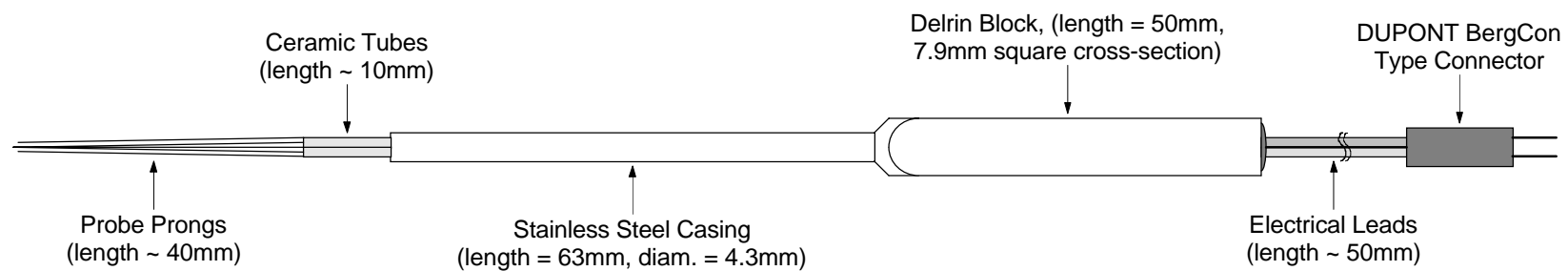


Figure 3. Schematic of the Auspex Corporation AVOP-3-100

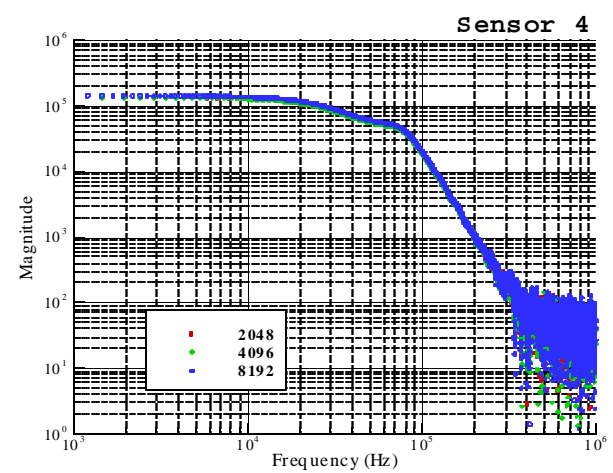
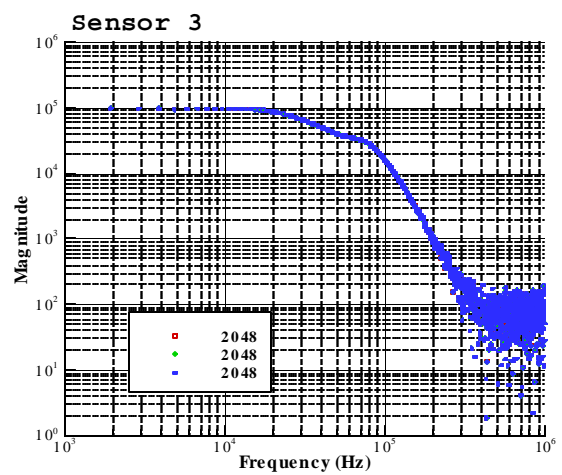
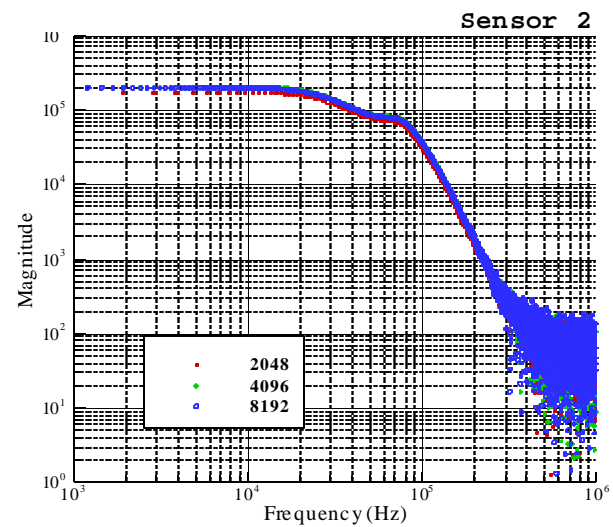
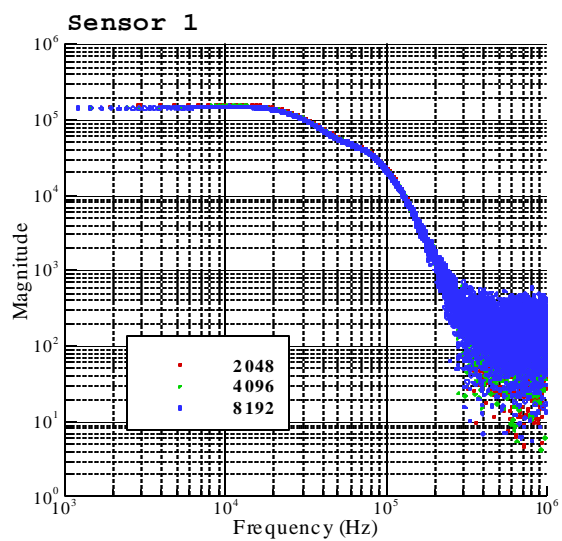


Figure 4a. Amplitude calibration for the sensor channels of the 'fixed' probe.
Magnitude scale is arbitrary.

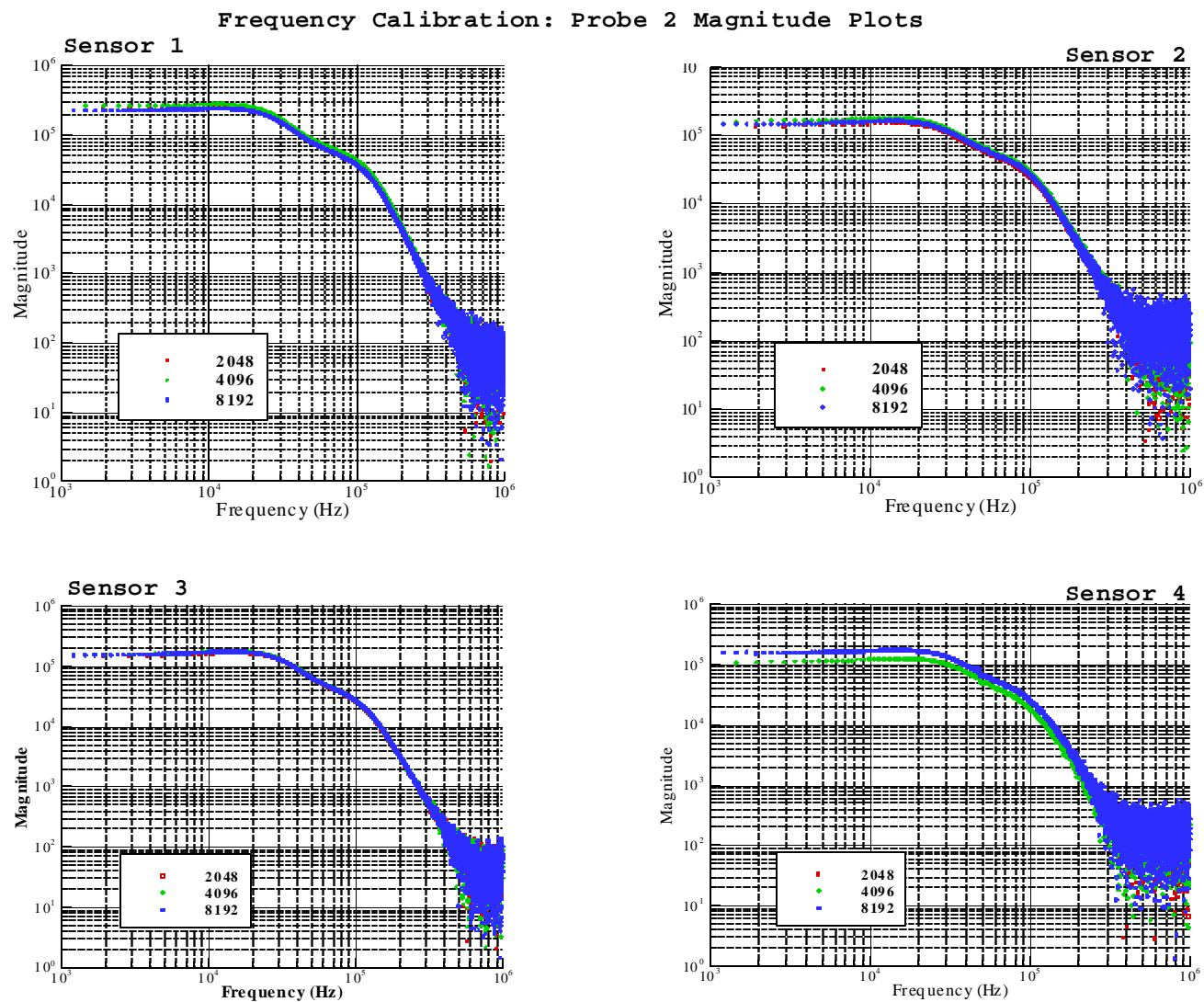


Figure 4b. Amplitude calibration for the sensor channels of the 'moving' probe.
Magnitude scale is arbitrary.

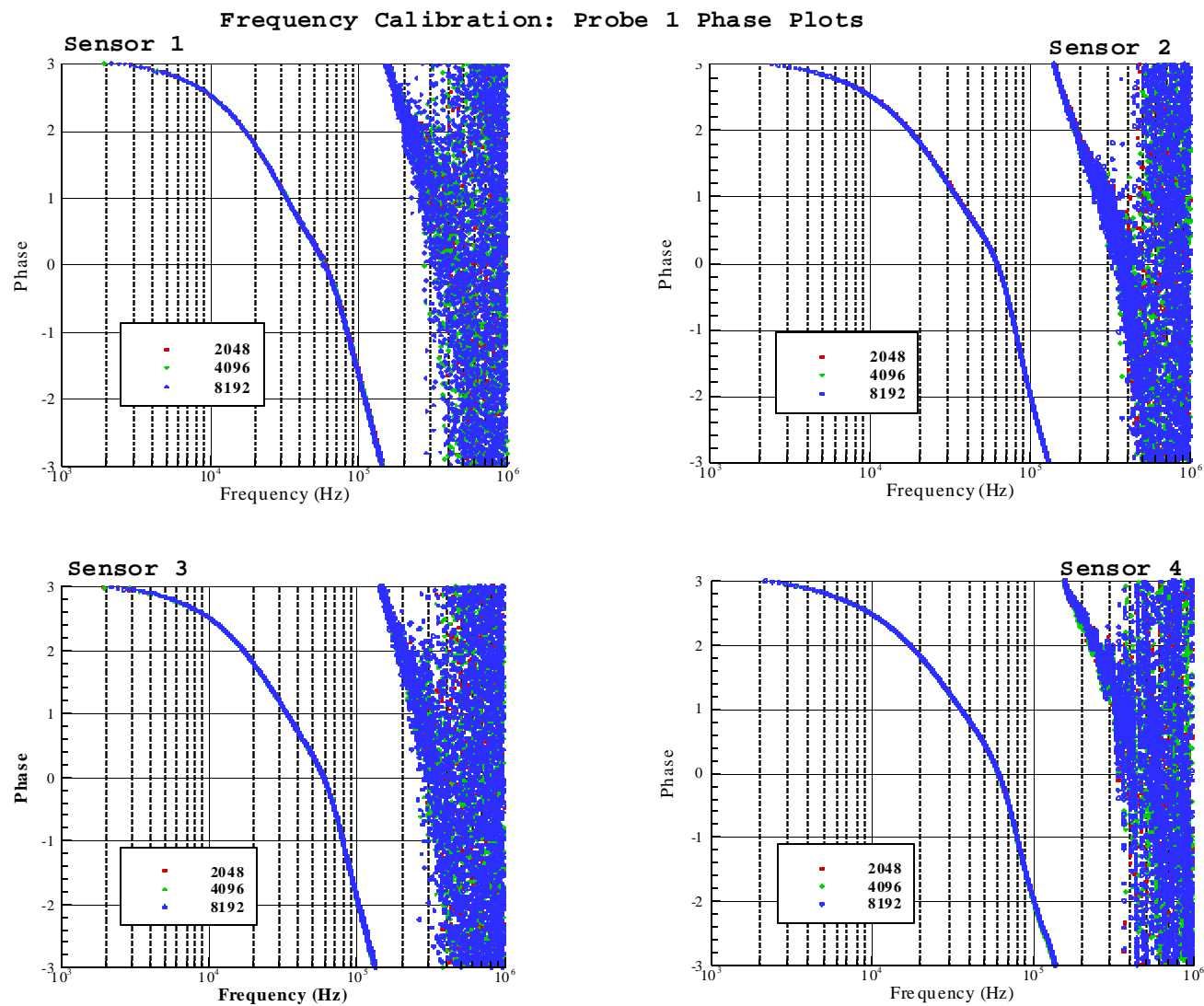


Figure 4c. Phase calibration for the sensor channels of the 'fixed' probe.

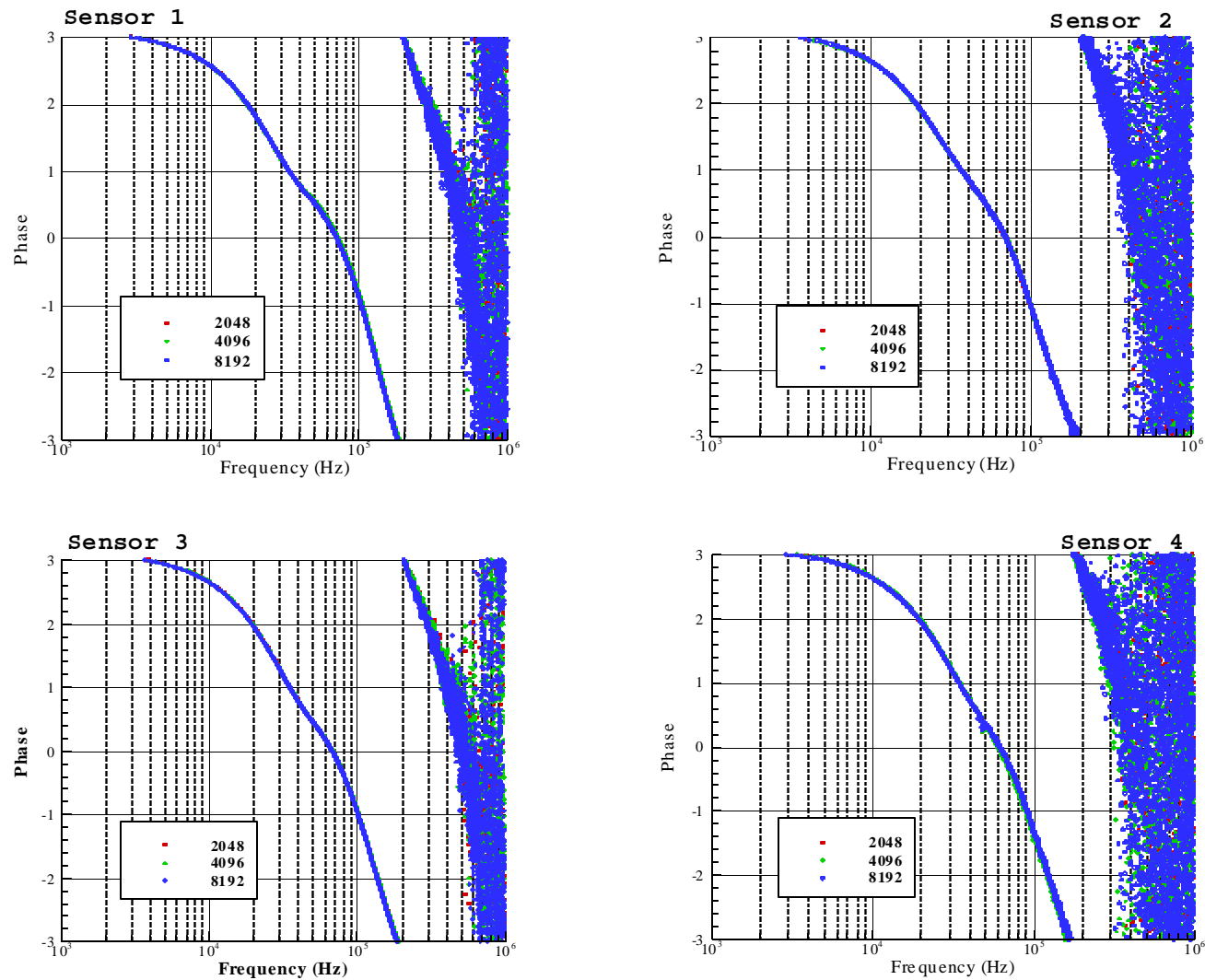


Figure 4d. Phase calibration for the sensor channels of the 'moving' probe.

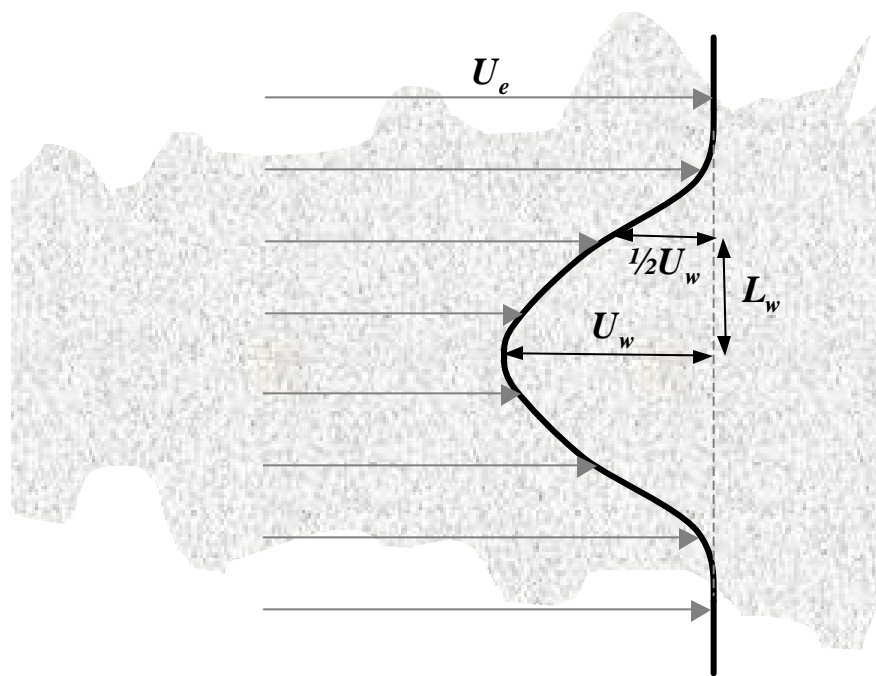


Figure 5. Definition of wake scales U_w and L_w

Figure 6. Wake parameters based on the mean U velocity profile. (a) and (b) Axial velocity deficit and half wake width vs. distance downstream of the airfoil trailing edge.

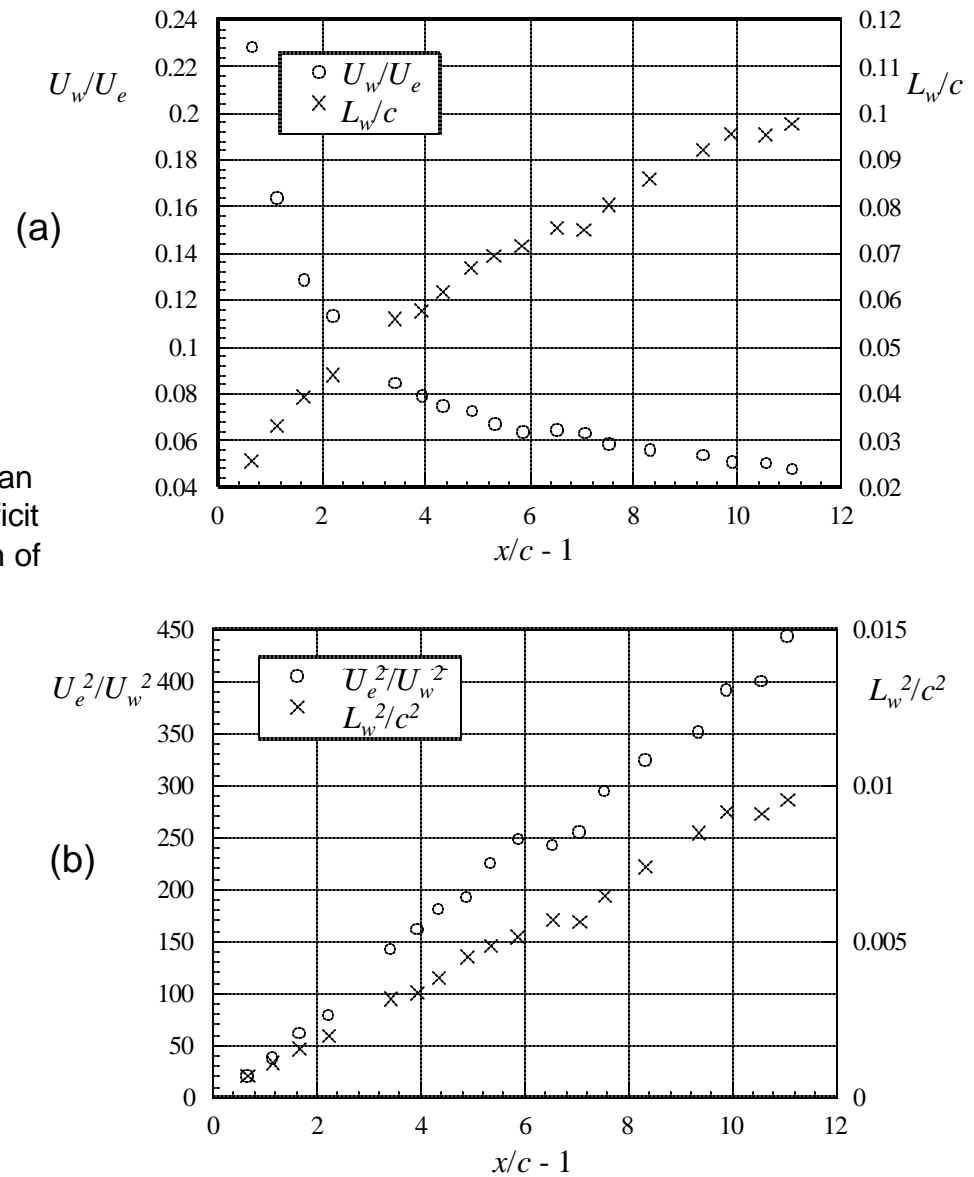
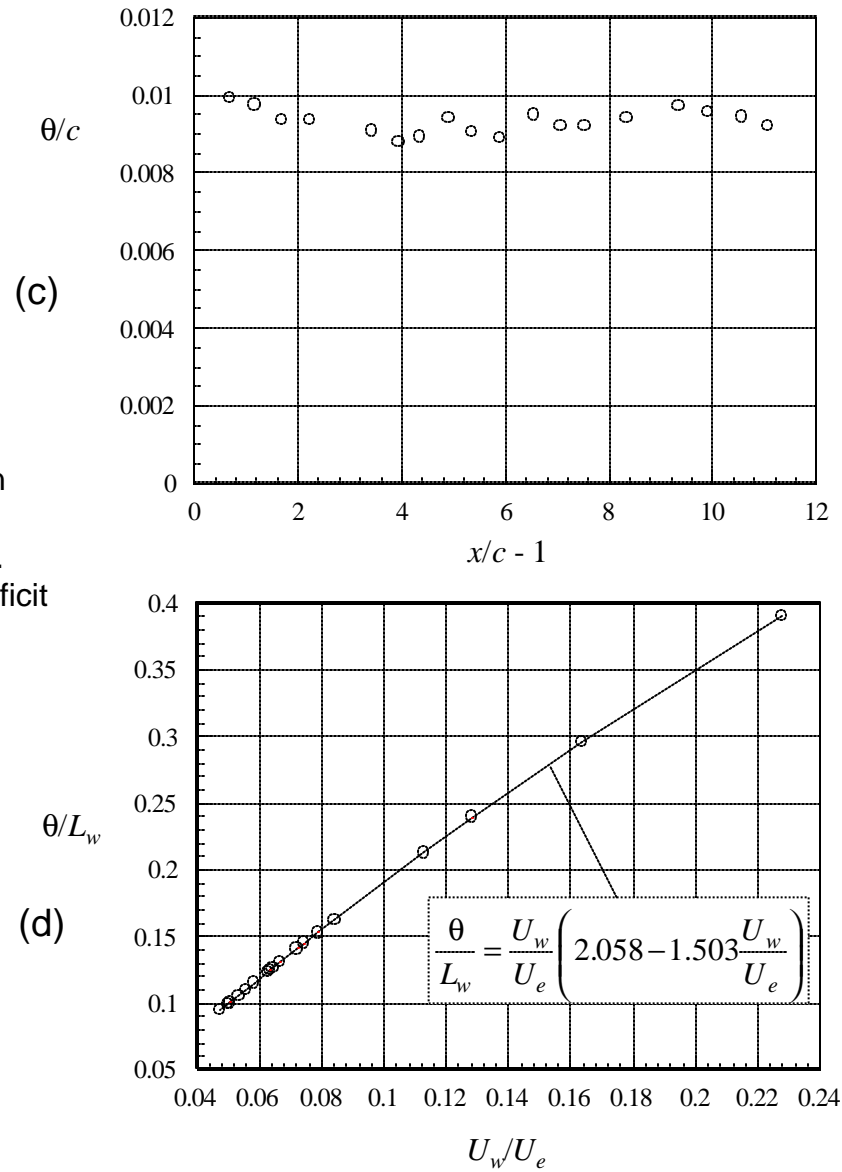


Figure 6. Wake parameters based on the mean U velocity profile. (c) Momentum thickness vs. distance downstream of the airfoil trailing edge. (d) Inverse half-wake width vs. axial velocity deficit following Wygnanski *et al.* (1986).



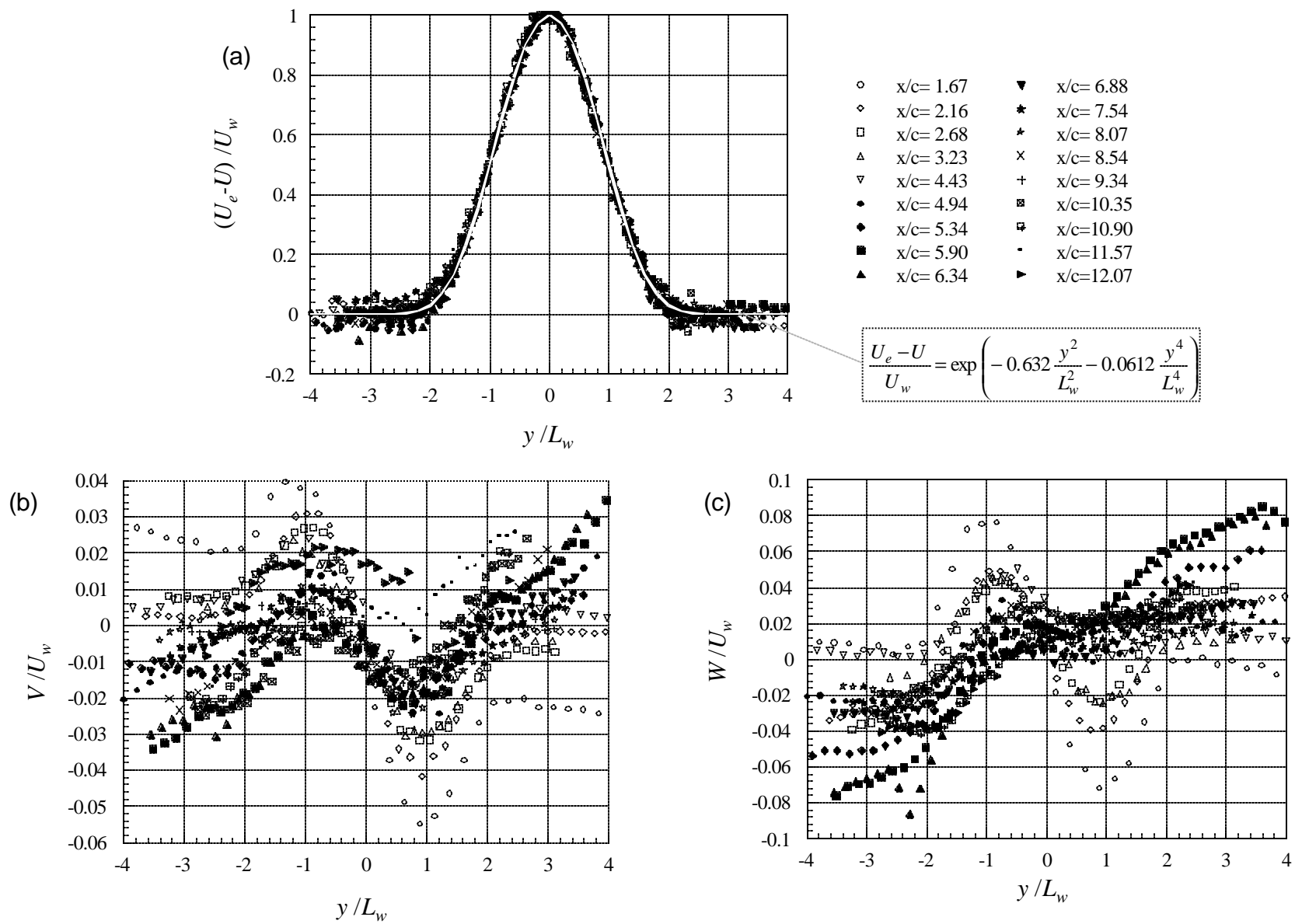


Figure 7. Mean velocity profiles normalized on half-width and centerline axial velocity deficit.

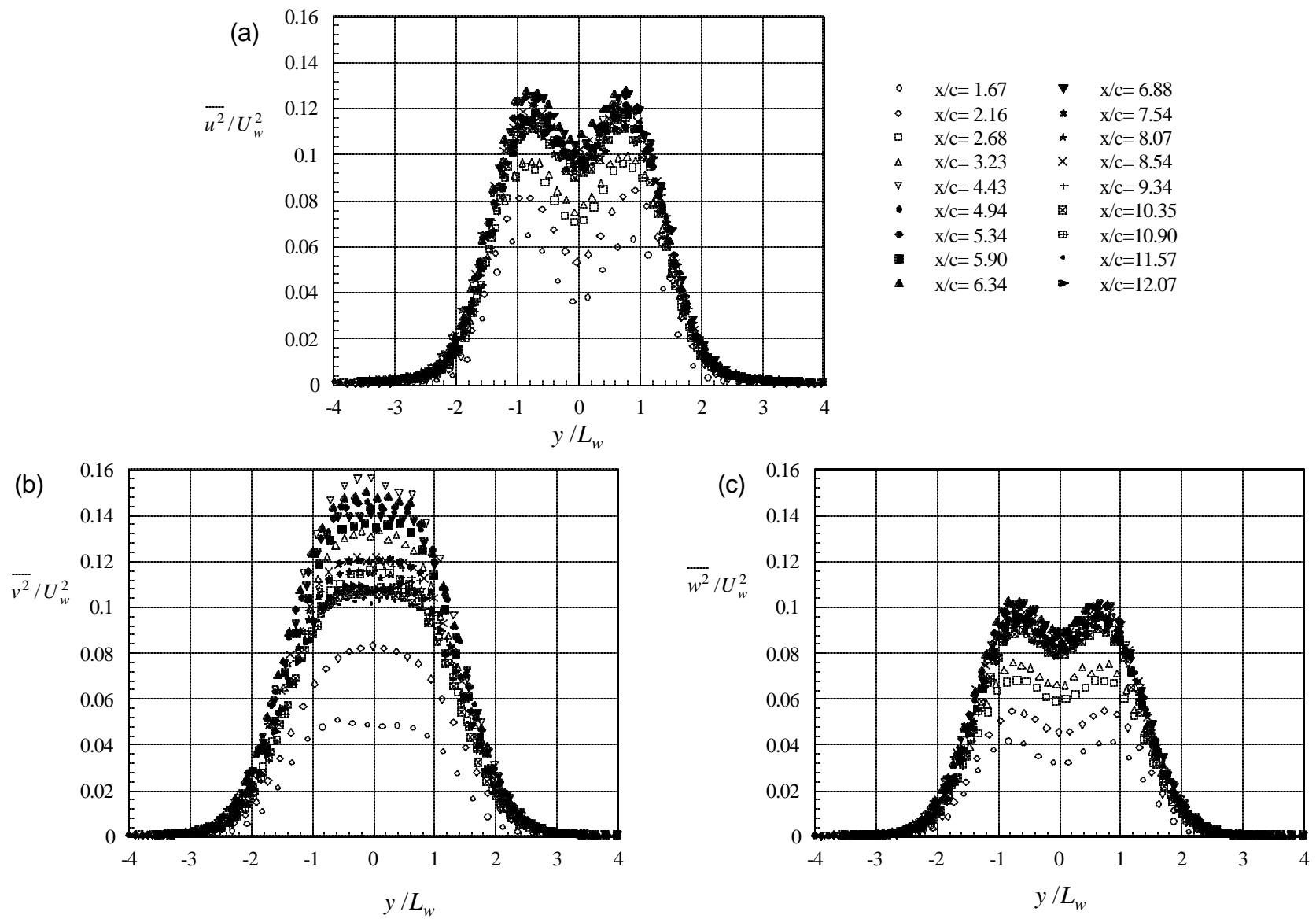


Figure 8. Turbulence stress profiles normalized on half-width and centerline axial velocity deficit.

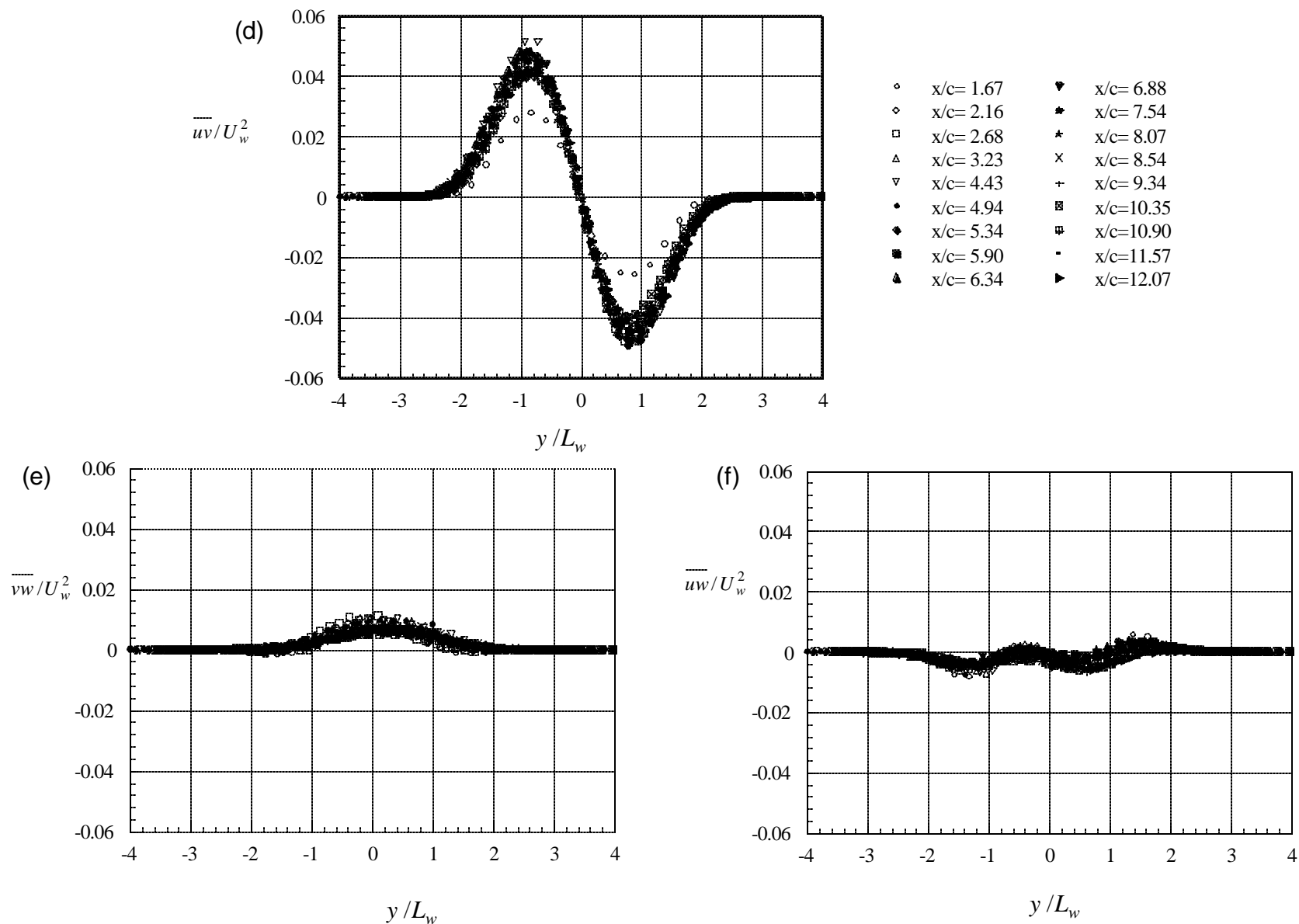


Figure 8. Turbulence stress profiles normalized on half-width and centerline axial velocity deficit.

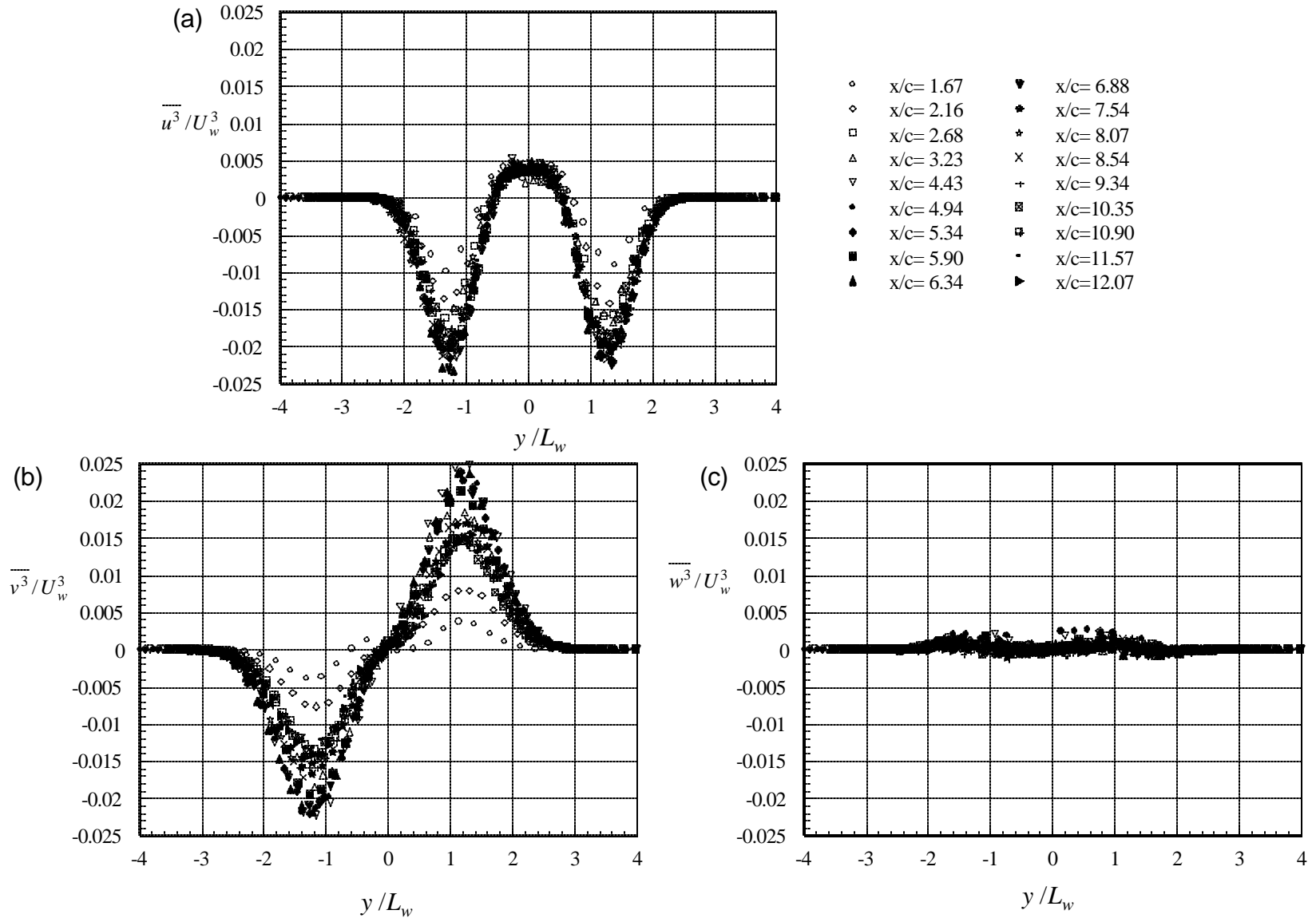


Figure 9. Triple product profiles normalized on half-width and centerline axial velocity deficit.

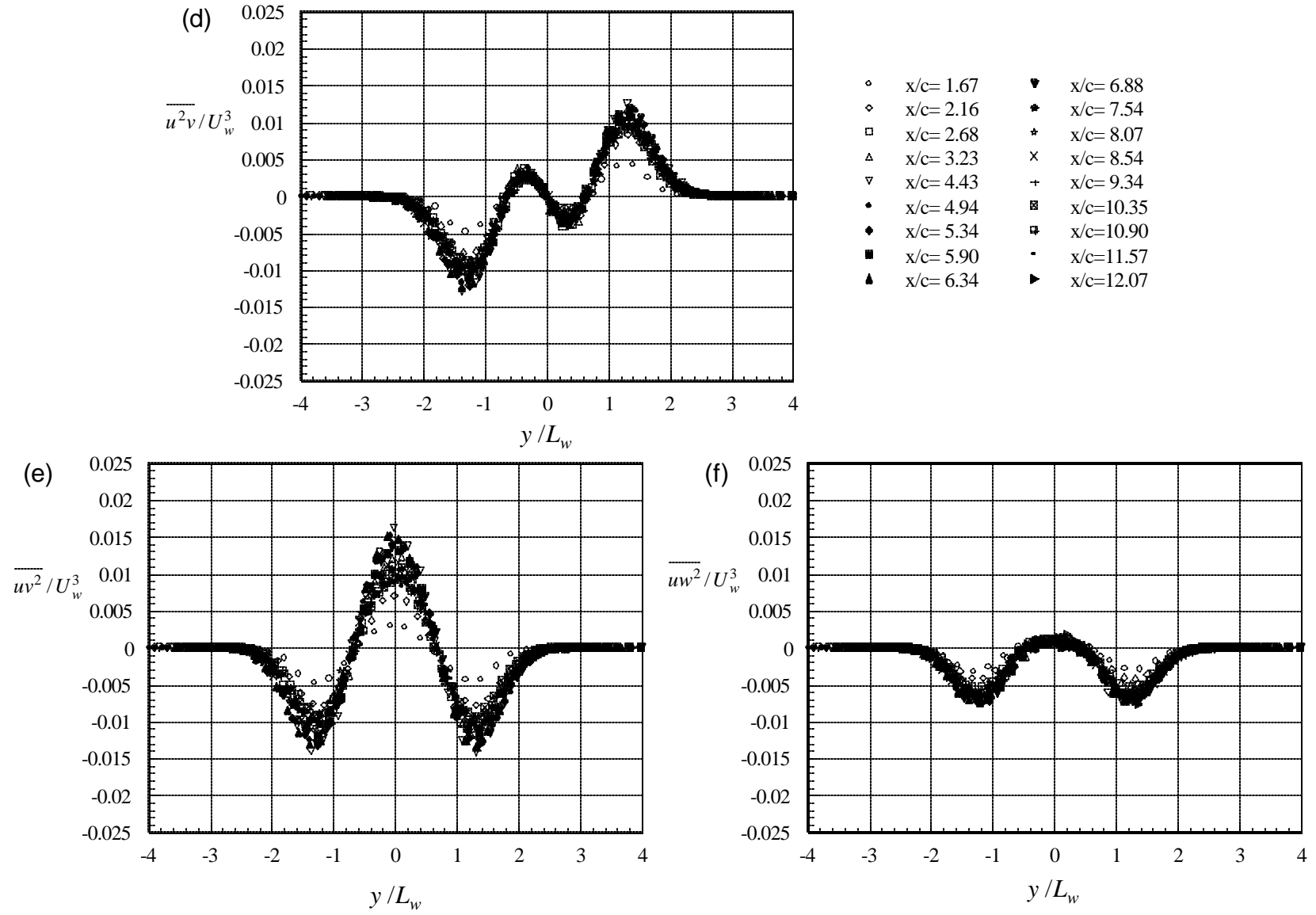


Figure 9. Triple product profiles normalized on half-width and centerline axial velocity deficit.

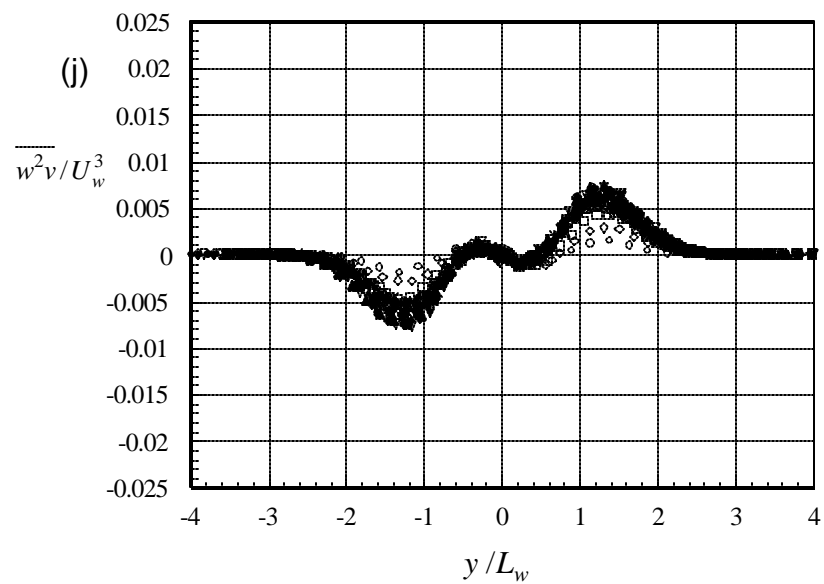
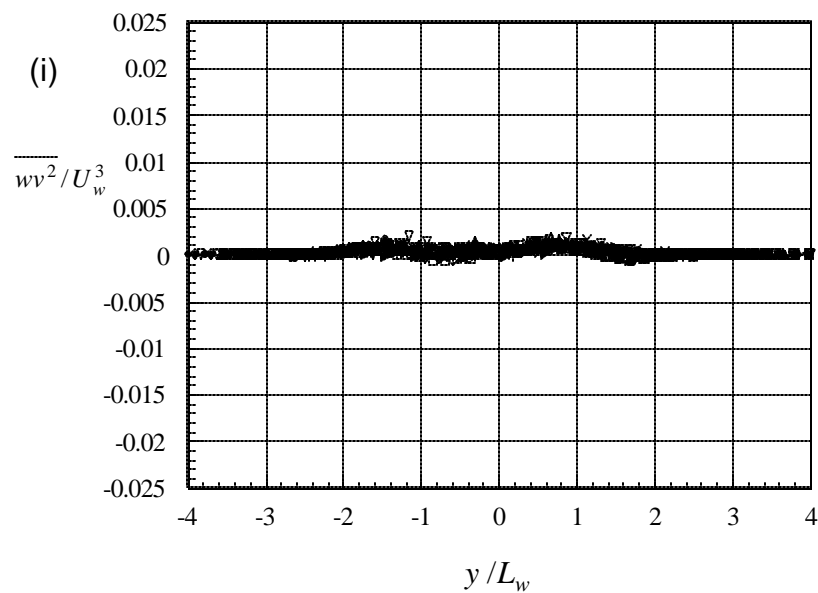
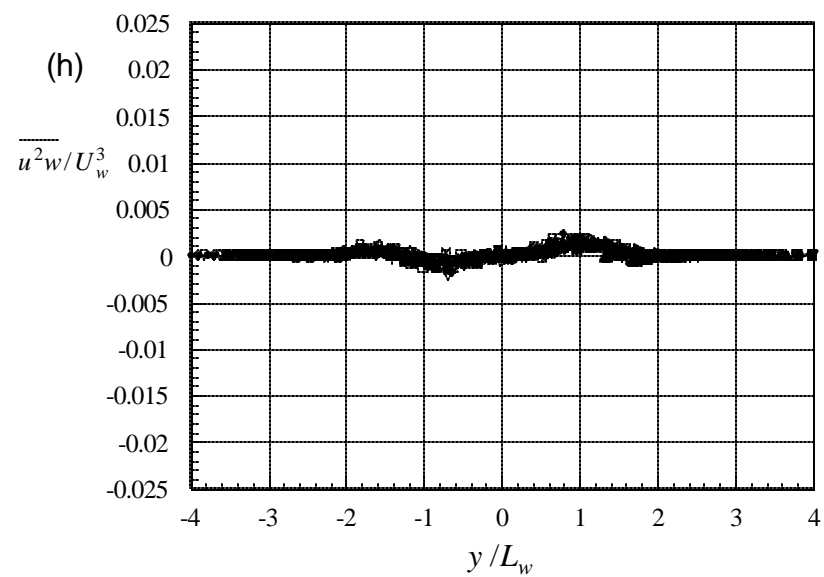
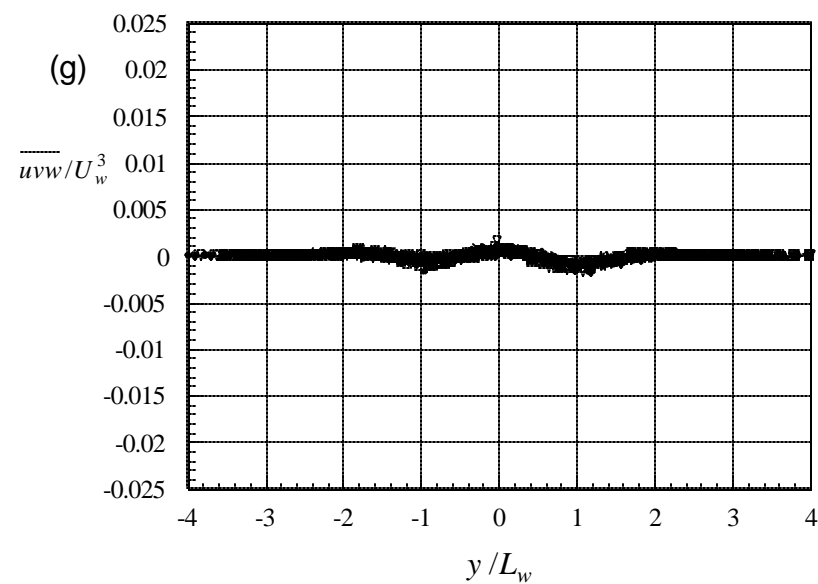


Figure 9. Triple product profiles normalized on half-width and centerline axial velocity deficit.

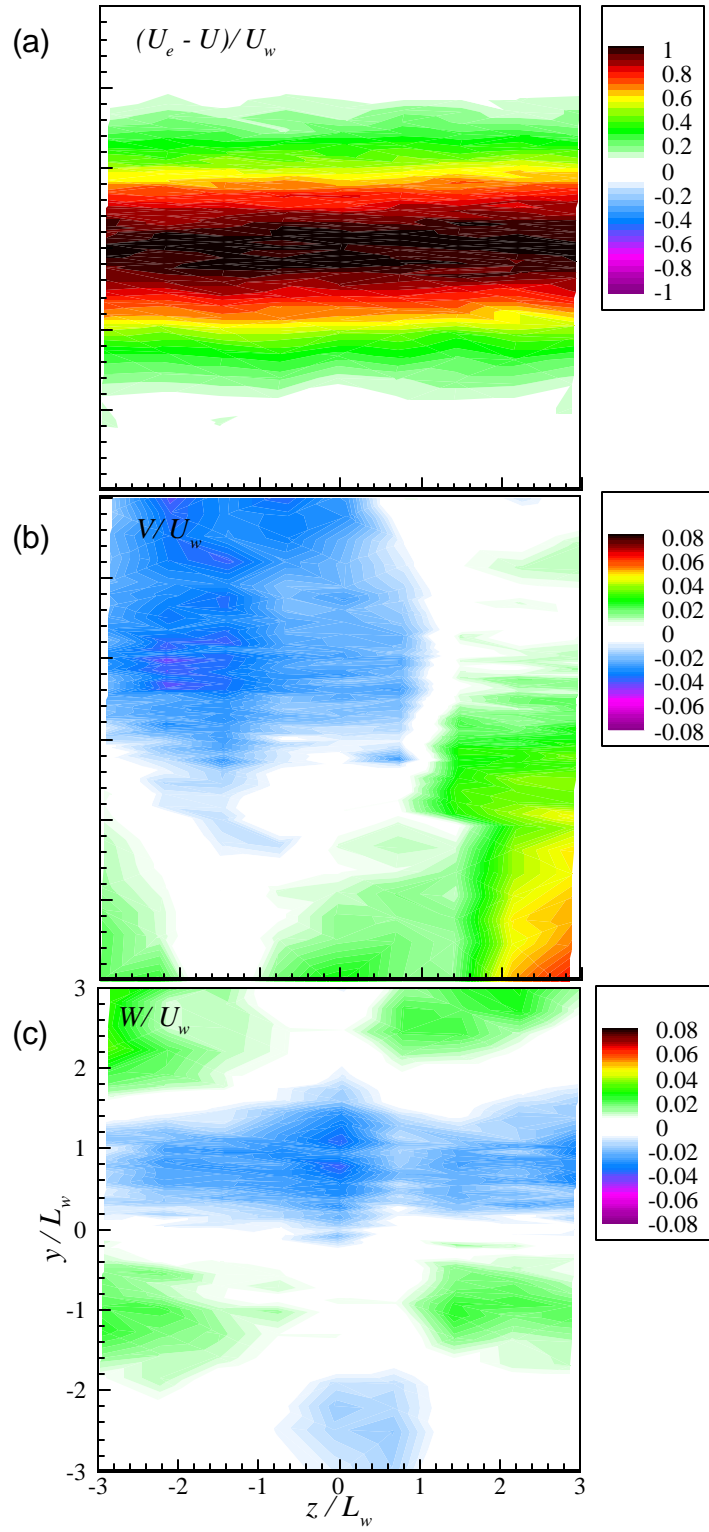


Figure 10. Mean velocity cross-sections at $z/c=9.34$ normalized on half-width and centerline axial velocity deficit.

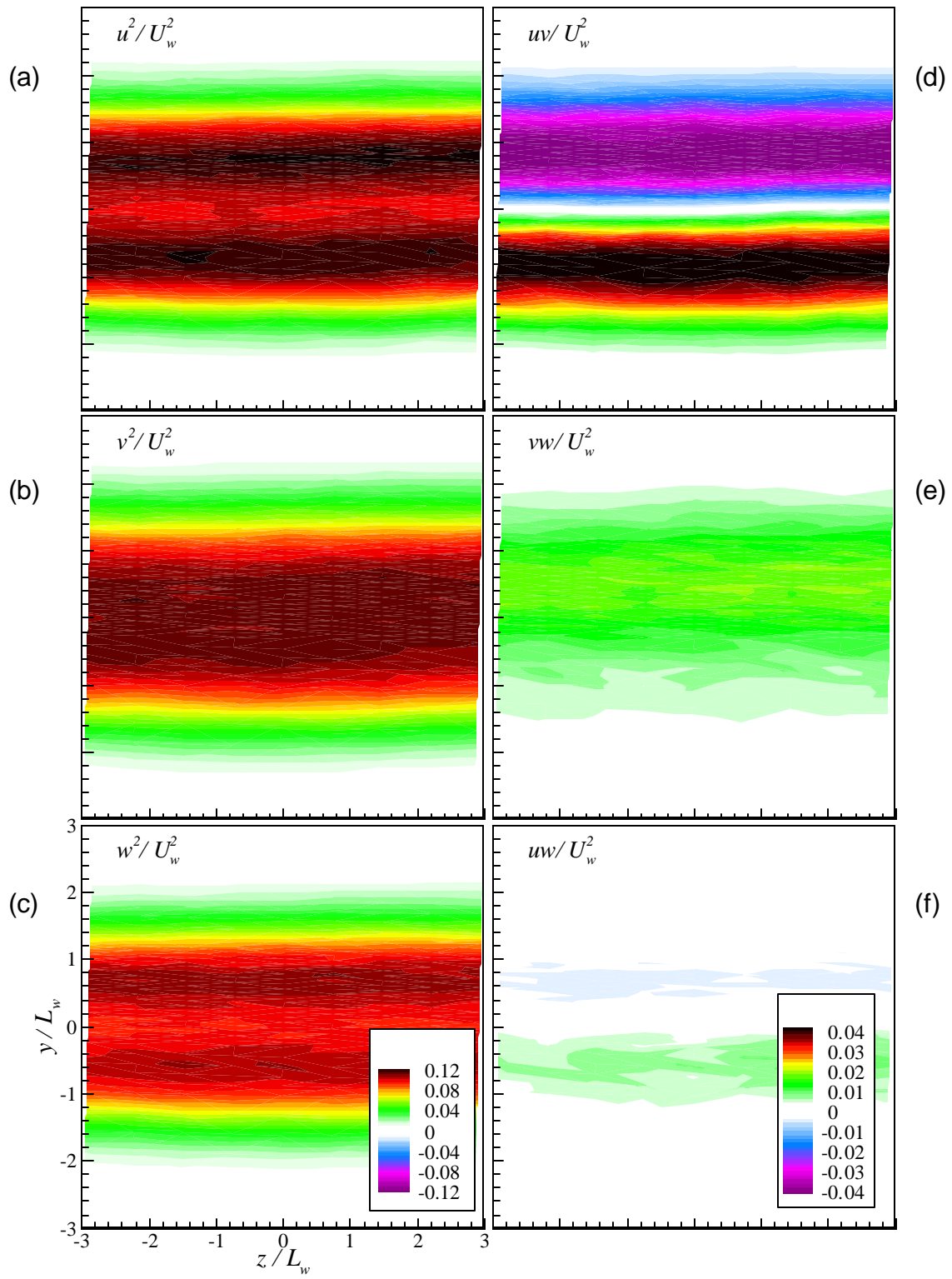


Figure 11. Turbulence stress cross-sections at $z/c=9.34$ normalized on half-width and centerline axial velocity deficit.

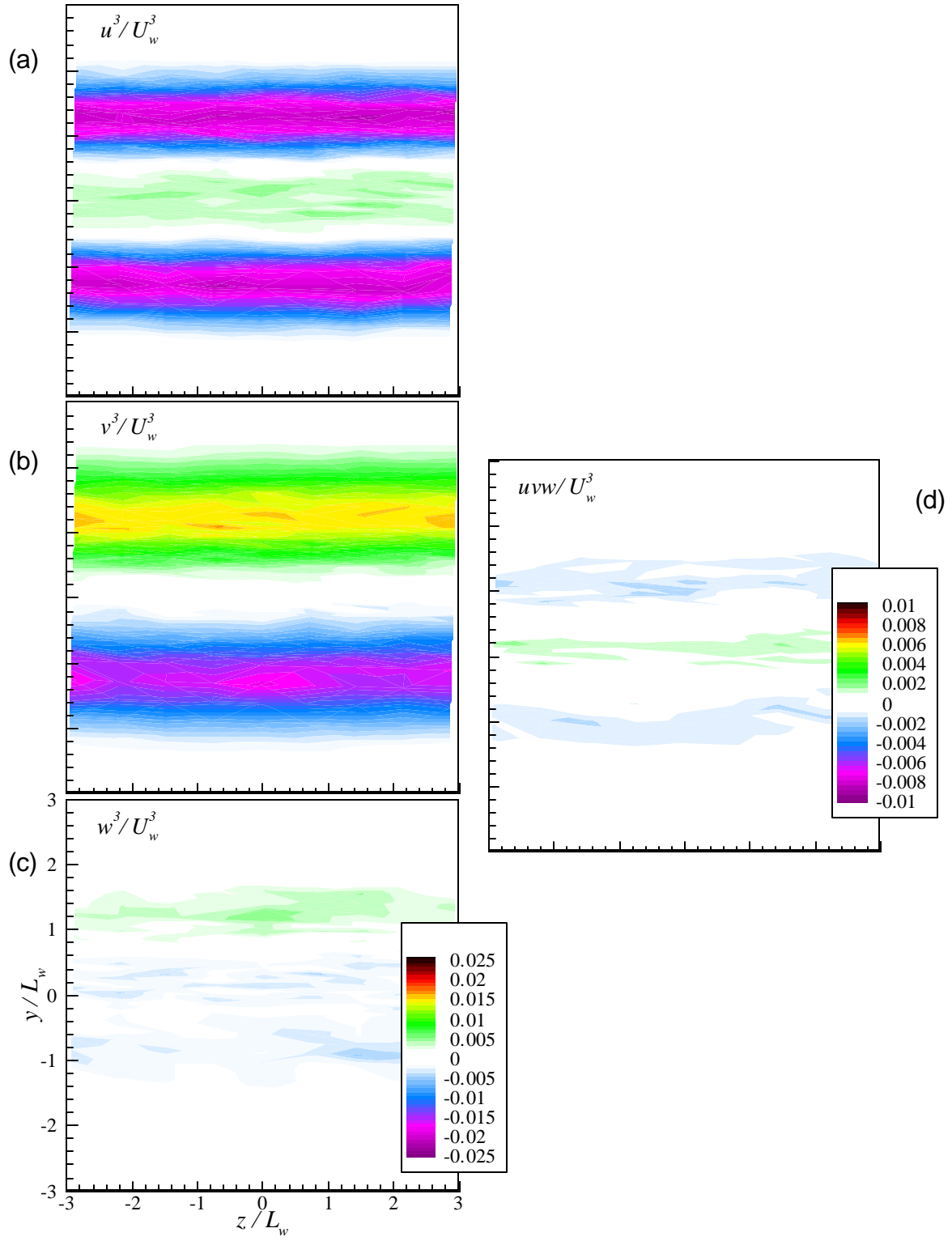


Figure 12. Triple product cross-sections at $z/c=9.34$ normalized on half-width and centerline axial velocity deficit.

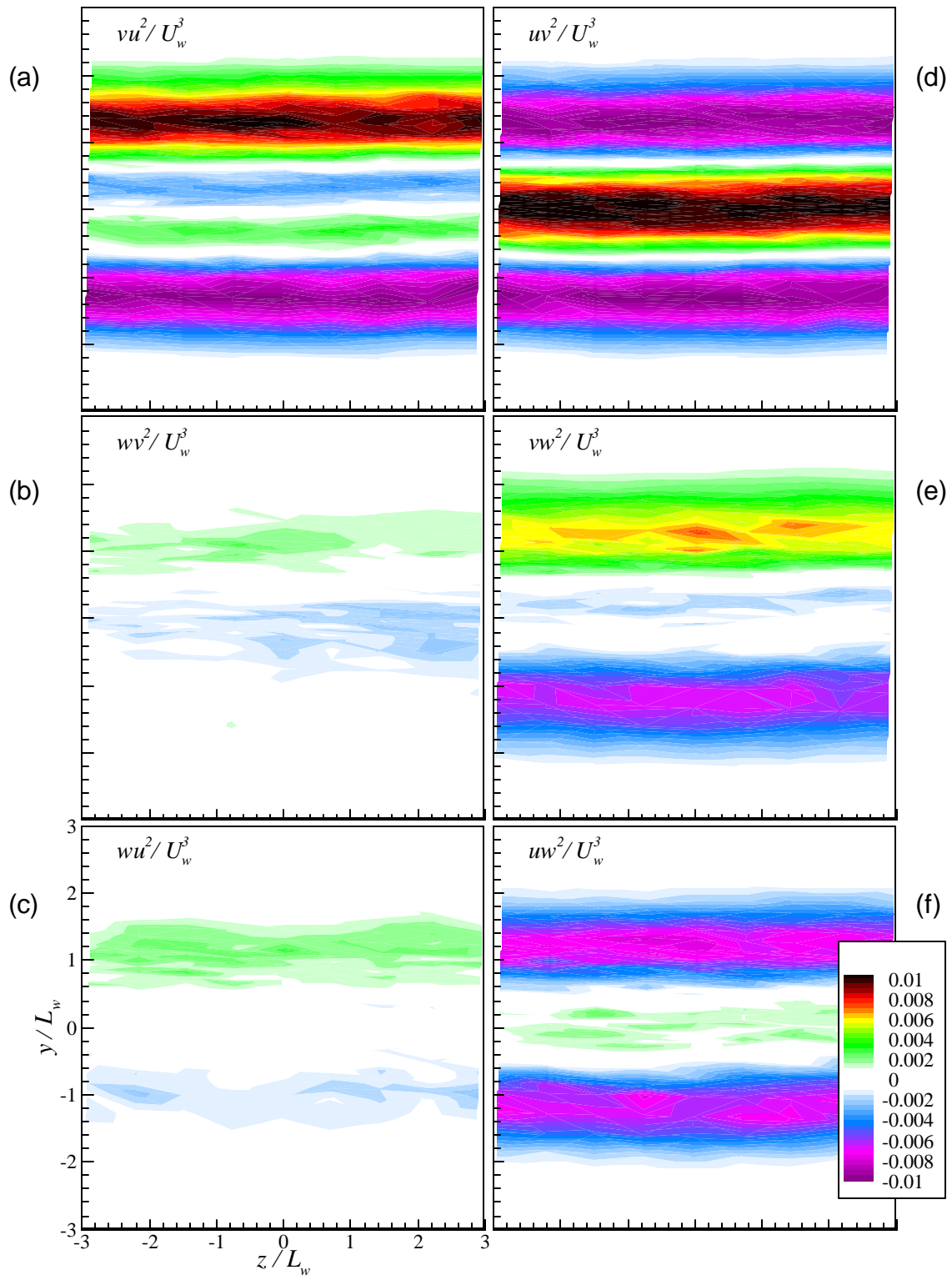


Figure 12. Triple product cross-sections at $z/c=9.34$ normalized on half-width and centerline axial velocity deficit.

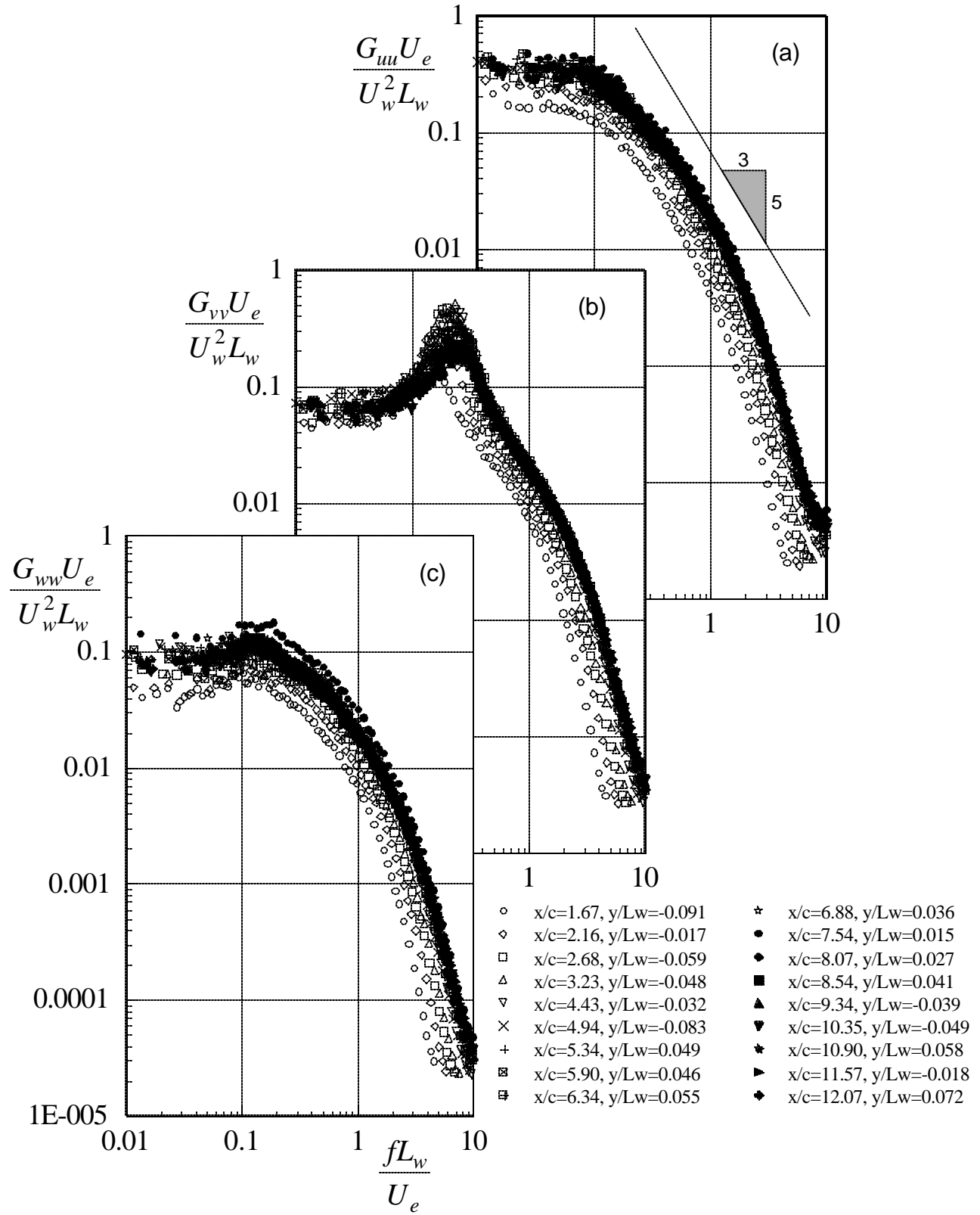


Figure 13. Velocity spectra measured near the flow centerline normalized on half-width and centerline axial velocity deficit.

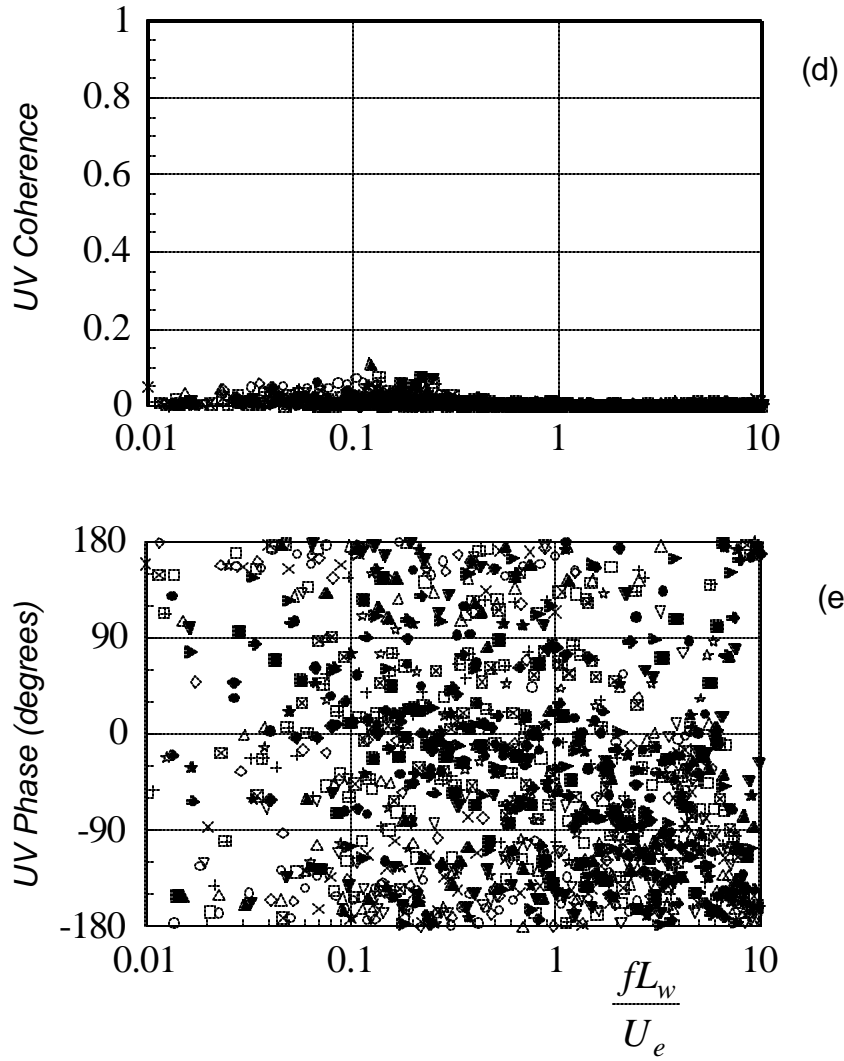


Figure 13. Velocity spectra measured near the flow centerline normalized on half-width and centerline axial velocity deficit. Legend in figure 13(c)

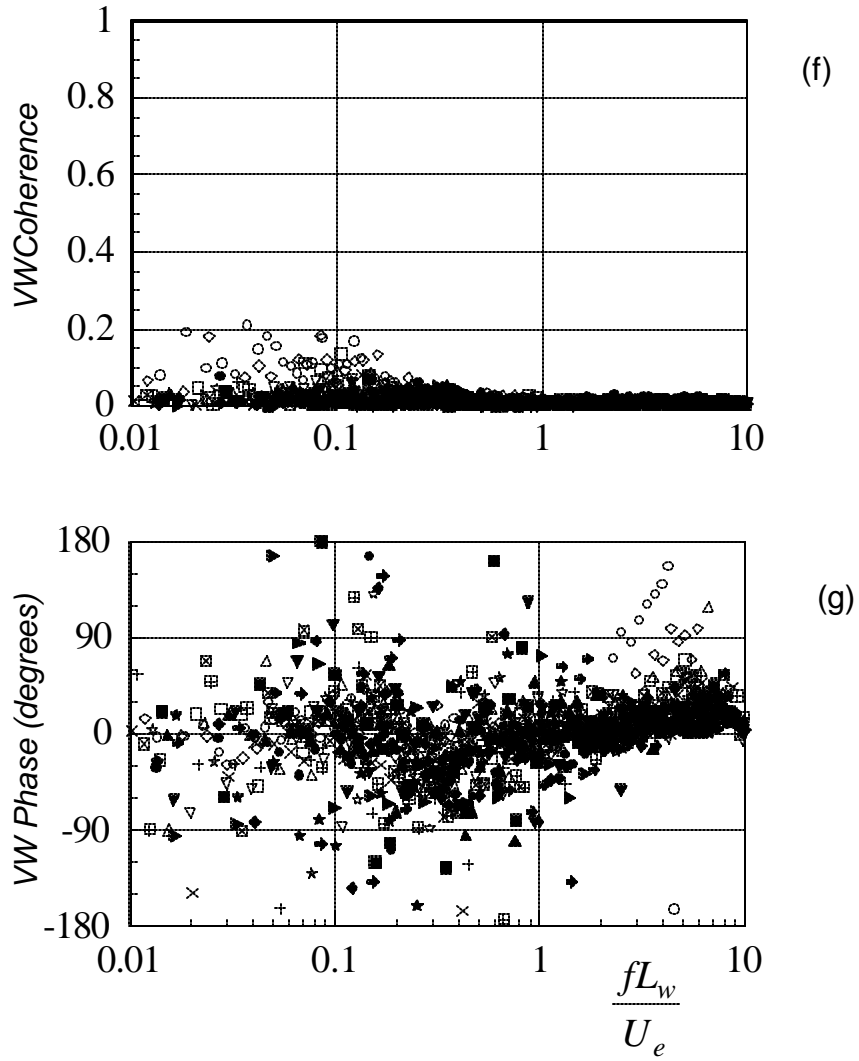


Figure 13. Velocity spectra measured near the flow centerline normalized on half-width and centerline axial velocity deficit. Legend in figure 13(c)

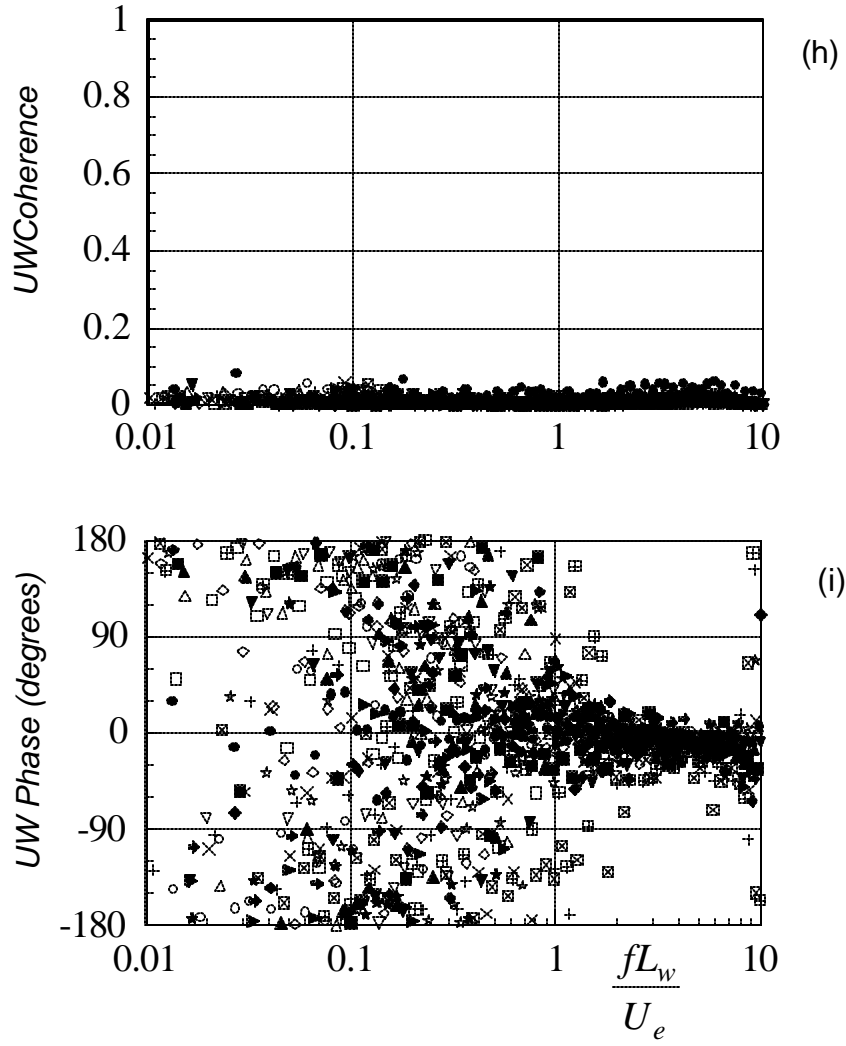


Figure 13. Velocity spectra measured near the flow centerline normalized on half-width and centerline axial velocity deficit. Legend in figure 13(c)

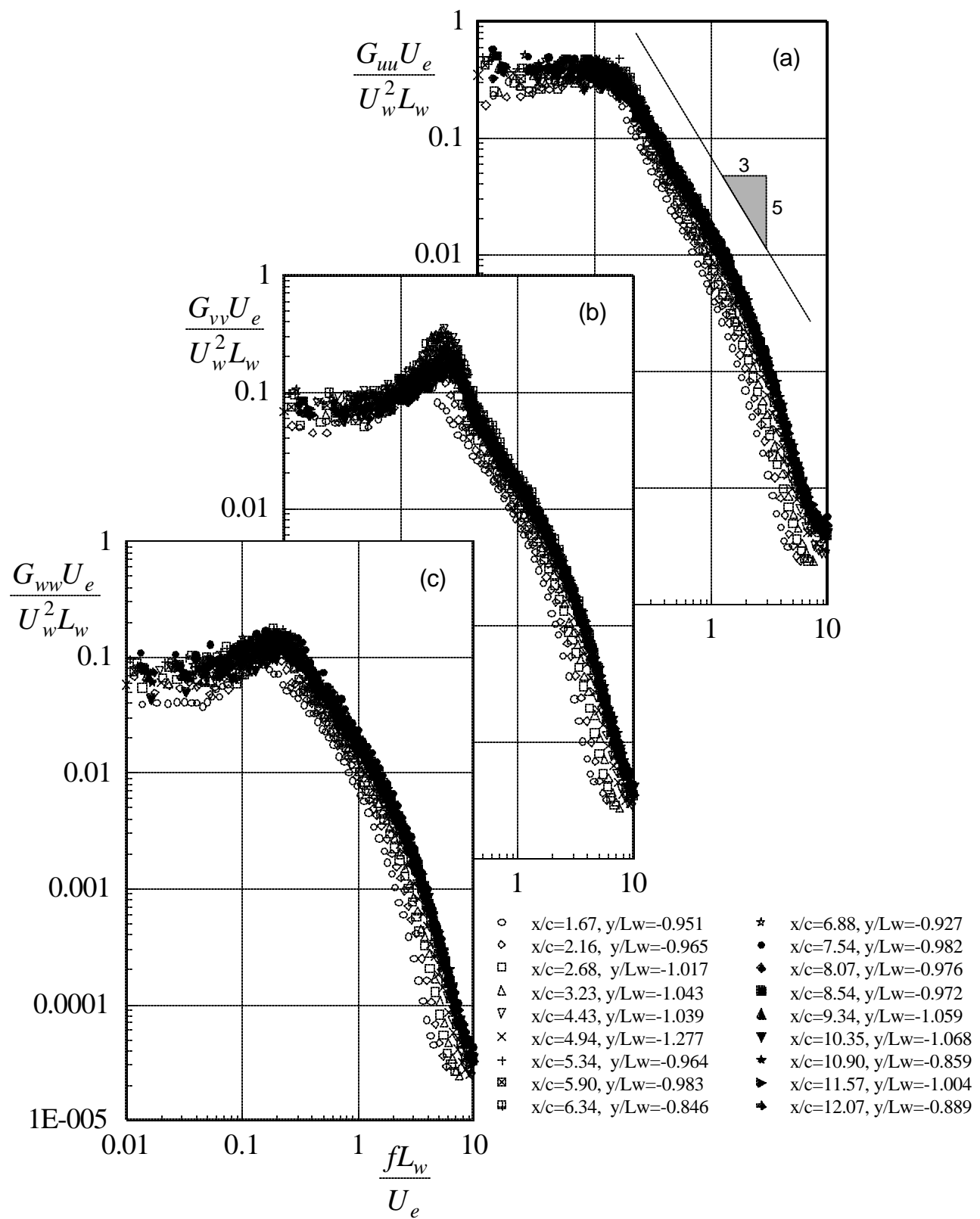


Figure 14. Velocity spectra measured approximately one half-wake width from the flow centerline, normalized on half-width and centerline axial velocity deficit.

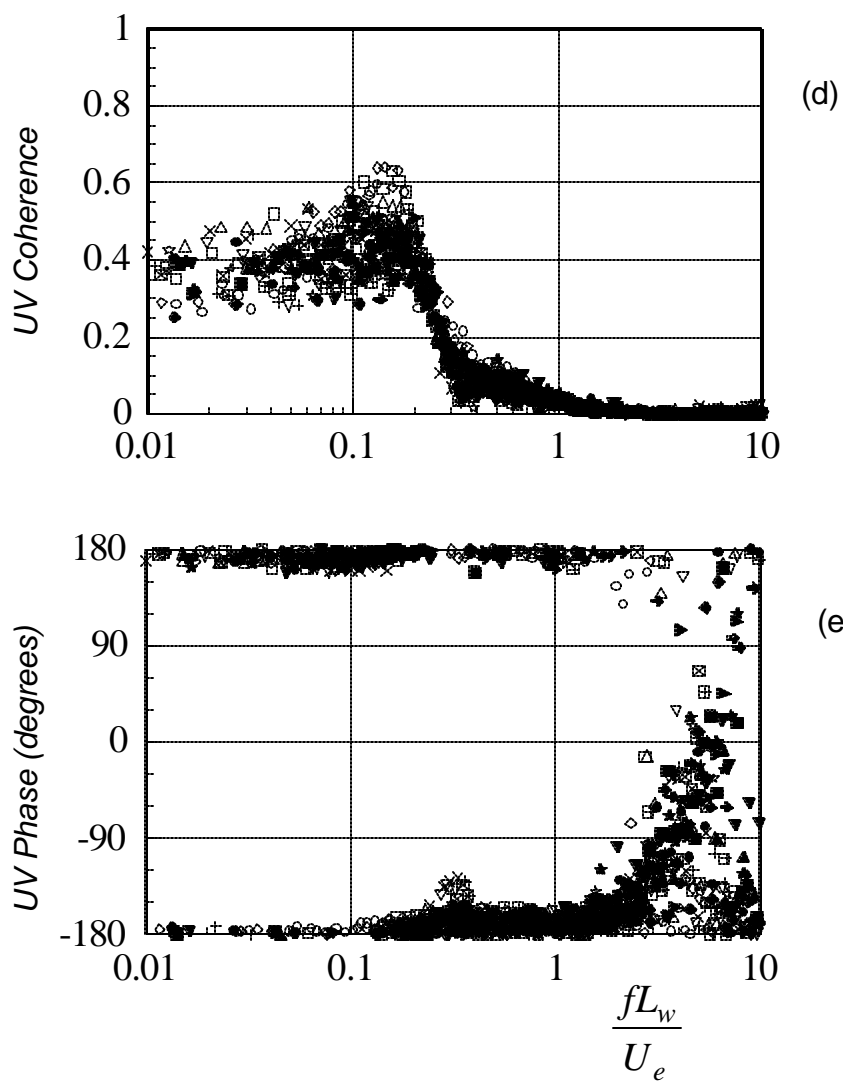


Figure 14. Velocity spectra measured approximately one half-wake width from the flow centerline, normalized on half-width and centerline axial velocity deficit. Legend in figure 14(c)

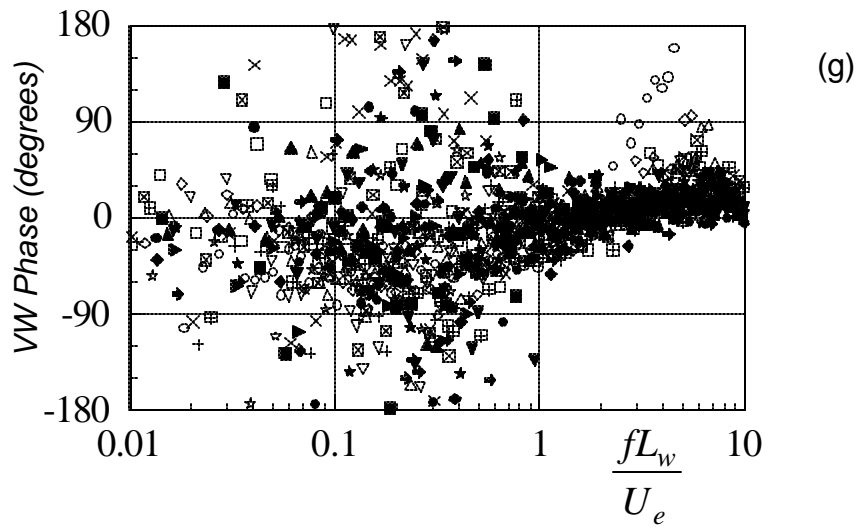
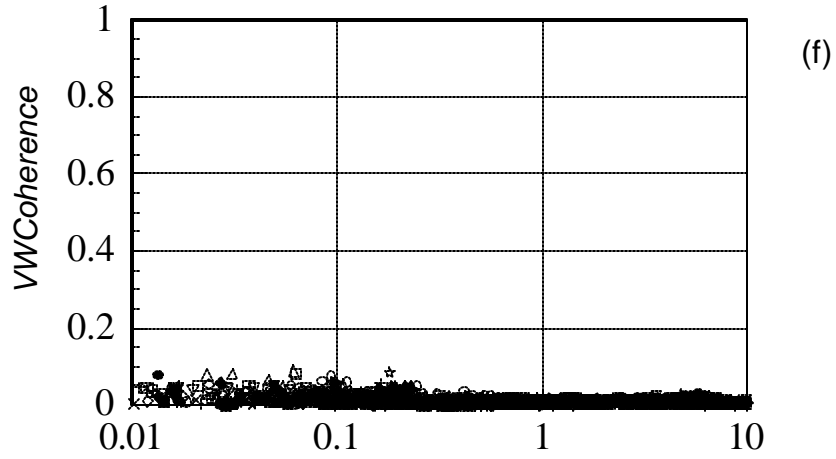


Figure 14. Velocity spectra measured approximately one half-wake width from the flow centerline, normalized on half-width and centerline axial velocity deficit.
Legend in figure 14(c)

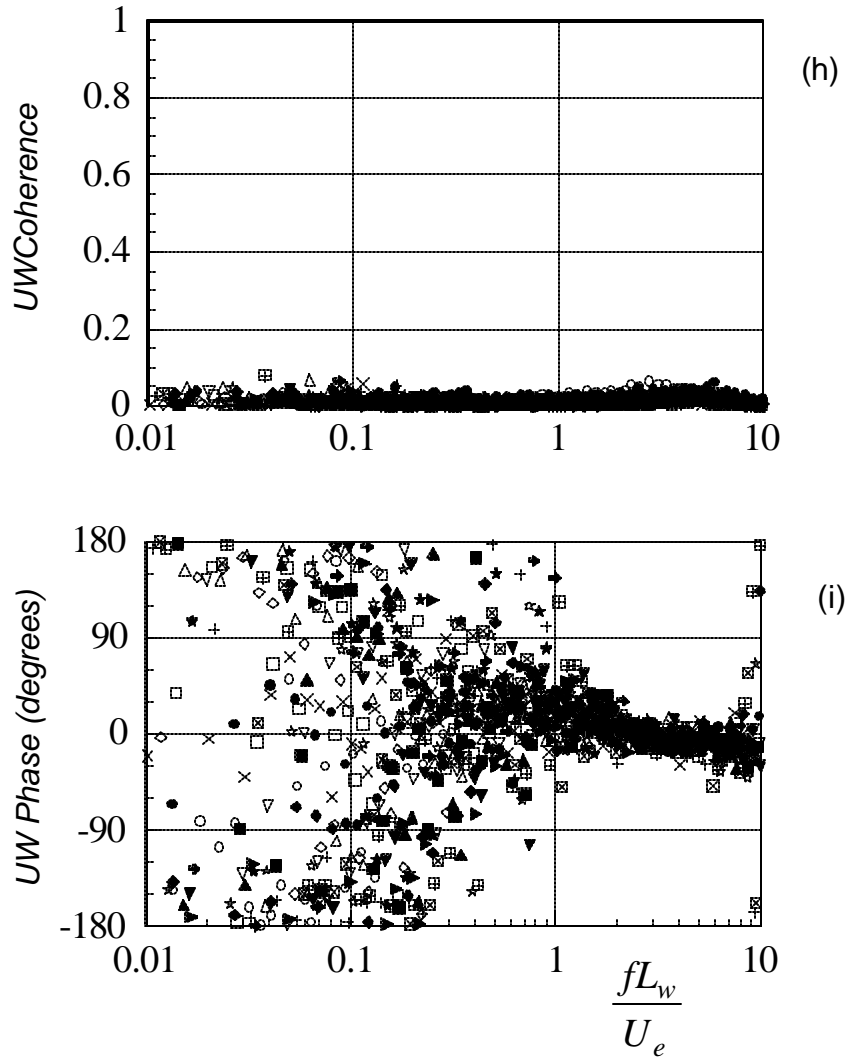


Figure 14. Velocity spectra measured approximately one half-wake width from the flow centerline, normalized on half-width and centerline axial velocity deficit. Legend in figure 14(c)

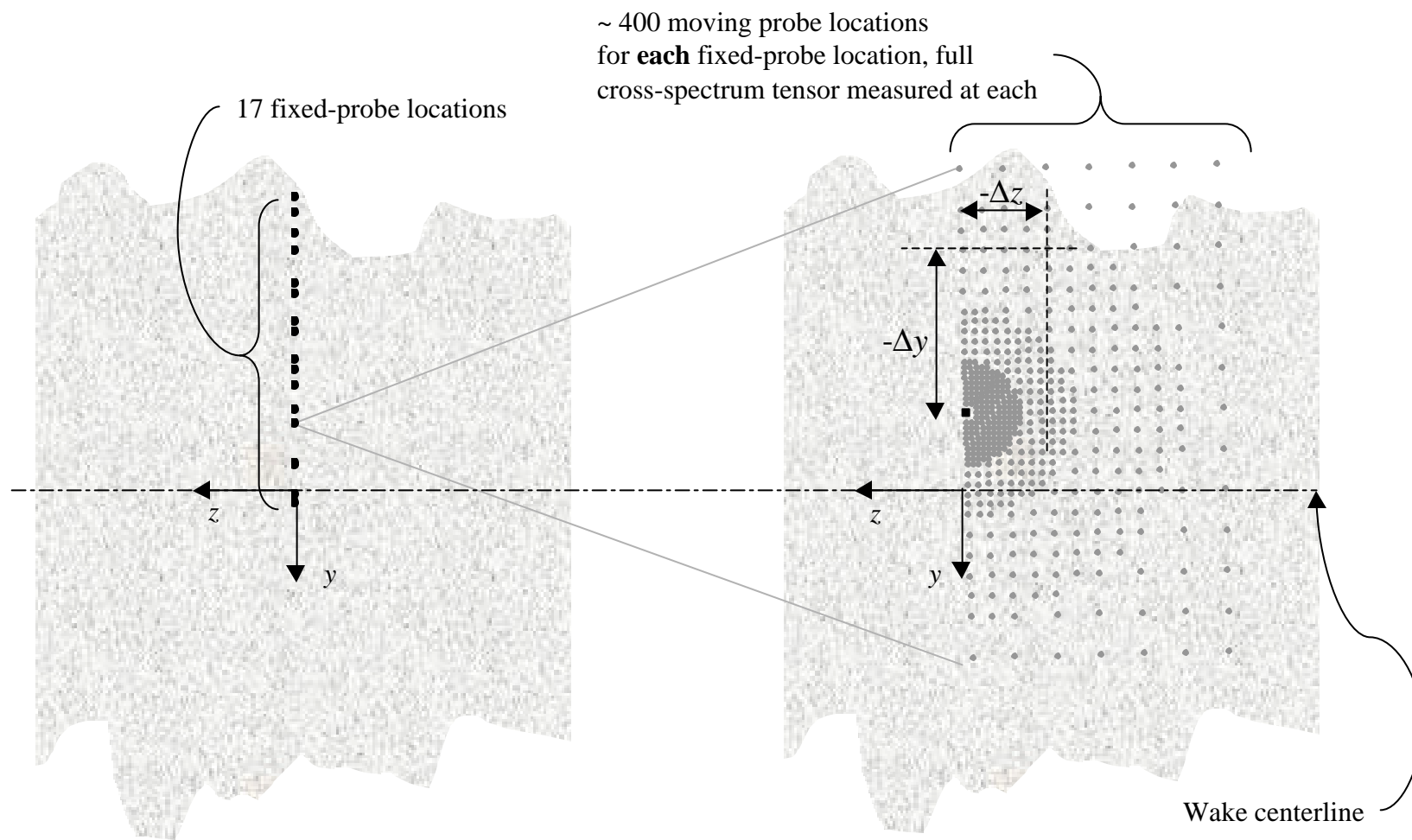


Figure 15. Schematic of the wake cross section illustrating the 400-point grid measured for each of the 17 fixed probe locations

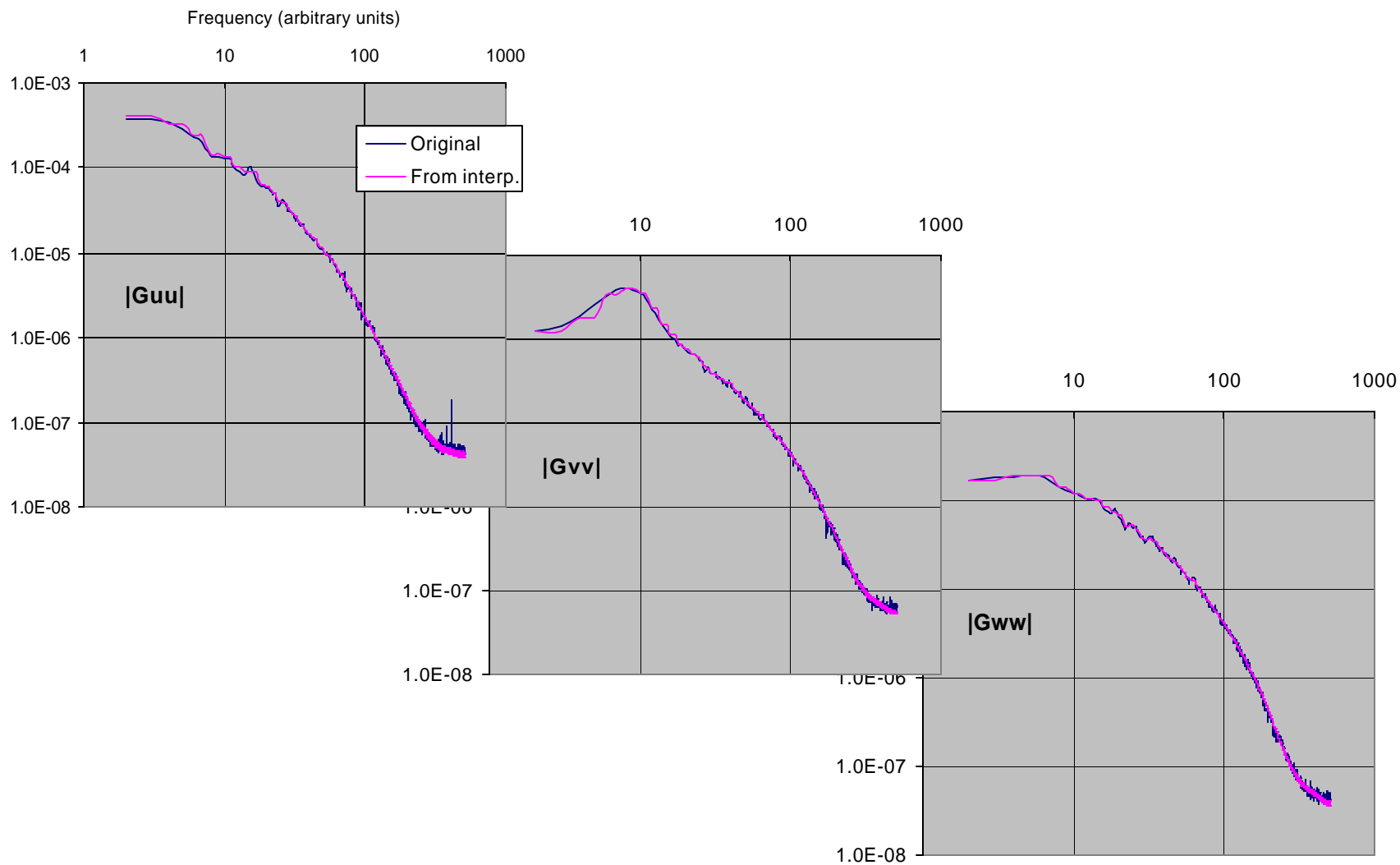


Figure 16a. Comparison of original velocity autospectra with estimates recreated from the interpolated data. $x/c=9.33$, $y/L_w=0.077$

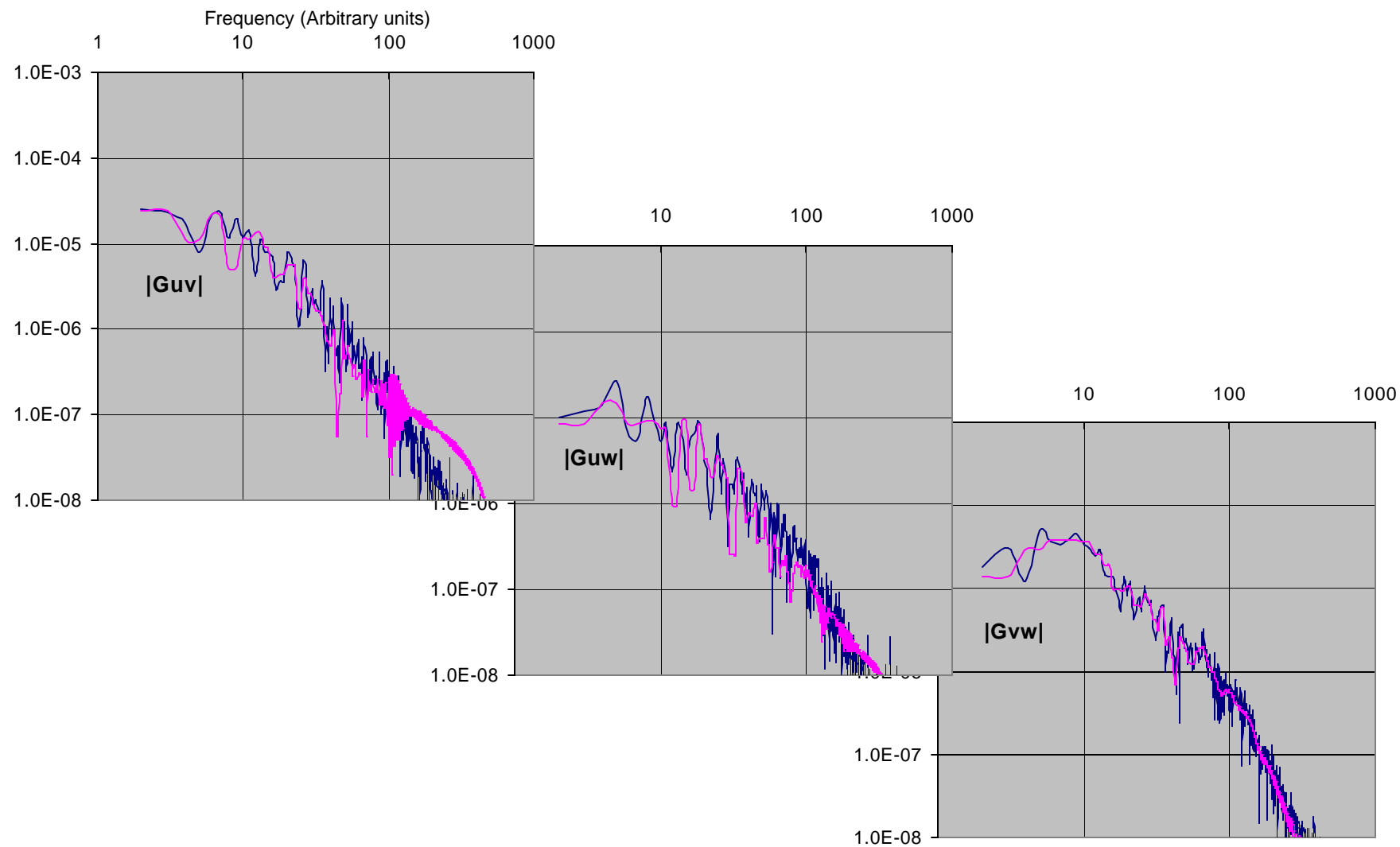


Figure 16b. Comparison of original velocity cross-spectra with estimates recreated from the interpolated data. $x/c=9.33$, $y/L_w=0.077$

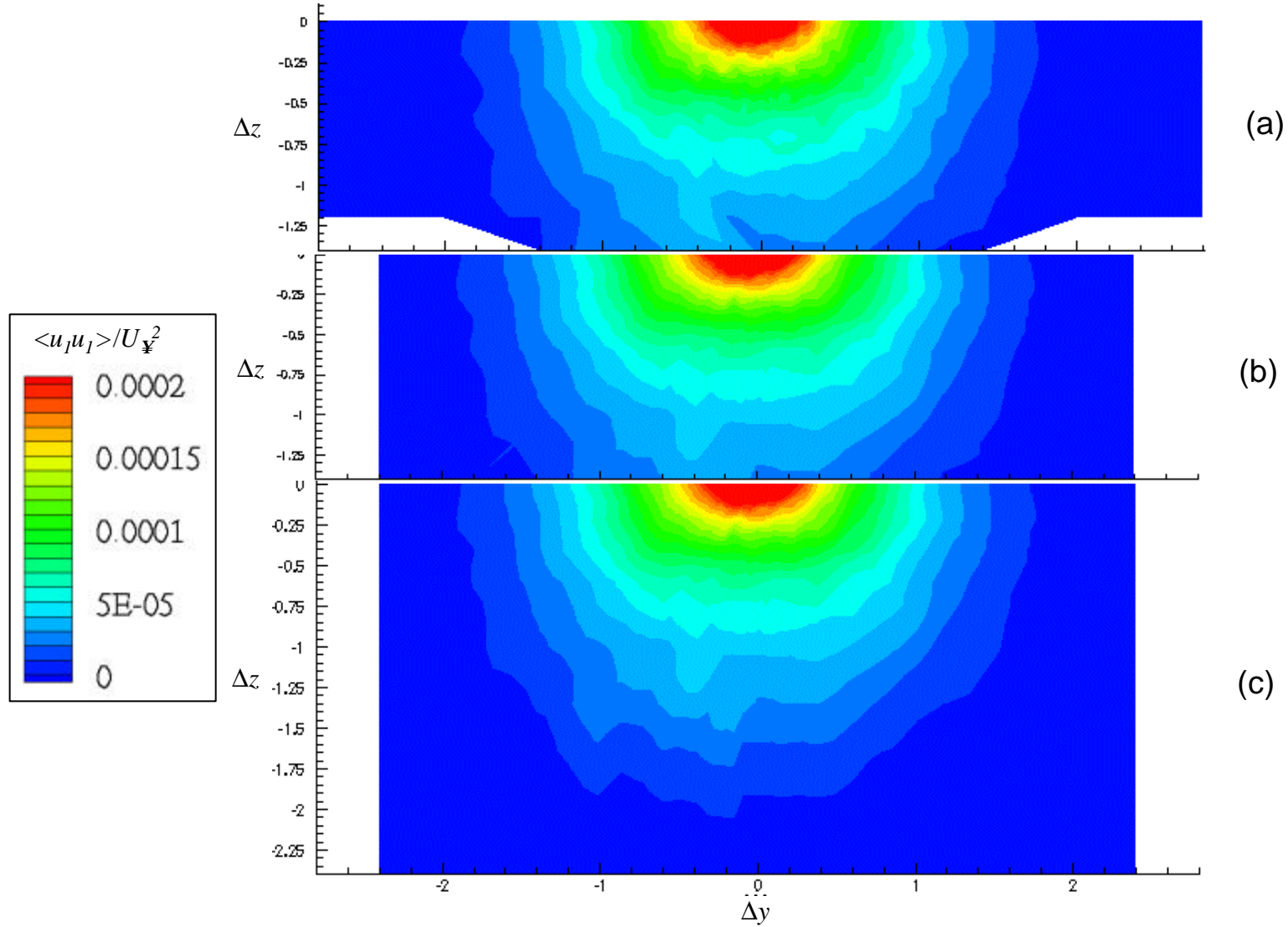


Figure 17. Comparison of zero-time delay correlation maps for u for $y/L_w=0.077$.
 (a) Raw data, (b) recreated from interpolation, (c) same as (b) with Gaussian extrapolation
 Distances in inches, $L_w=0.686$ inches

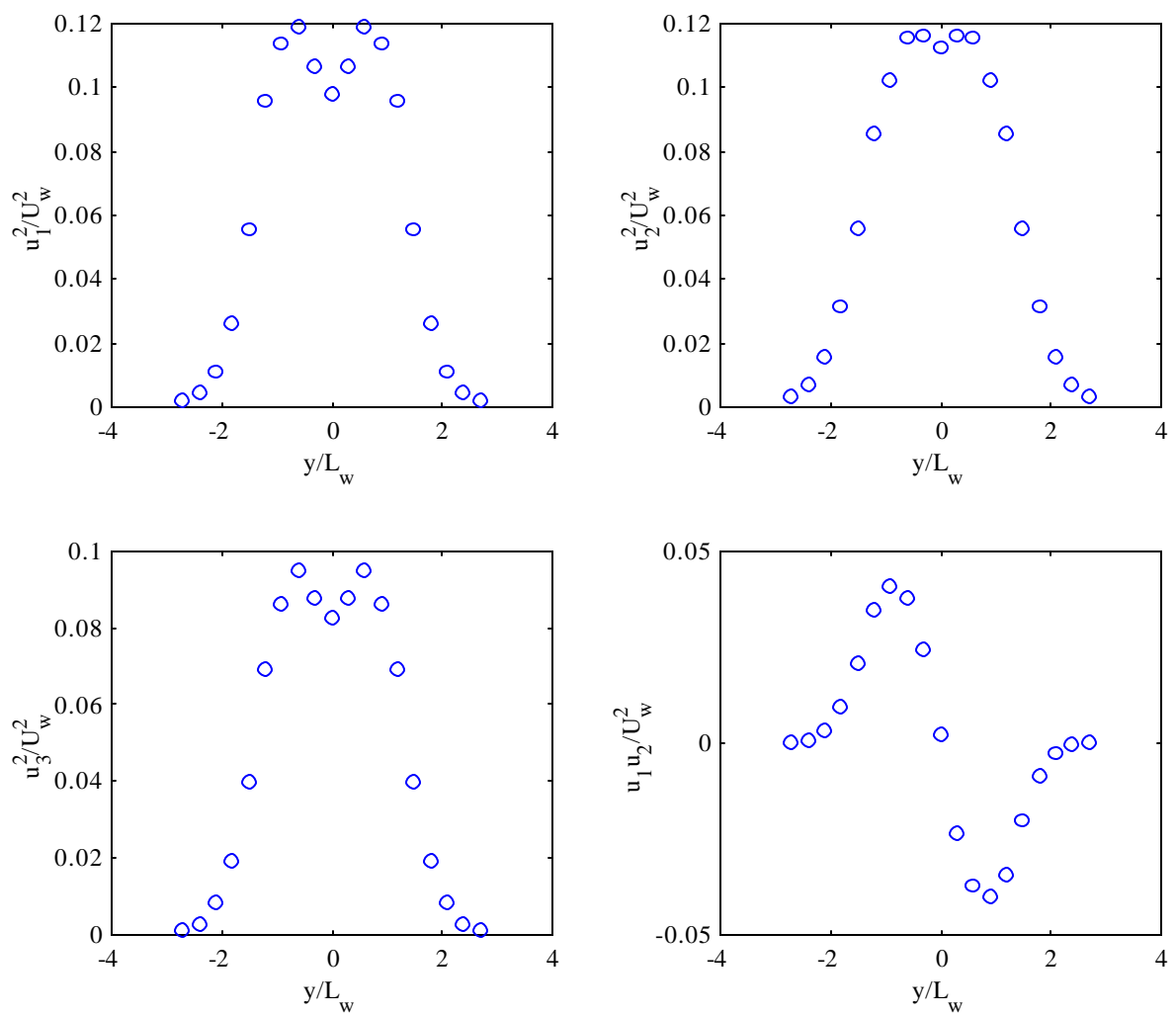


Figure 18 Output from *profile.m*

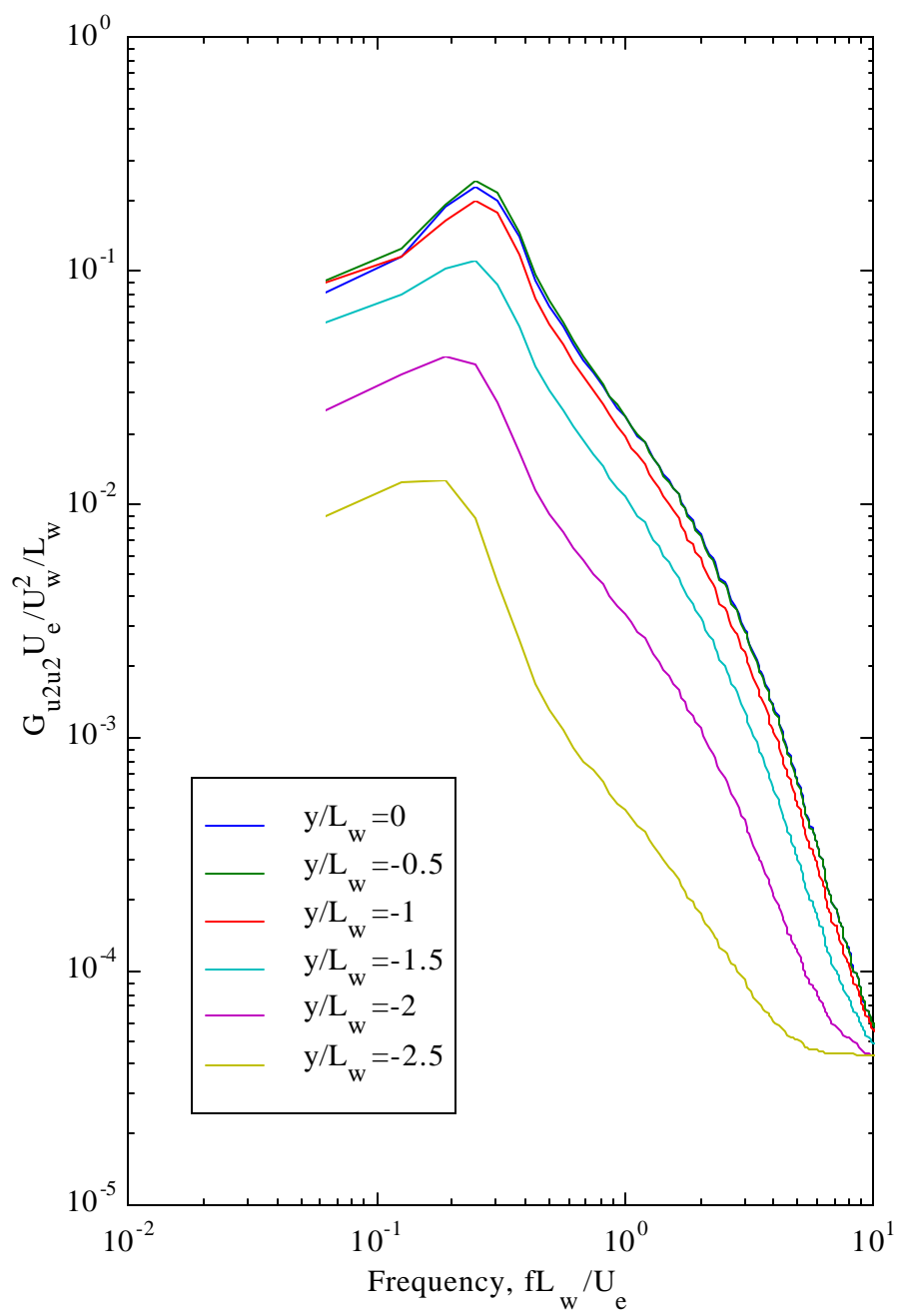


Figure 19. Output from *upsepc.m*

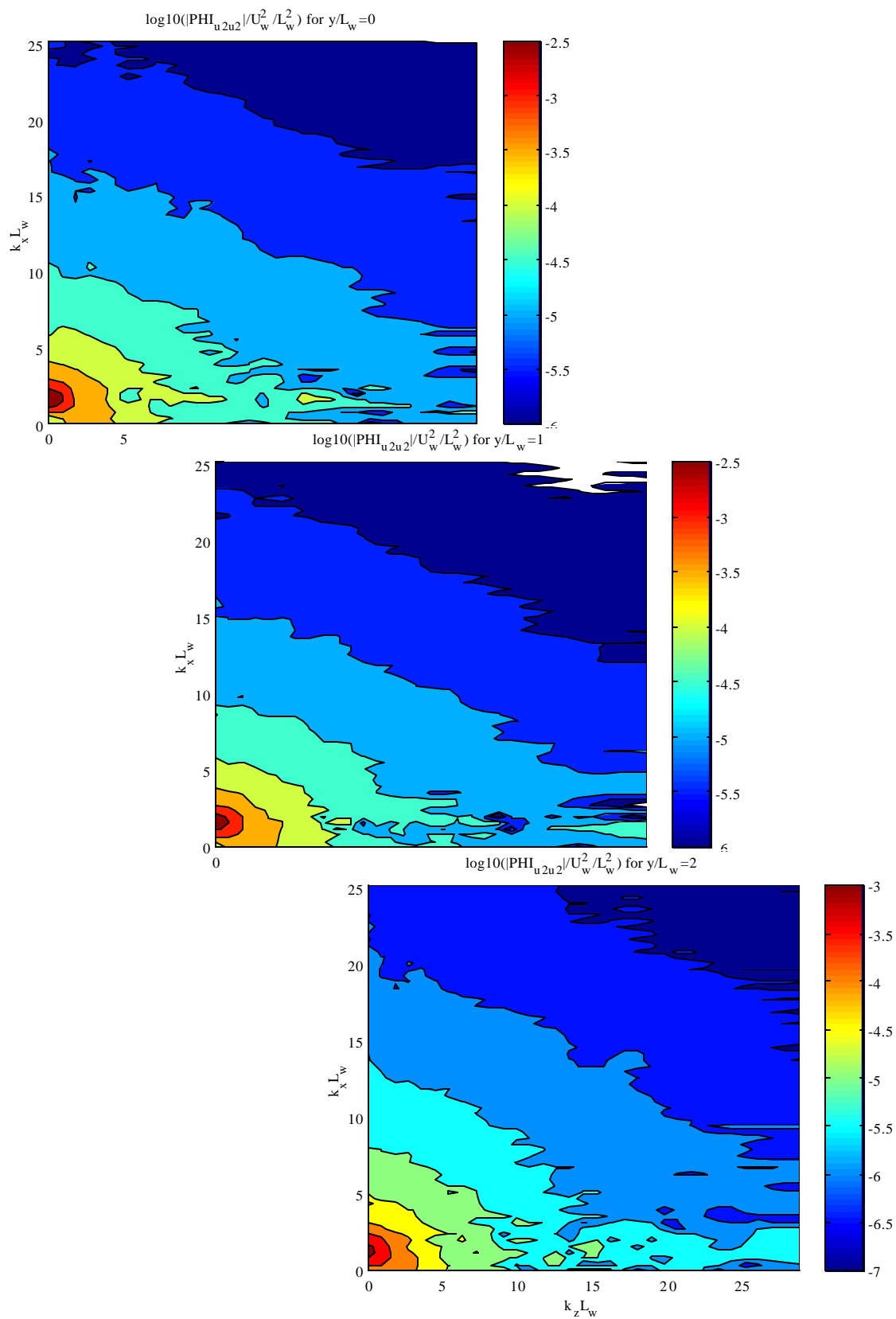


Figure 20. Output from *kwsepc.m*

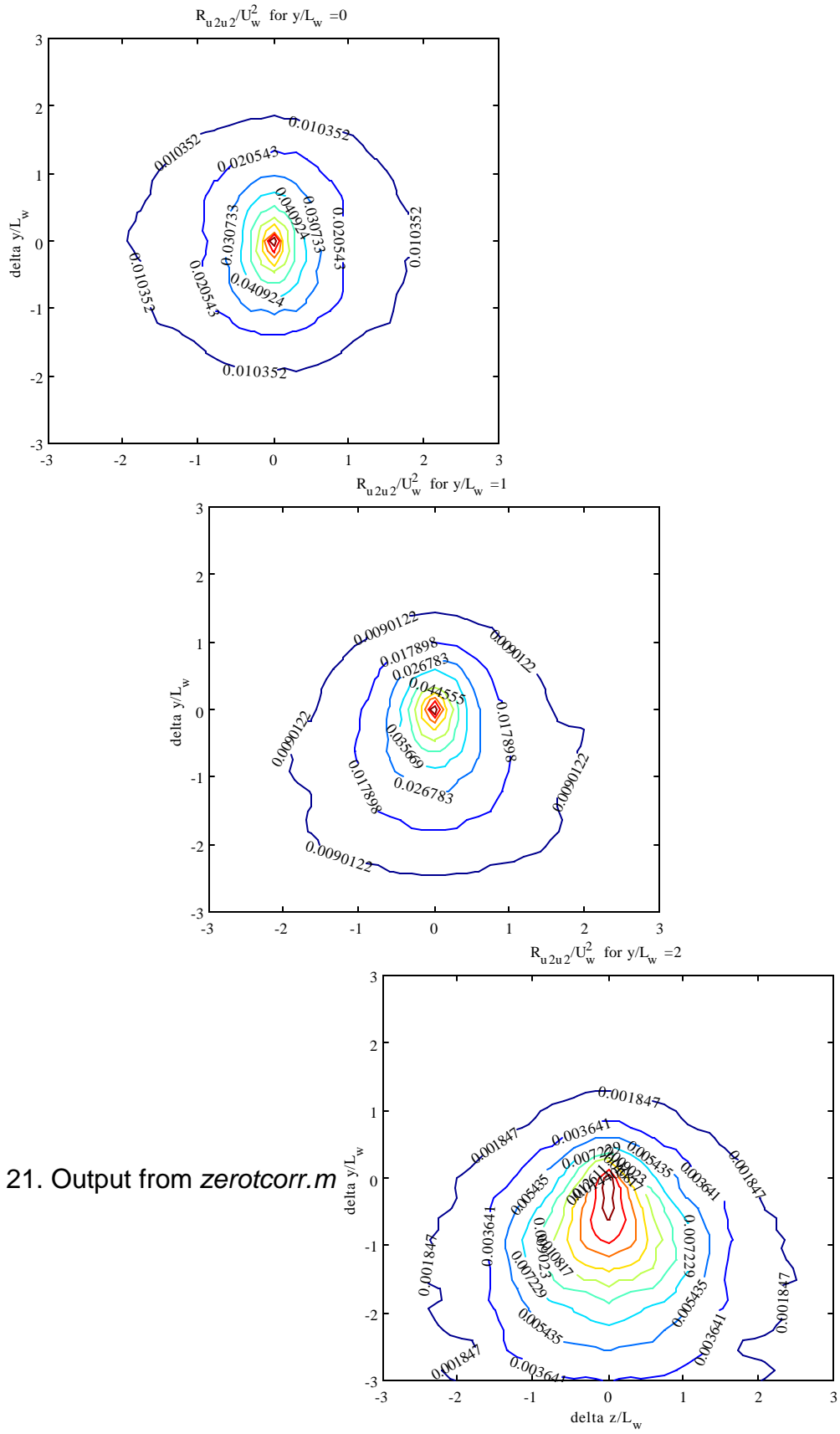


Figure 21. Output from `zerotcorr.m`

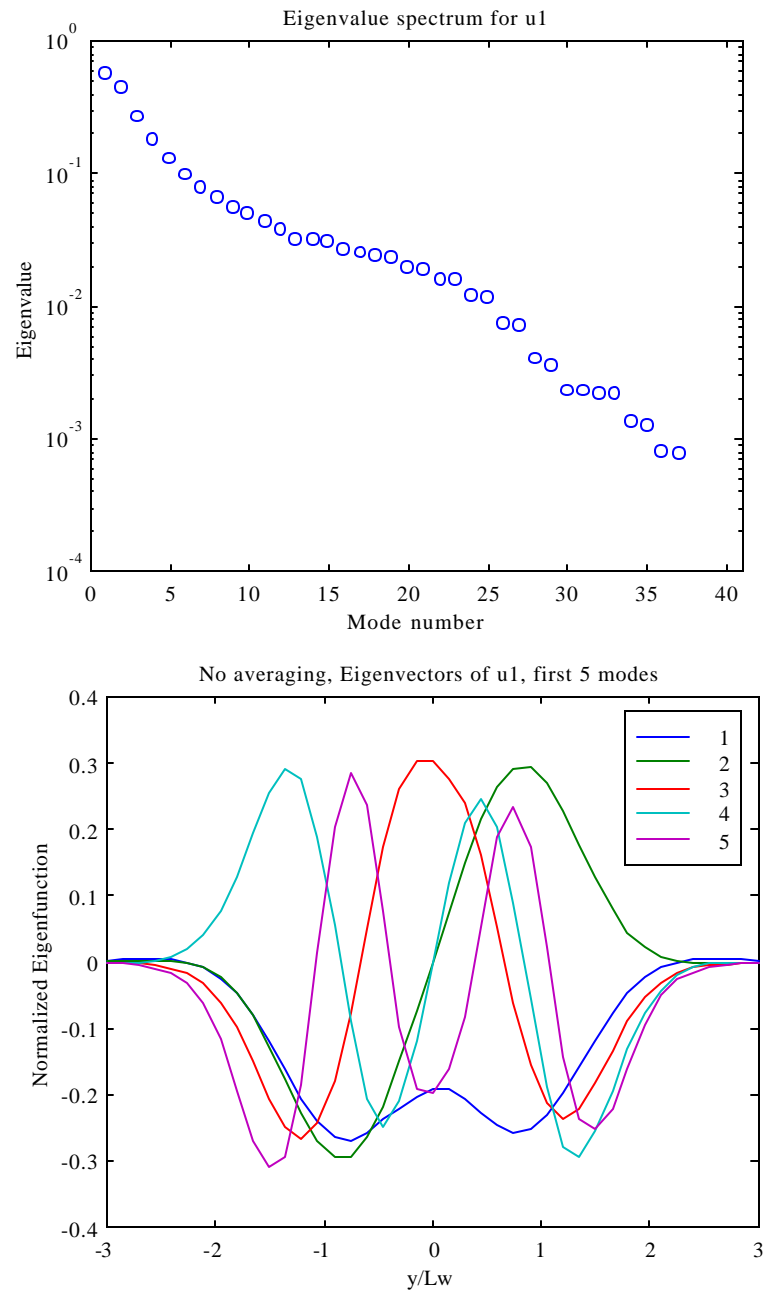


Figure 22. Output from *spod1d.m*. (a) $l = j = 1$.

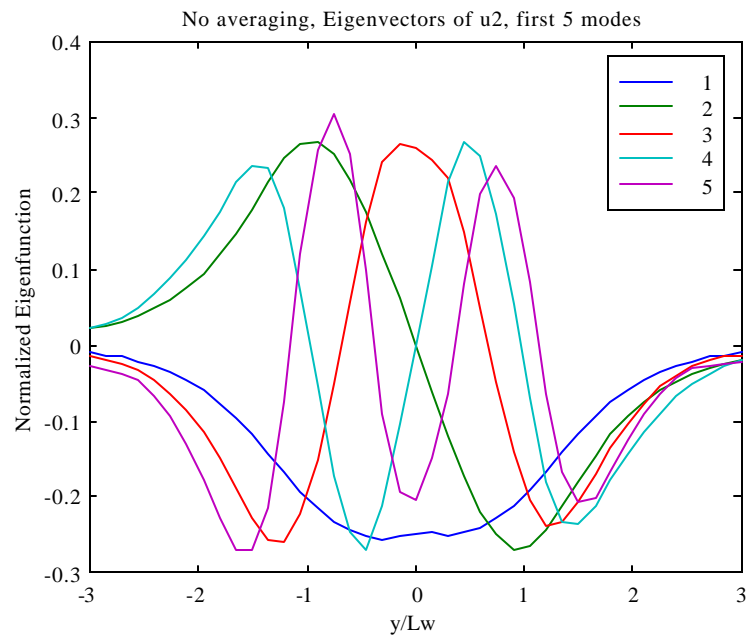
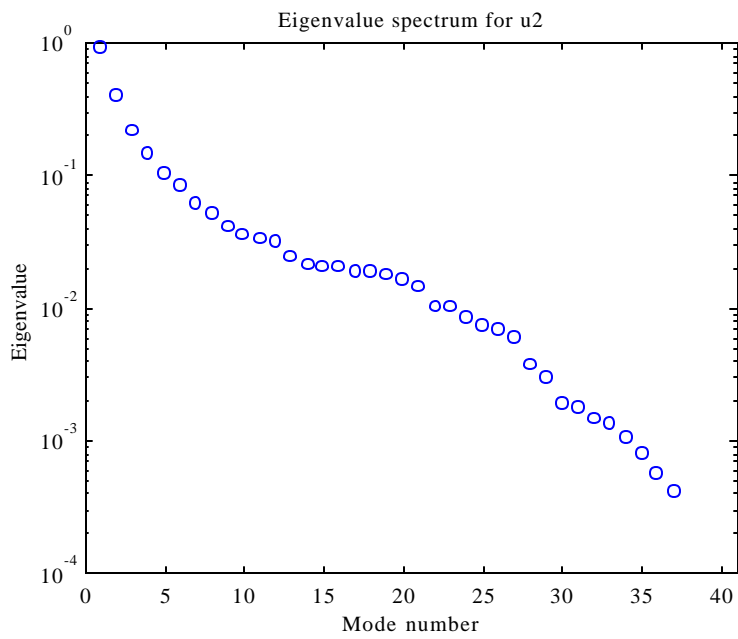


Figure 22. Output from *spod1d.m*. (b) $l = j = 2$.

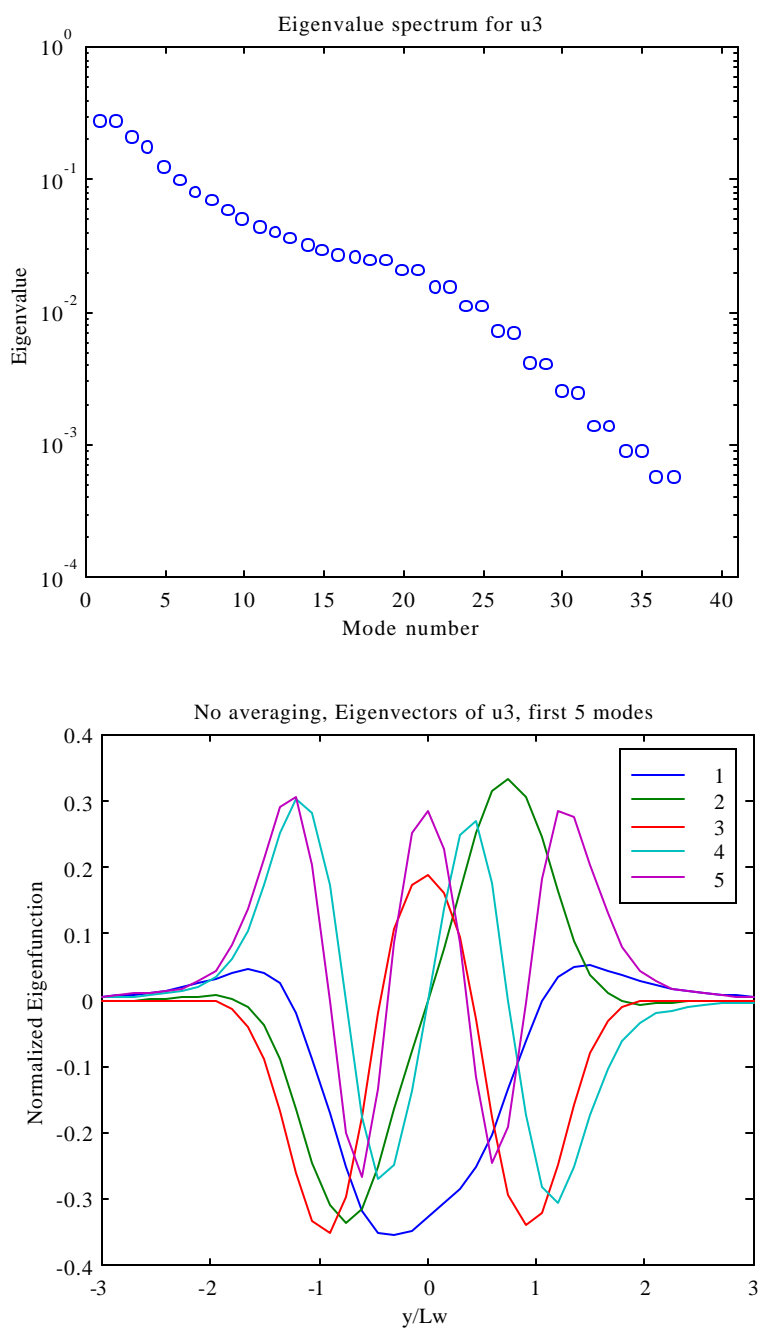


Figure 22. Output from *spod1d.m*. (c) $l = j = 3$.

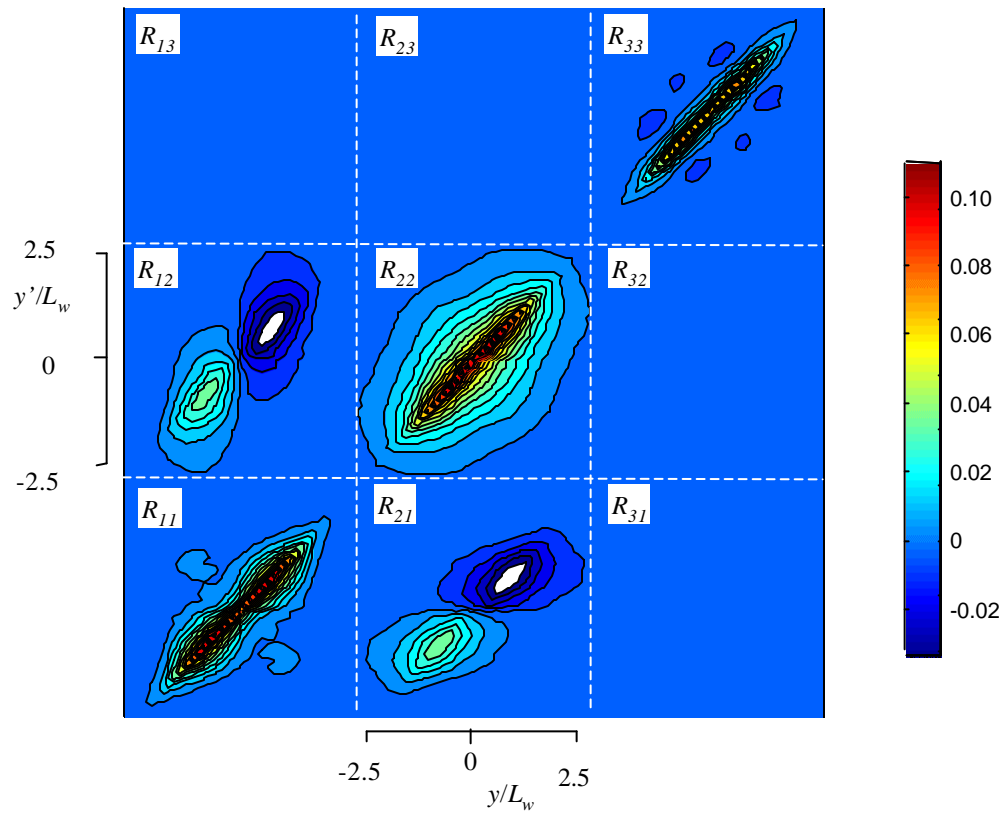


Figure 23. Correlation maps for zero time delay and spanwise separation $R_{ij}(y, y', 0, 0) / U_w^2$

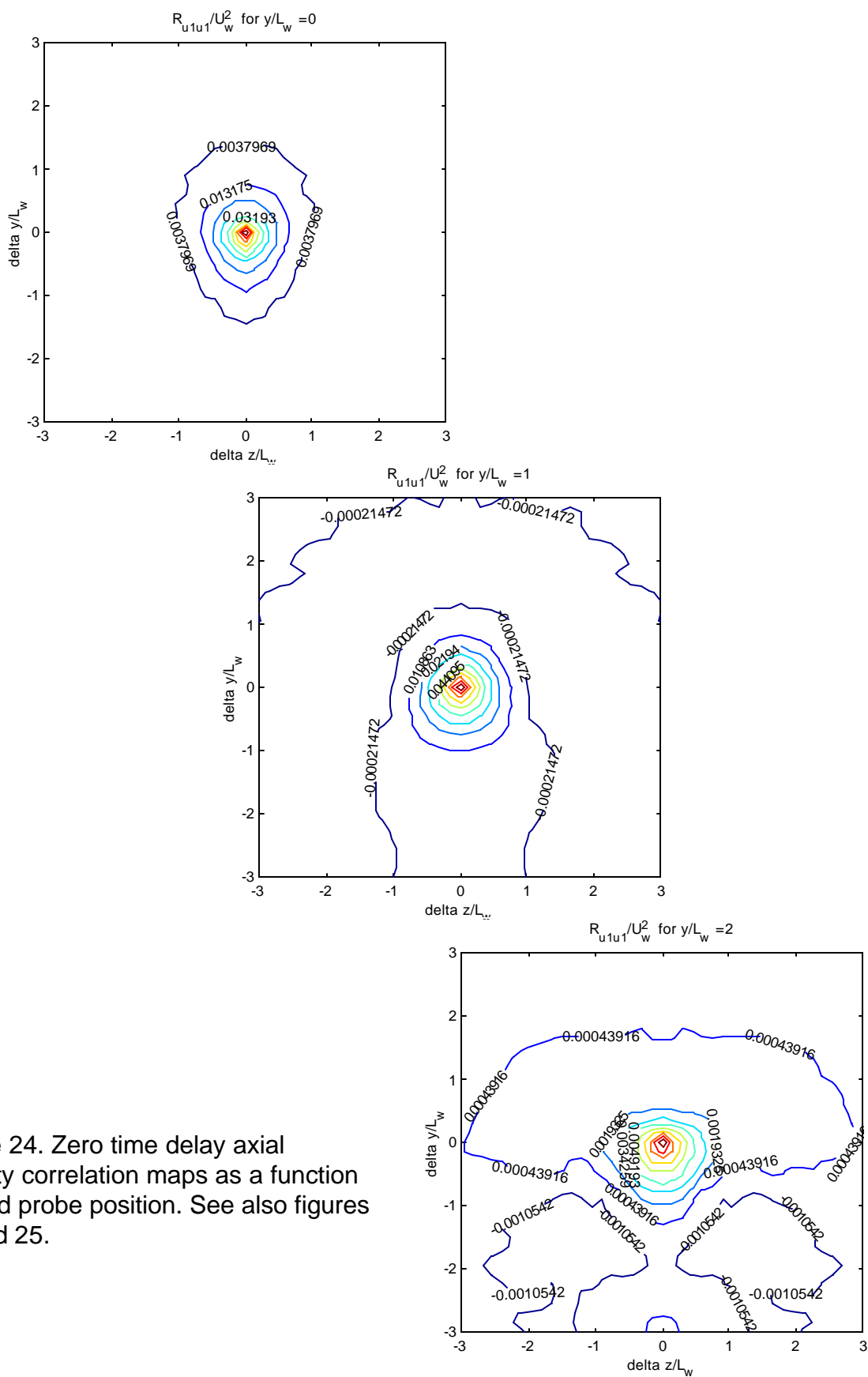


Figure 24. Zero time delay axial velocity correlation maps as a function of fixed probe position. See also figures 21 and 25.

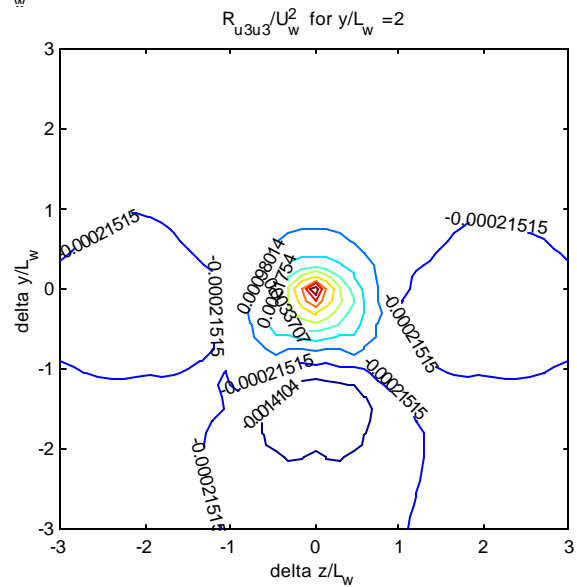
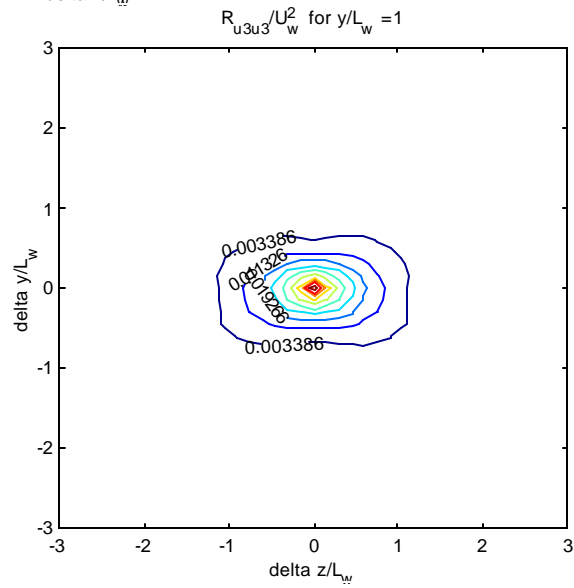
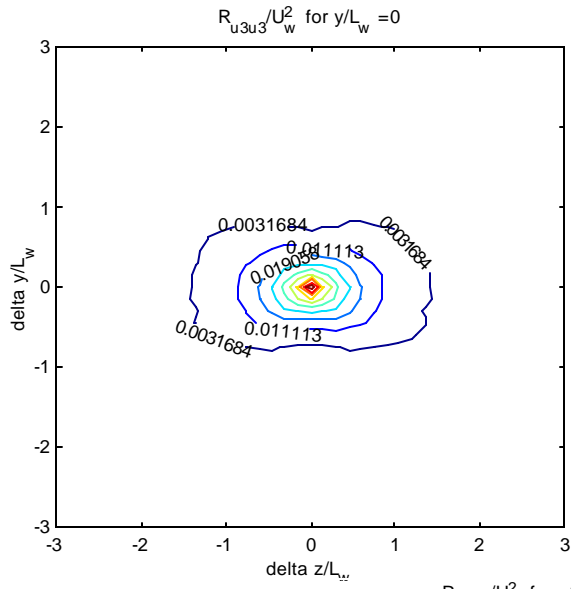


Figure 25. Zero time delay spanwise velocity correlation maps as a function of fixed probe position. See also figures 21 and 24.

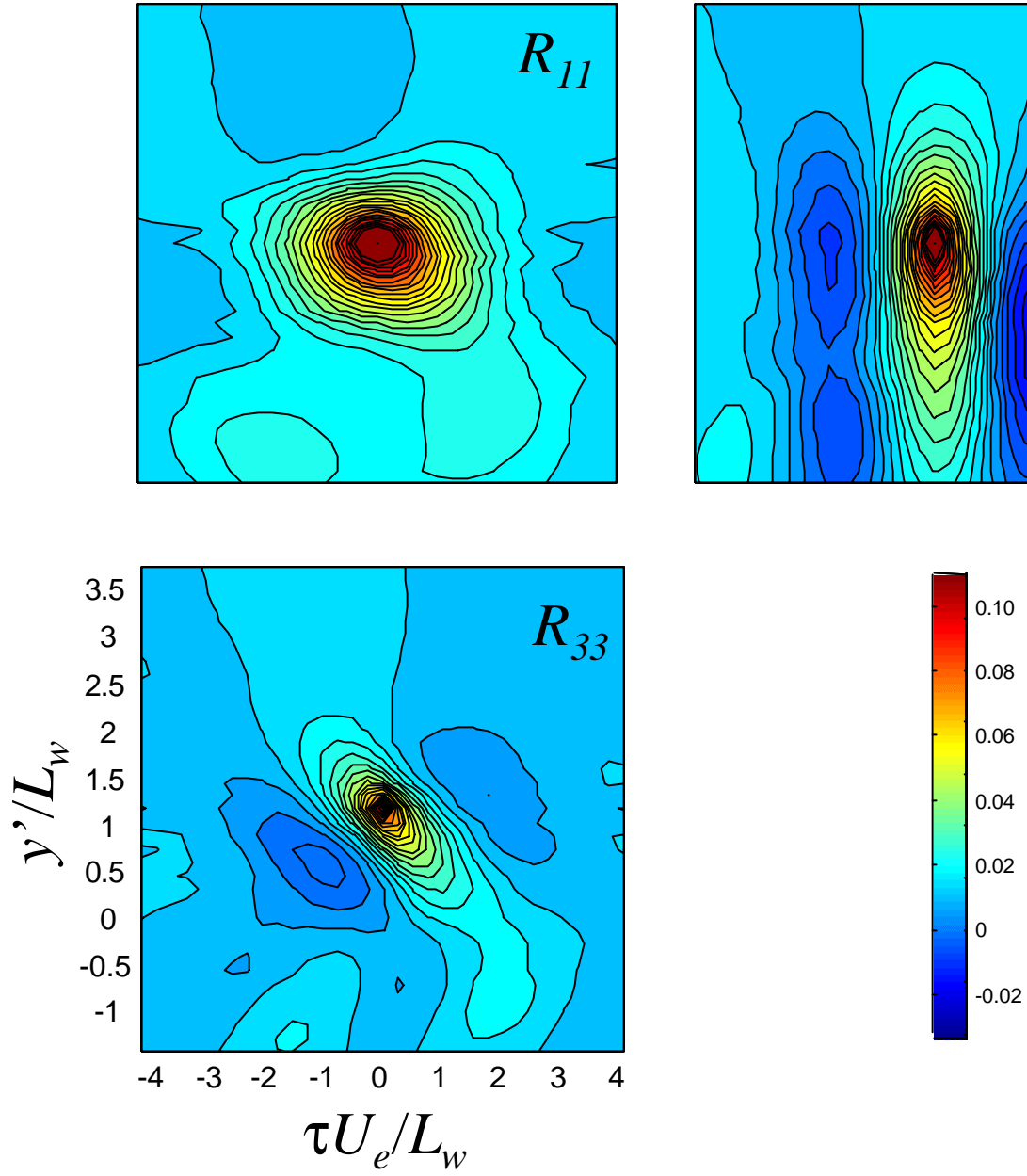


Figure 26. Correlation maps for zero spanwise separation about a fixed probe position of $y/L_w=1.16$: $R_{ij}(1.16L_w, y', 0, \tau) / U_w^2$

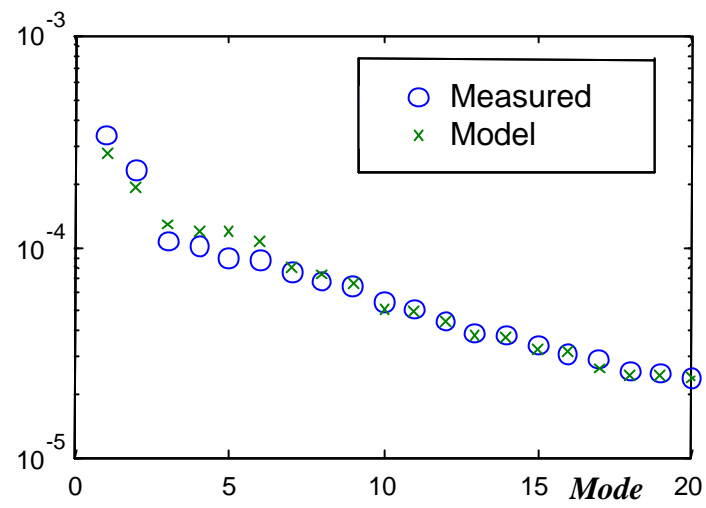


Figure 27. Eigenvalue spectra from the one-dimensional proper orthogonal decomposition in the y direction.

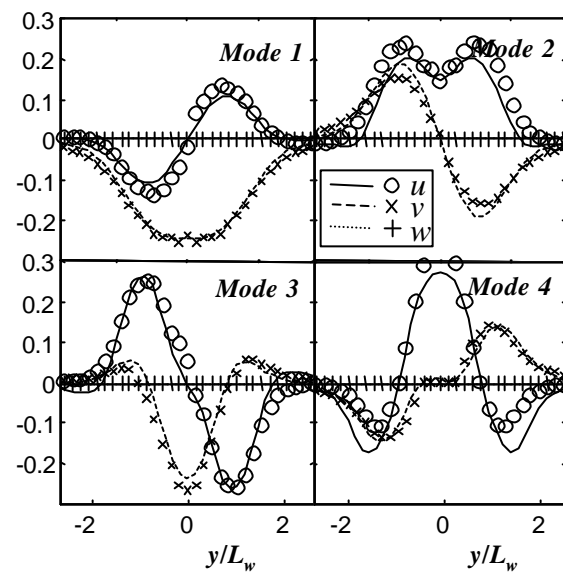


Figure 28. Modal profiles for the first 4 modes. Symbols show measurements, lines show model results. Modes 3 and 4 are reversed for the model results.

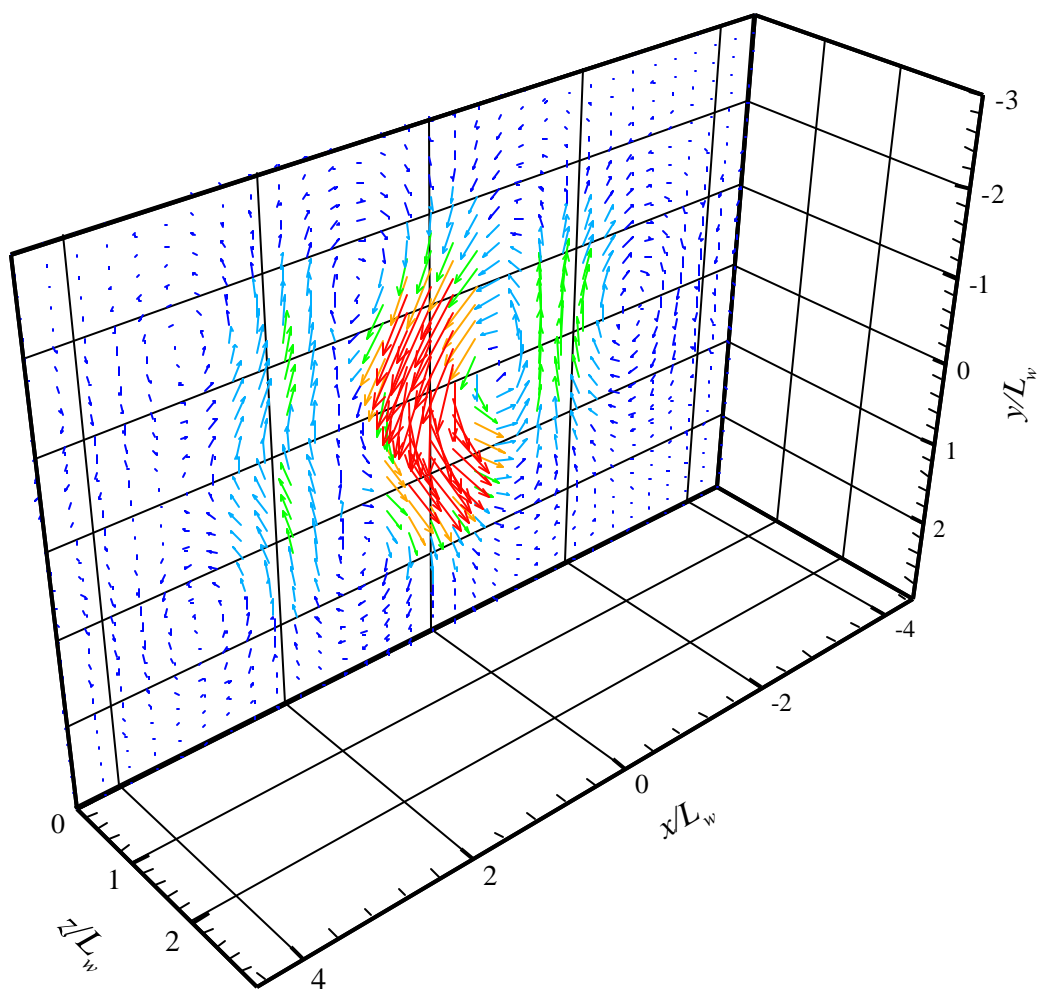


Figure 29(a). Characteristic eddy associated with the first proper orthogonal mode.

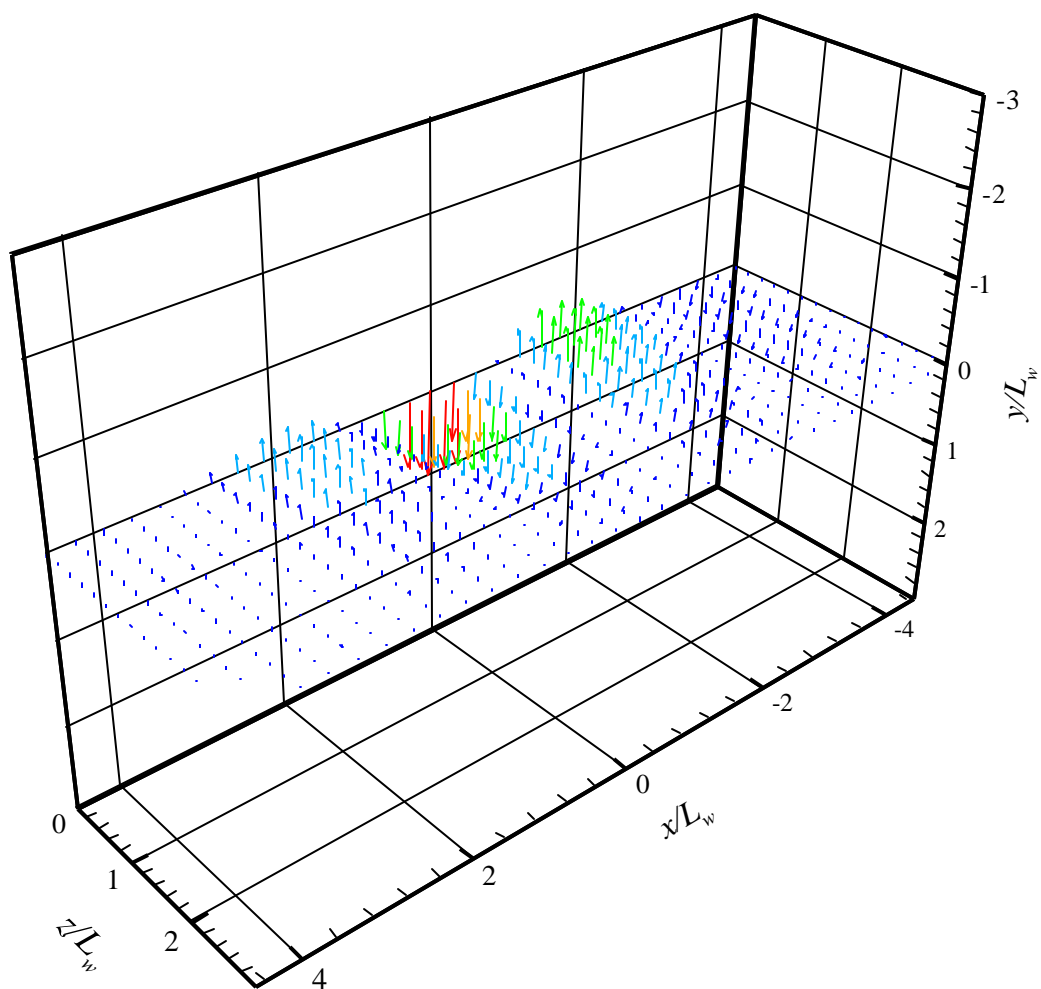


Figure 29(b). Characteristic eddy associated with the first proper orthogonal mode.

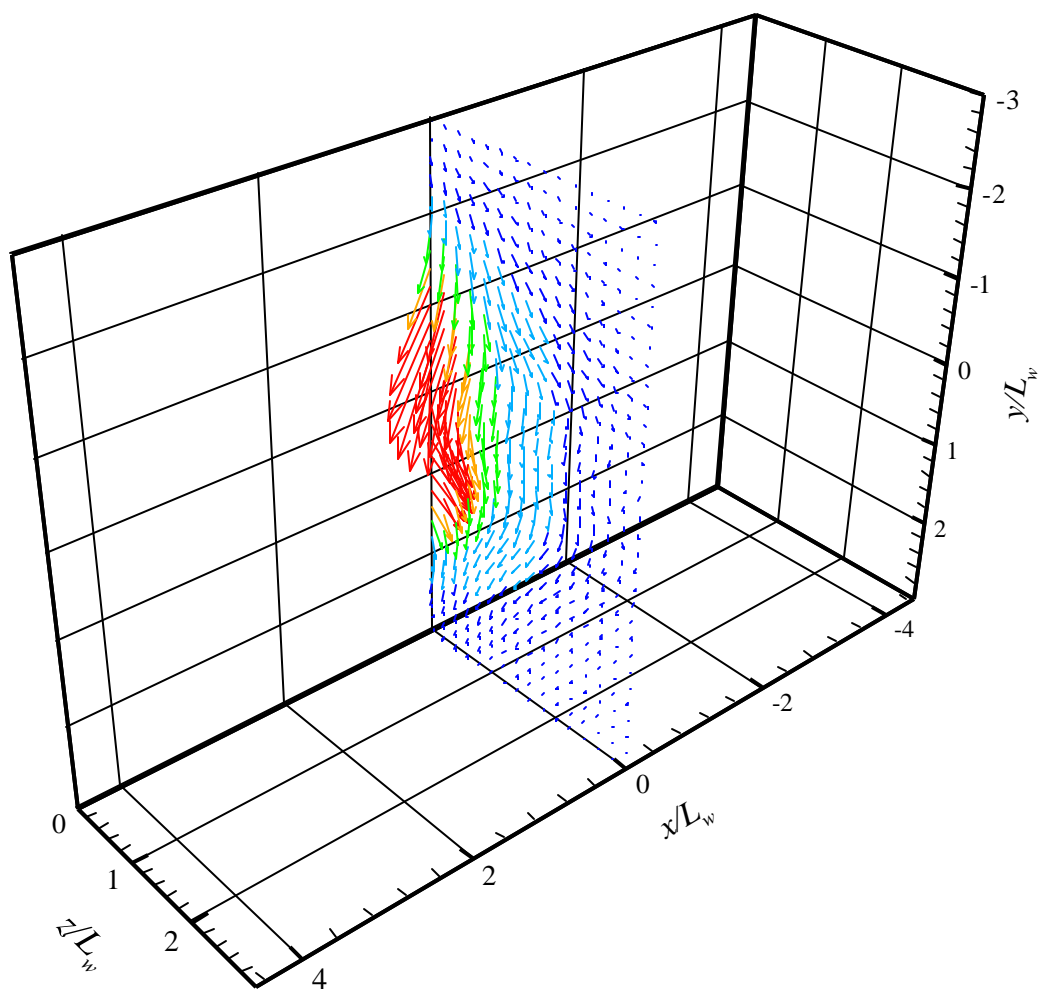


Figure 29(c). Characteristic eddy associated with the first proper orthogonal mode.

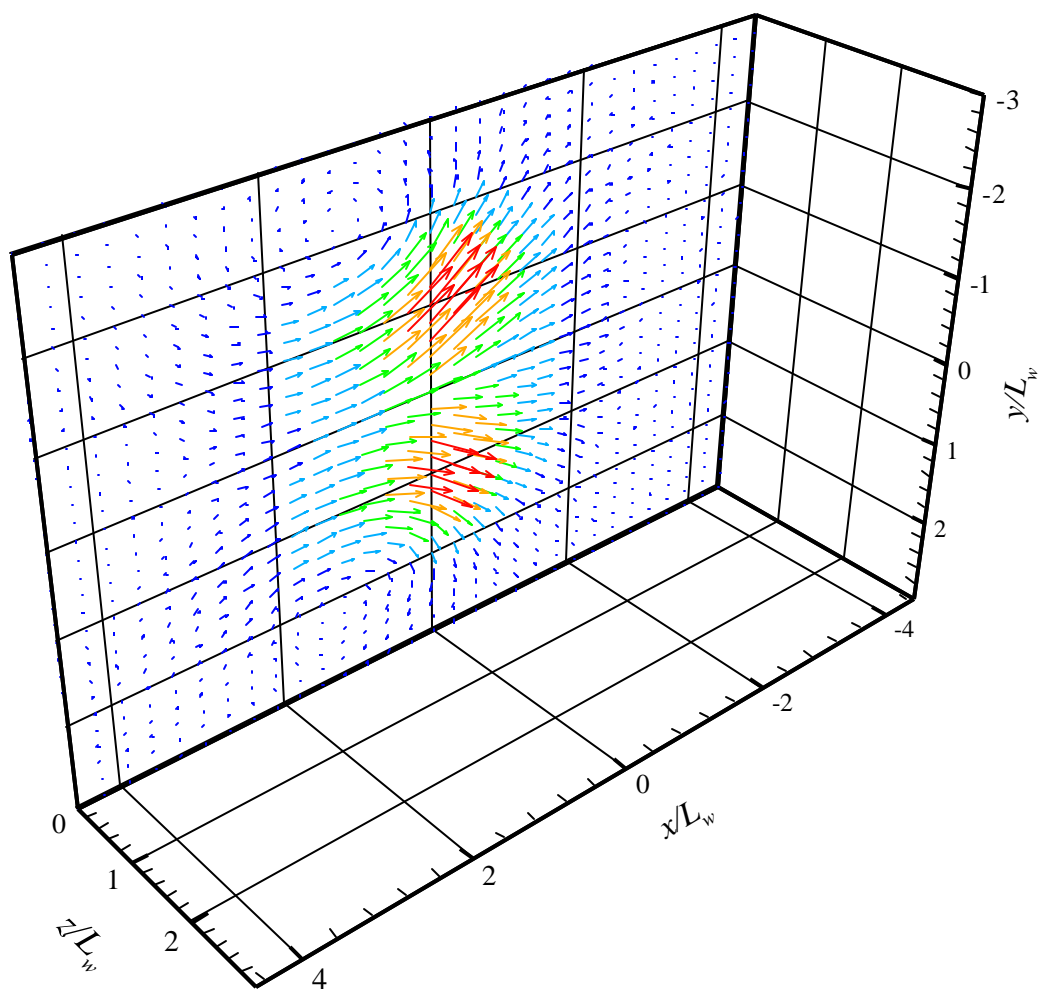


Figure 30(a). Characteristic eddy associated with the second proper orthogonal mode.

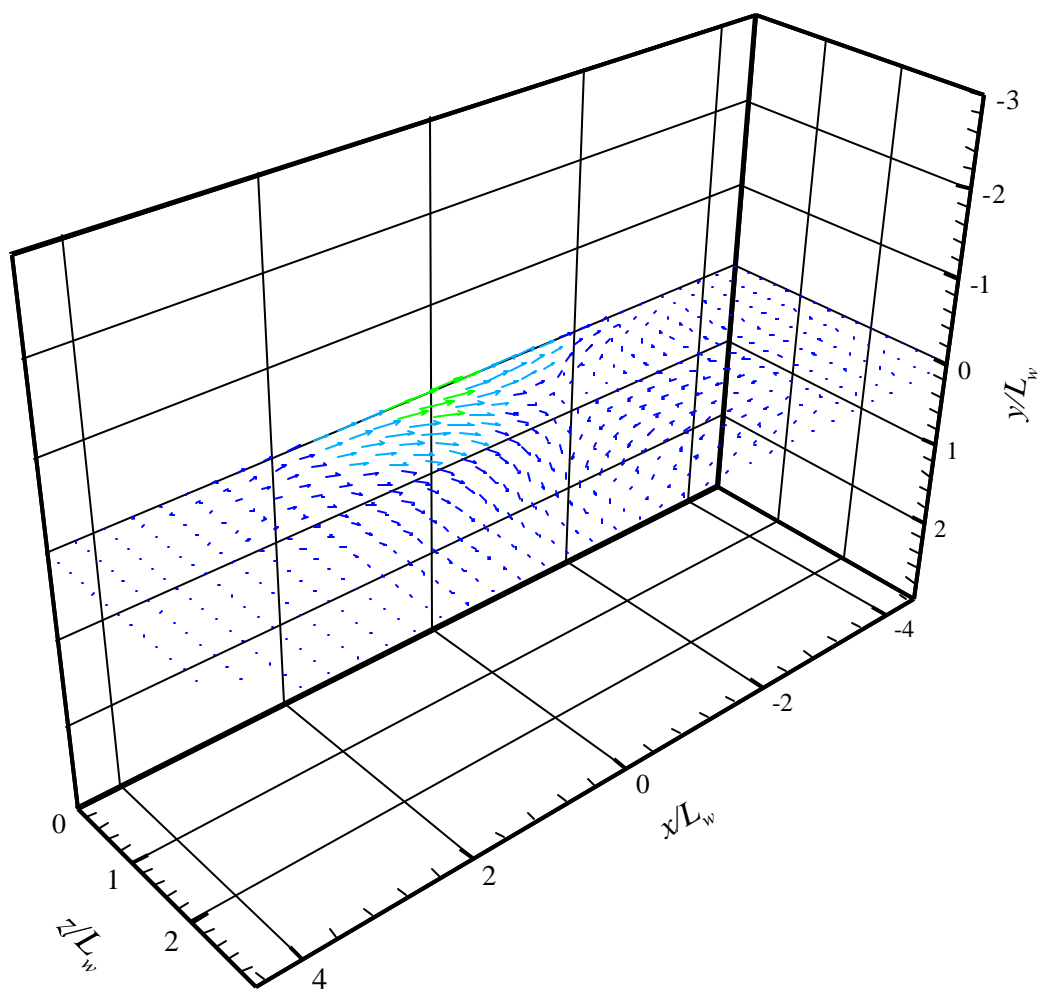


Figure 30(b). Characteristic eddy associated with the second proper orthogonal mode.

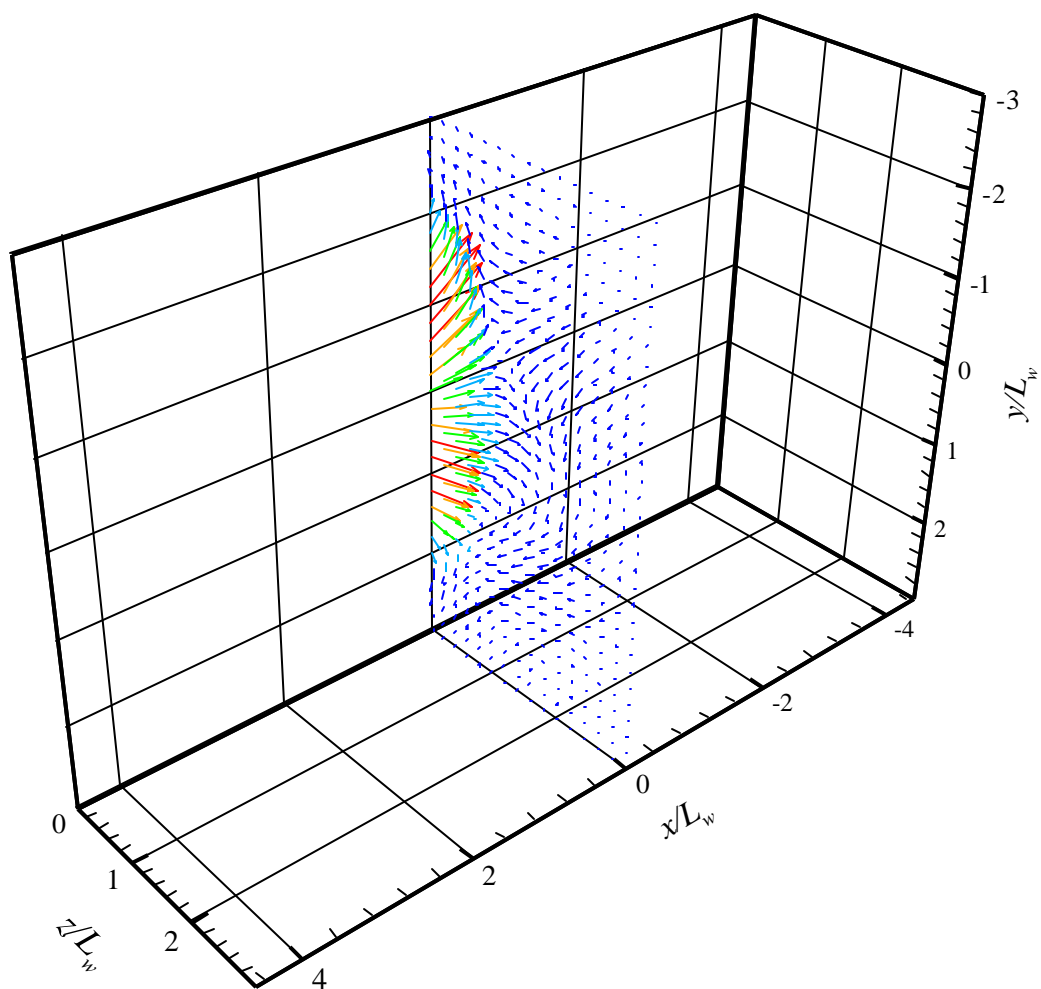


Figure 30(c). Characteristic eddy associated with the second proper orthogonal mode.

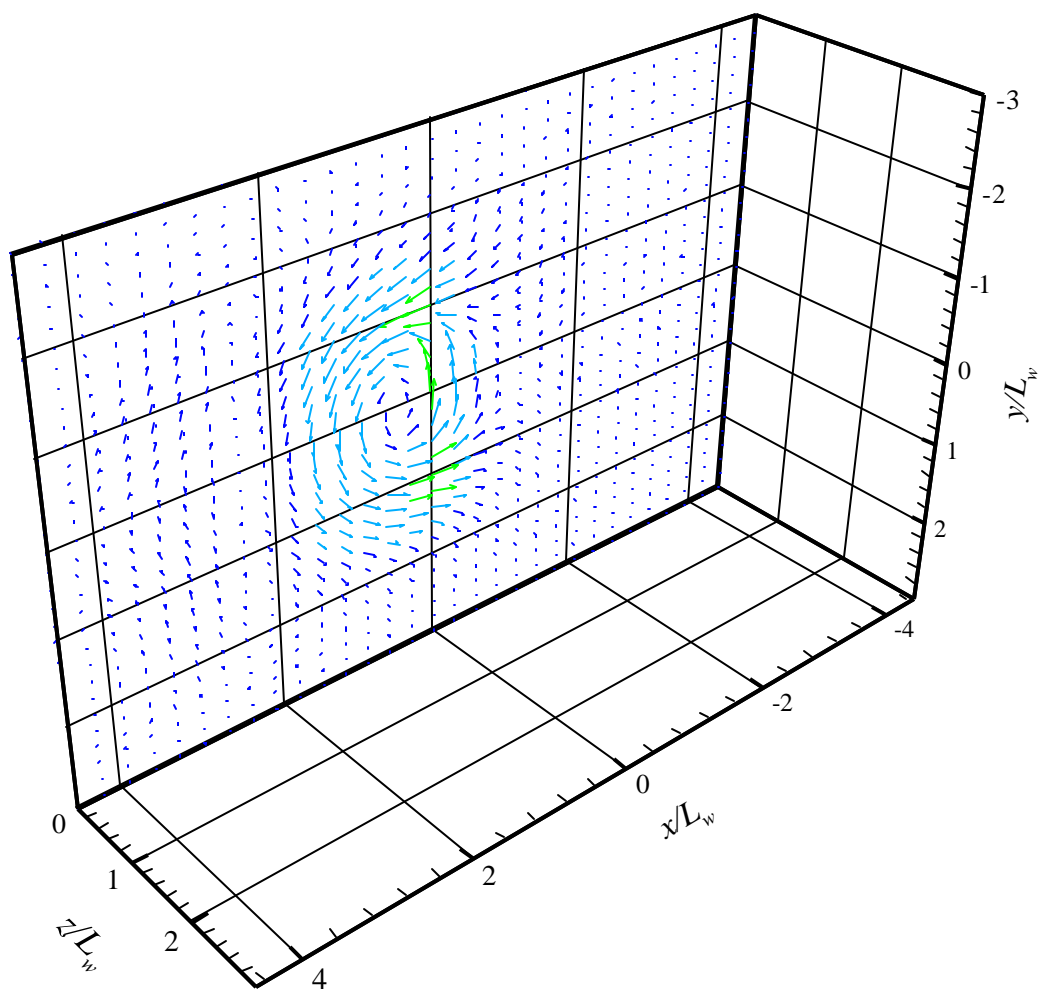


Figure 31(a). Characteristic eddy associated with the third proper orthogonal mode.

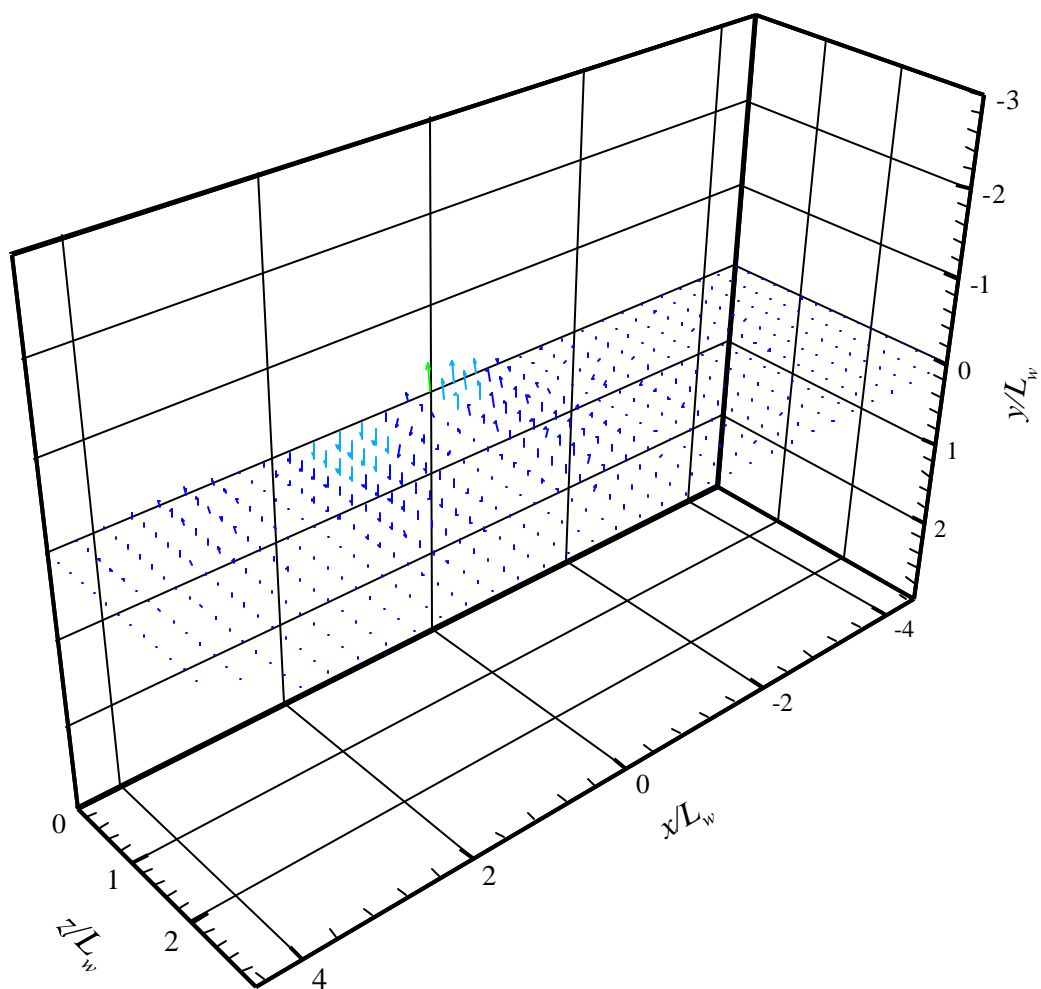


Figure 31(b). Characteristic eddy associated with the third proper orthogonal mode.

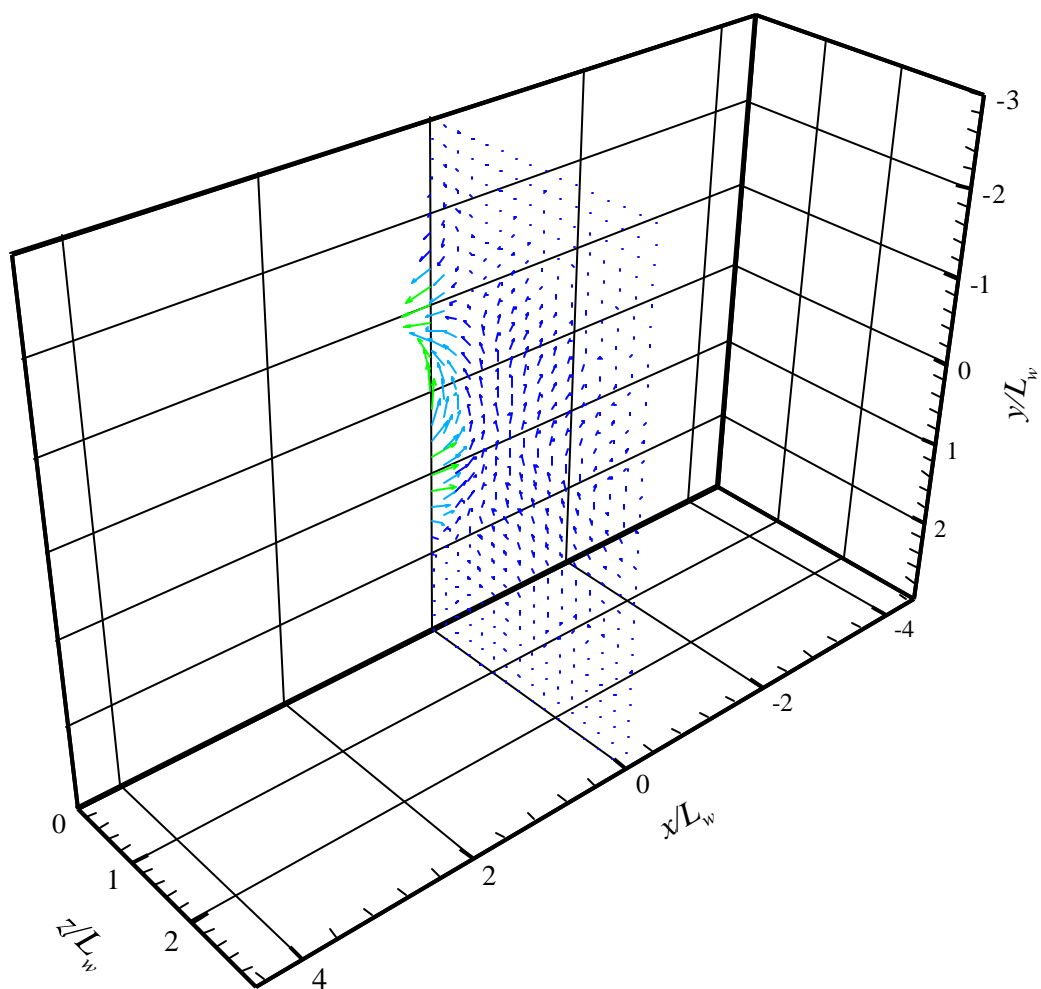


Figure 31(c). Characteristic eddy associated with the third proper orthogonal mode.

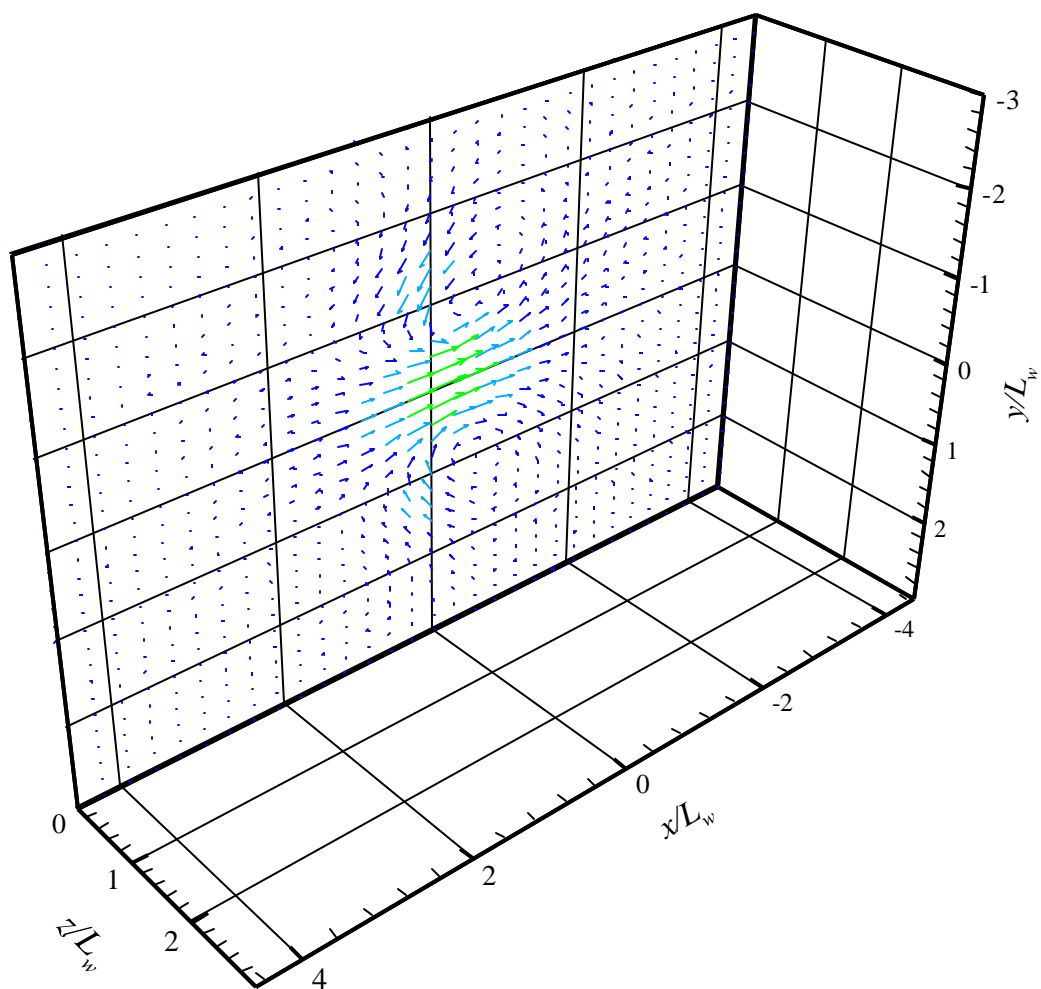


Figure 32(a). Characteristic eddy associated with the fourth proper orthogonal mode.

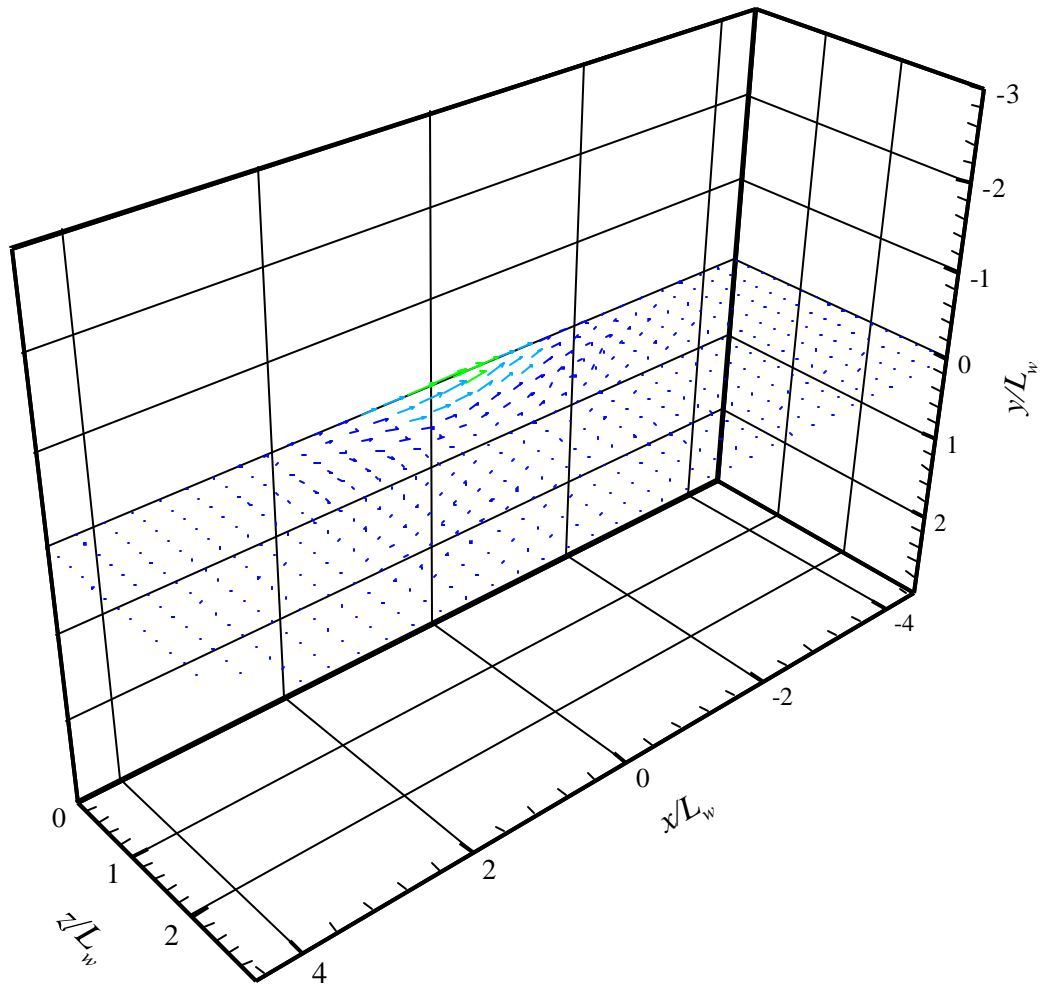


Figure 32(b). Characteristic eddy associated with the fourth proper orthogonal mode.

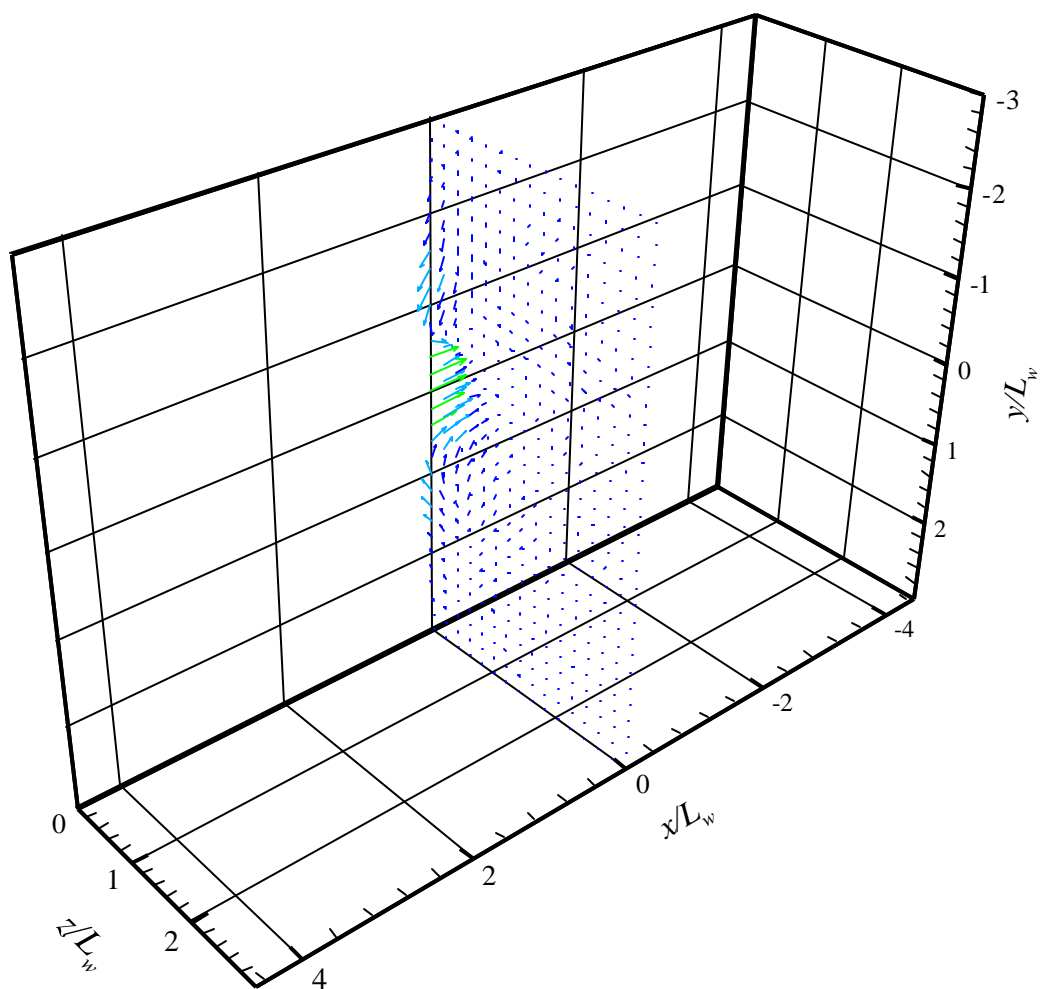


Figure 32(c). Characteristic eddy associated with the fourth proper orthogonal mode.

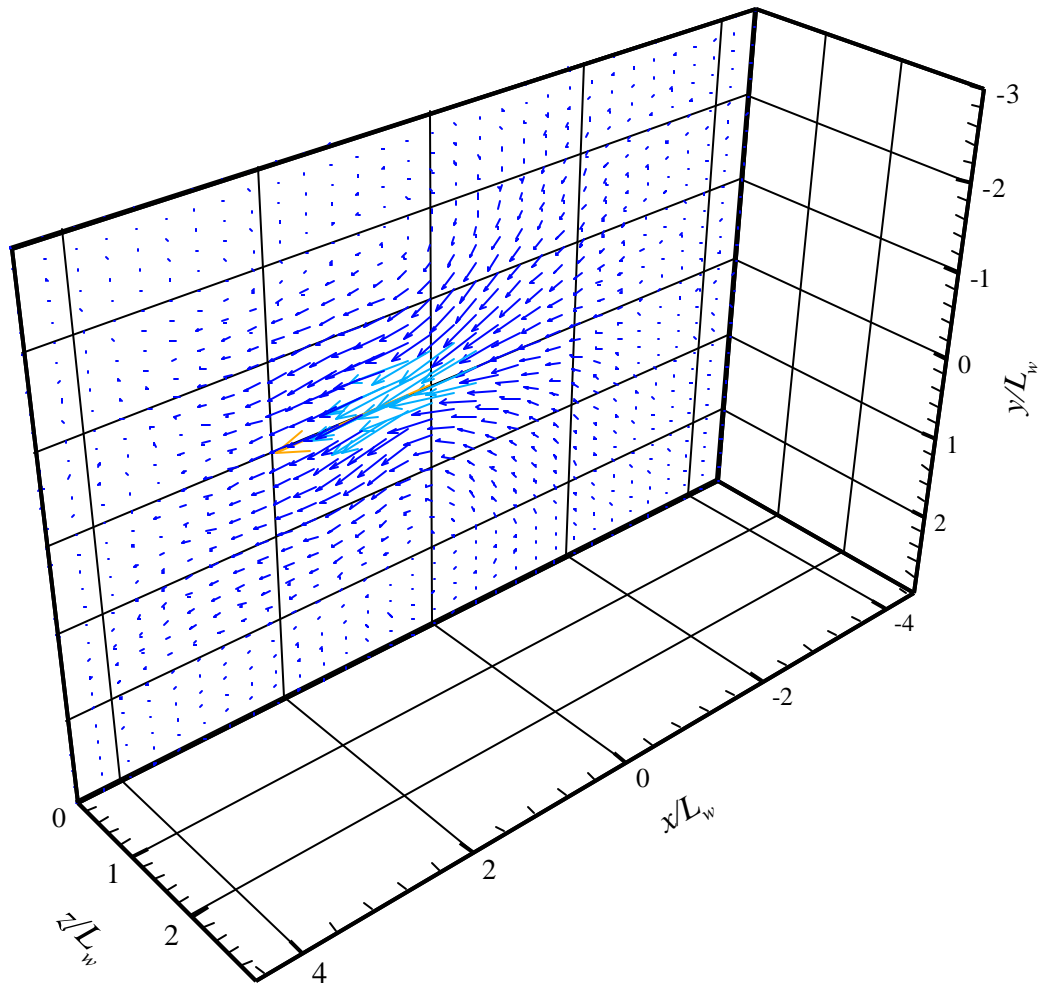


Figure 33(a). Linear stochastic estimate of the velocity field associated with a u fluctuation at $y/L_w=0$

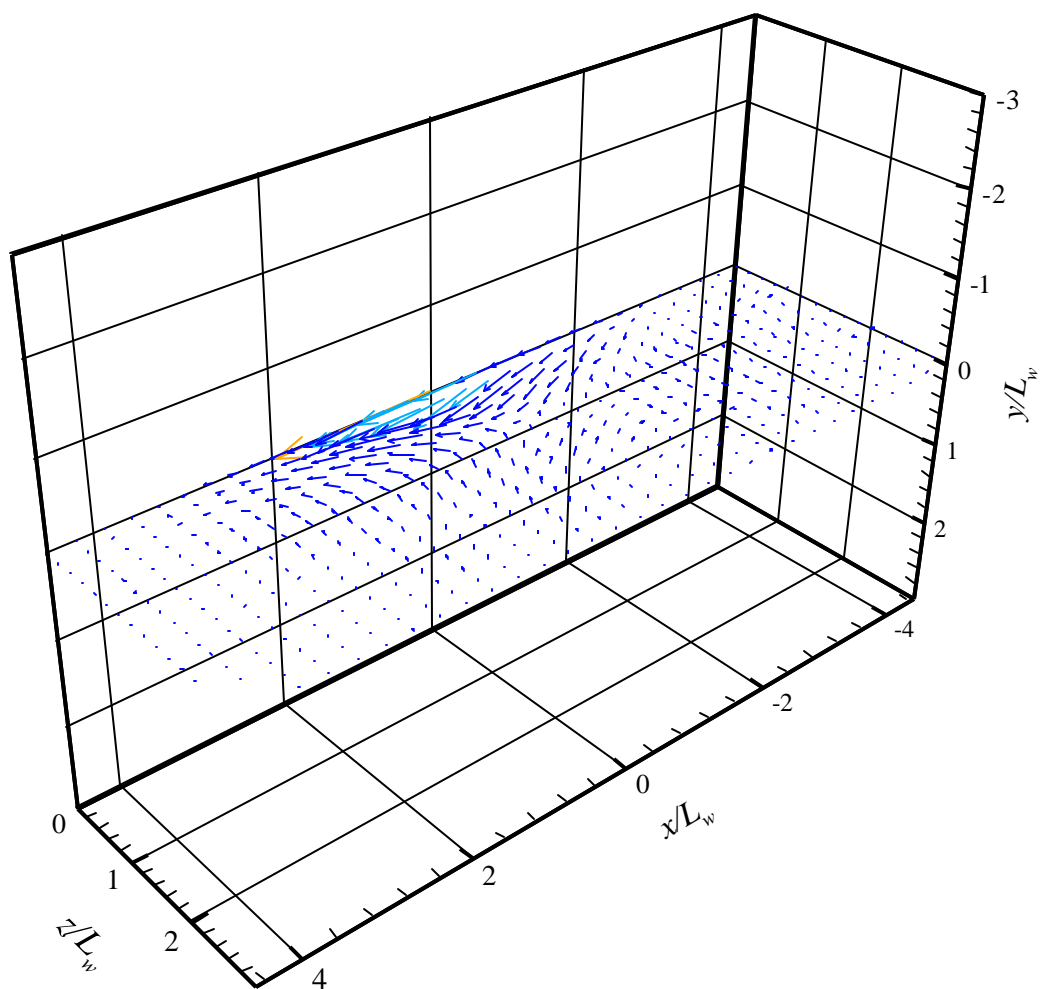


Figure 33(b). Linear stochastic estimate of the velocity field associated with a u fluctuation at $y/L_w=0$

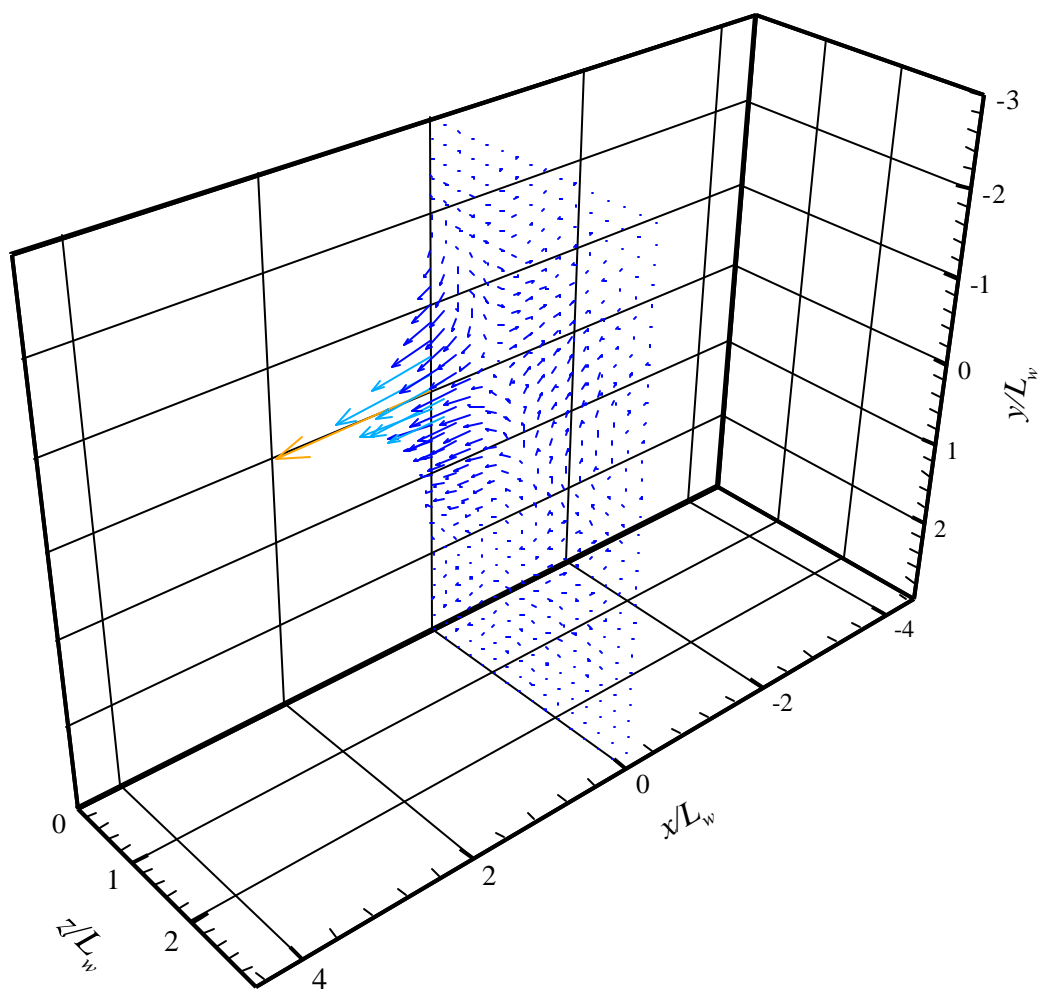


Figure 33(c). Linear stochastic estimate of the velocity field associated with a u fluctuation at $y/L_w=0$

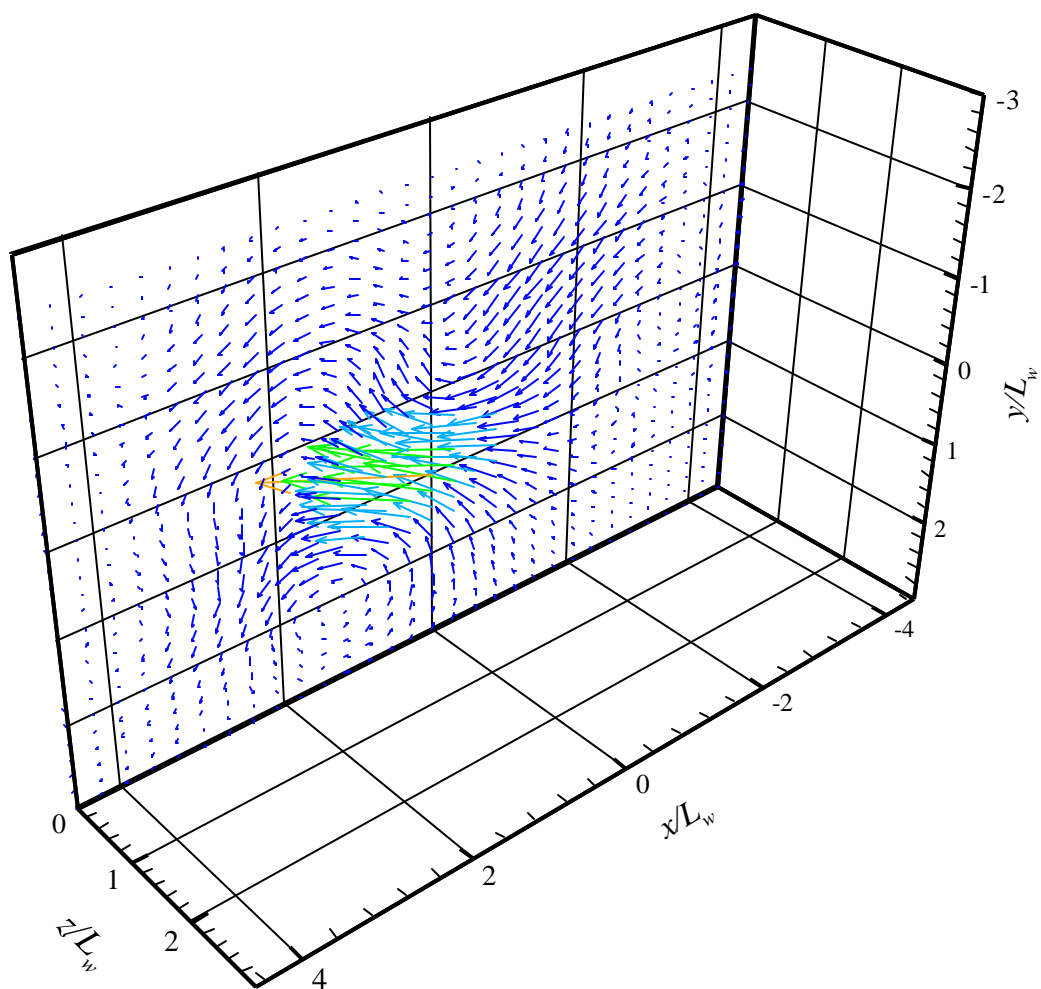


Figure 34(a). Linear stochastic estimate of the velocity field associated with a u fluctuation at $y/L_w=1$

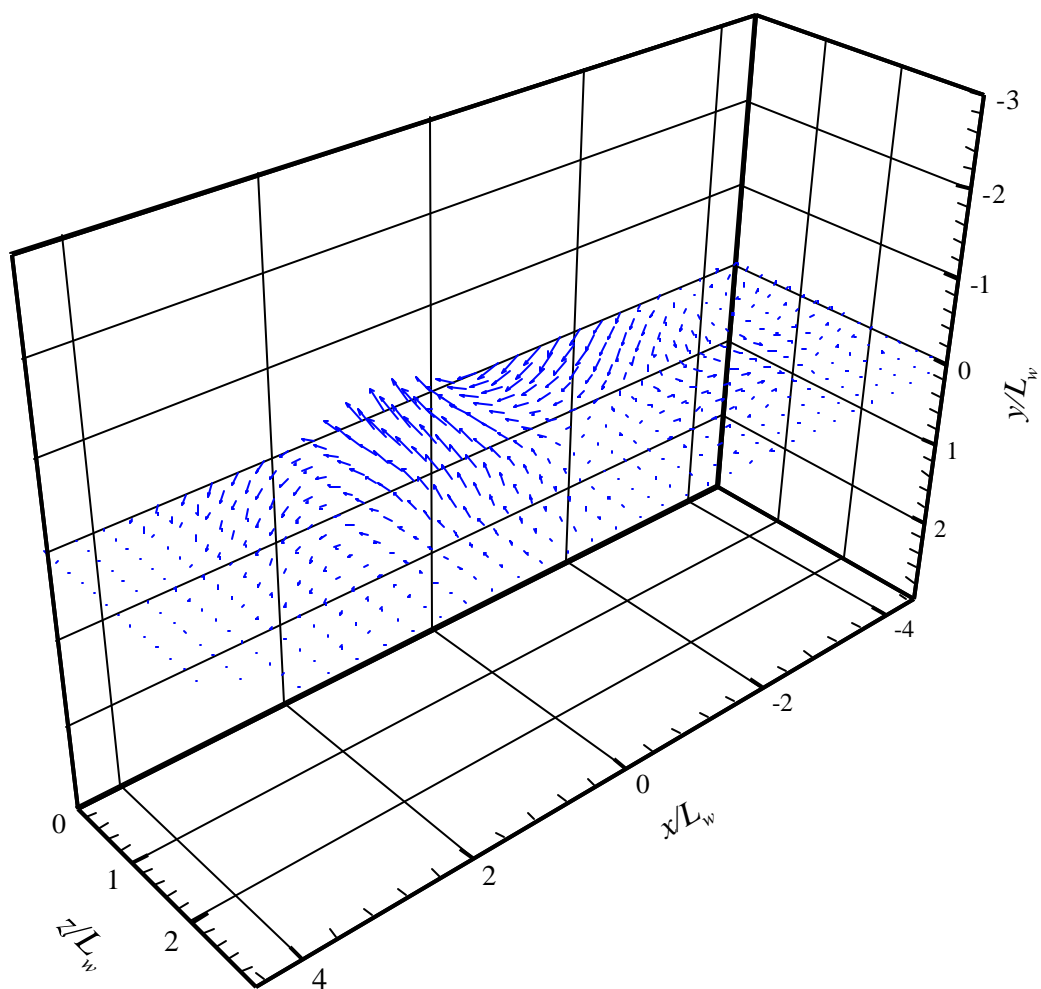


Figure 34(b). Linear stochastic estimate of the velocity field associated with a u fluctuation at $y/L_w=1$

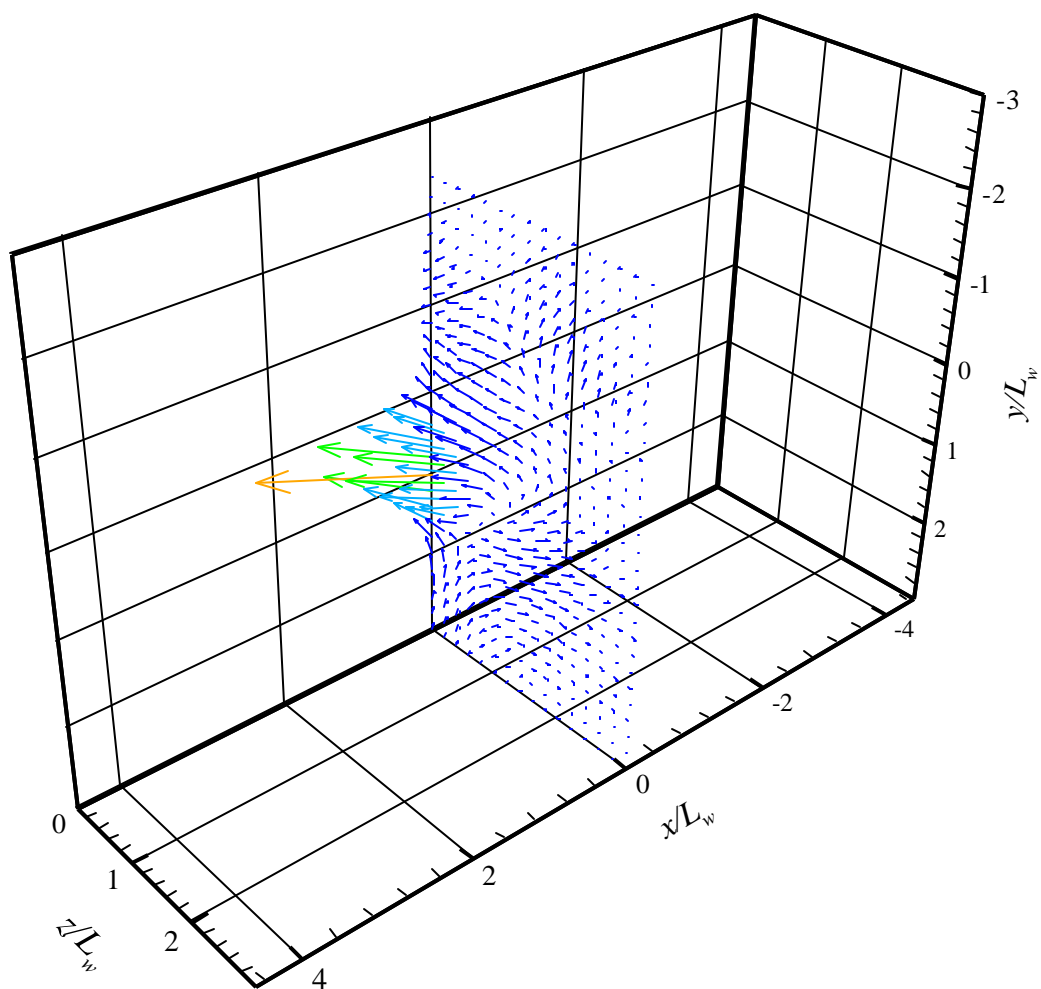


Figure 34(c). Linear stochastic estimate of the velocity field associated with a u fluctuation at $y/L_w=1$

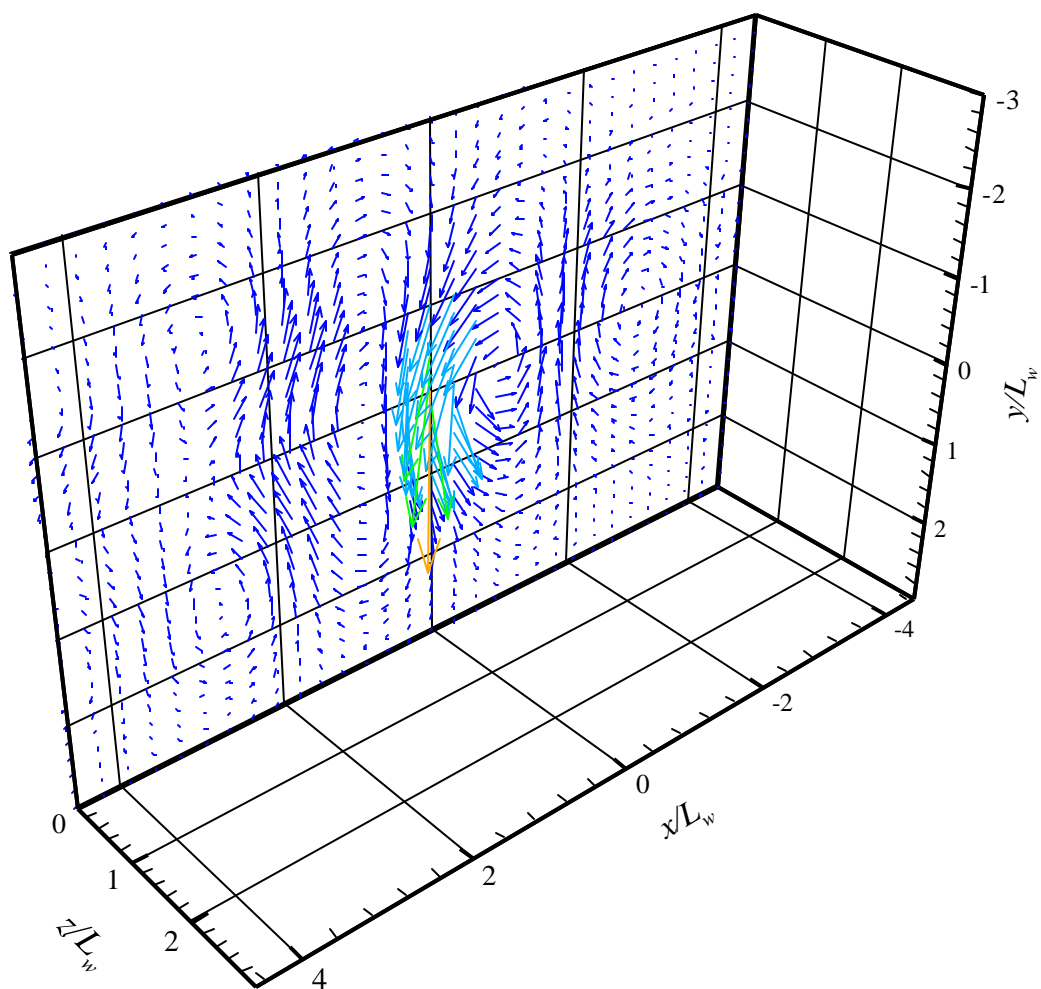


Figure 35(a). Linear stochastic estimate of the velocity field associated with a v fluctuation at $y/L_w=0$

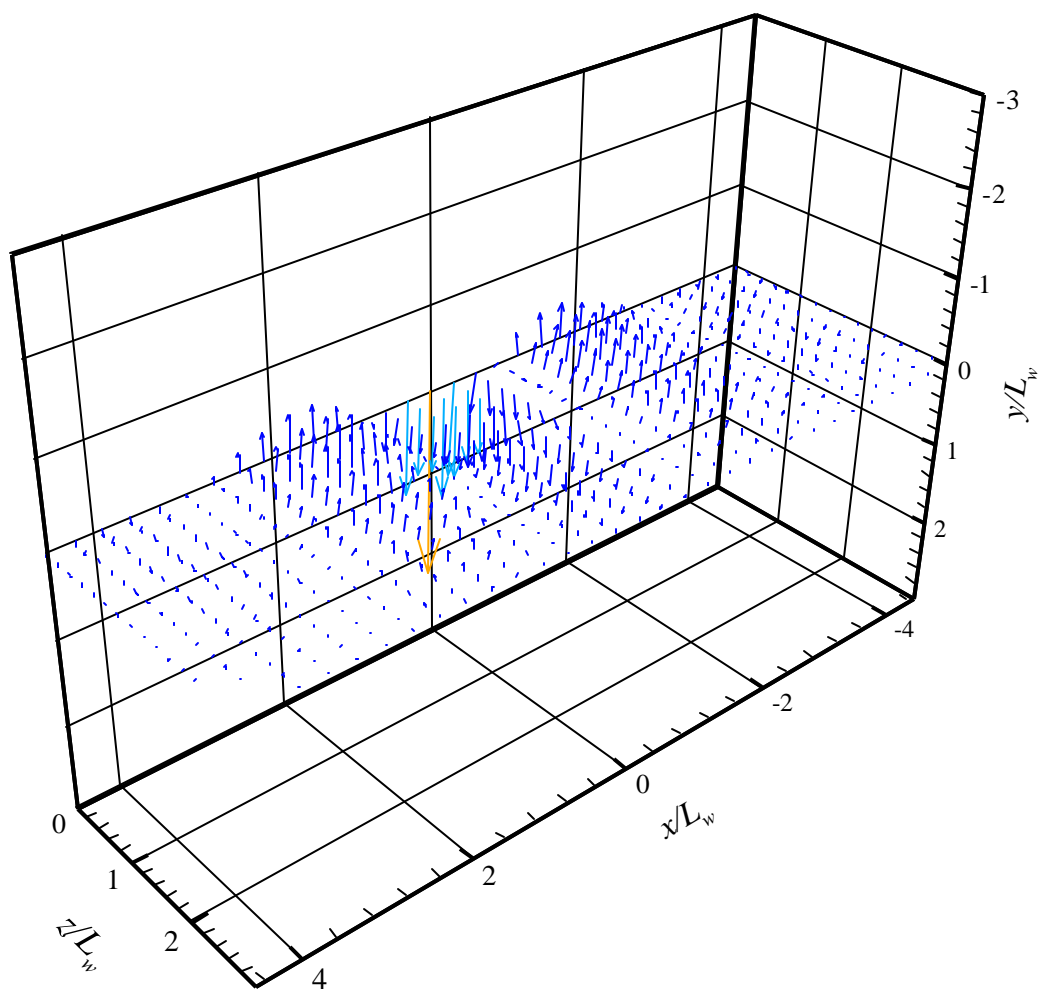


Figure 35(b). Linear stochastic estimate of the velocity field associated with a v fluctuation at $y/L_w=0$

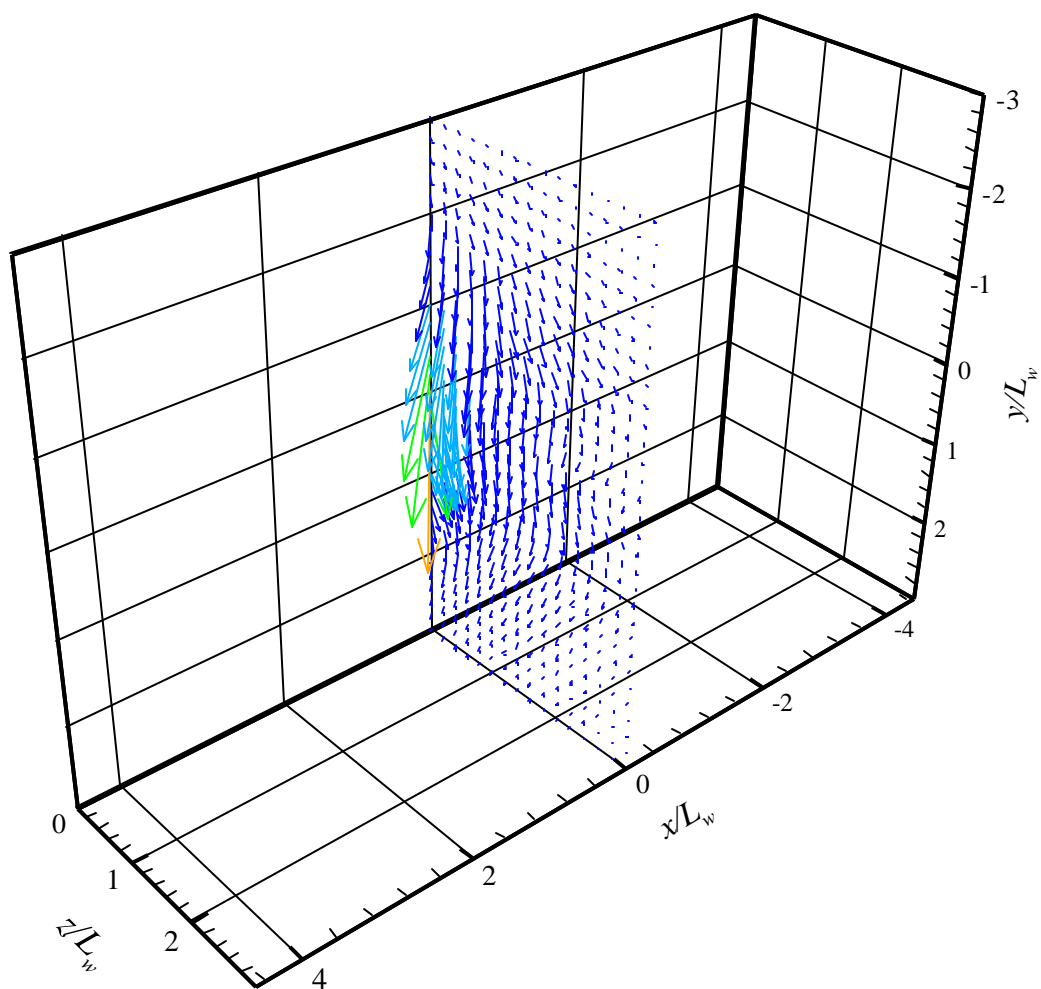


Figure 35(c). Linear stochastic estimate of the velocity field associated with a v fluctuation at $y/L_w=0$

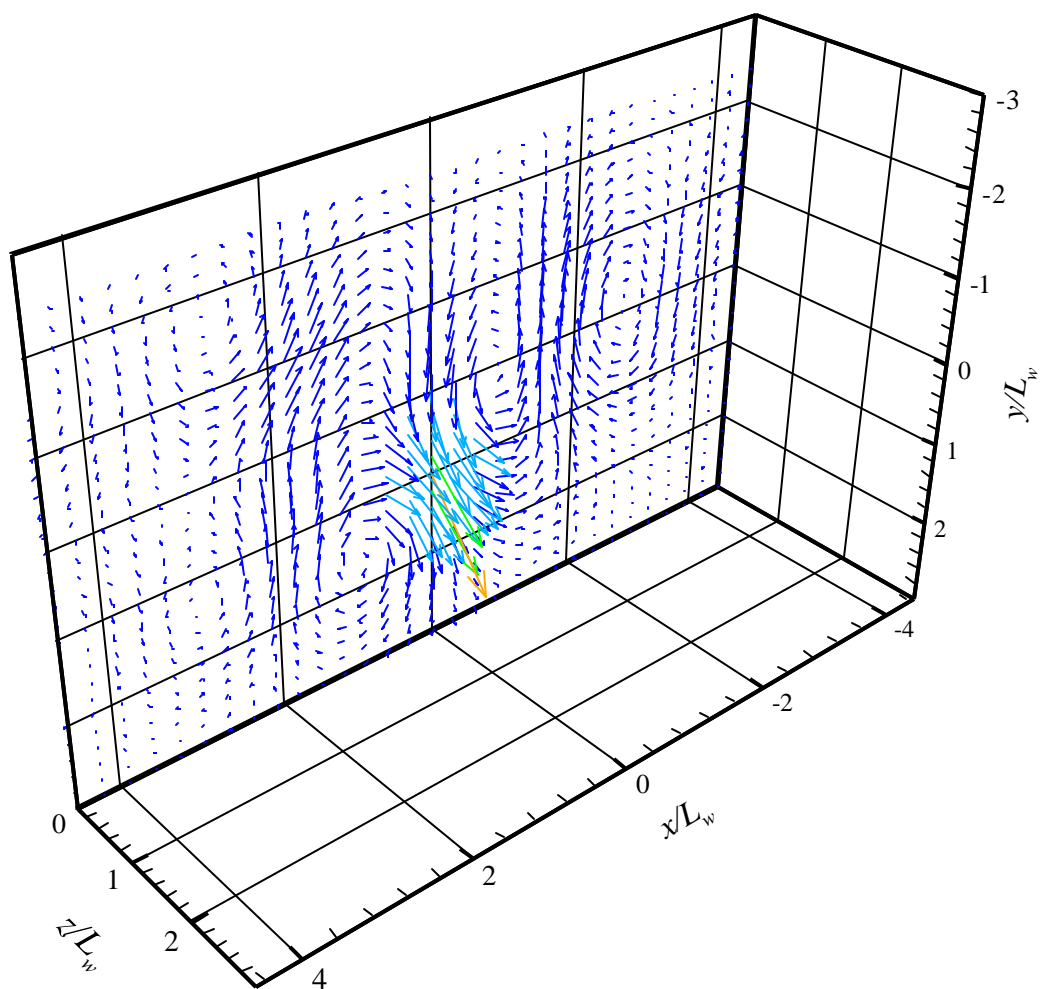


Figure 36(a). Linear stochastic estimate of the velocity field associated with a v fluctuation at $y/L_w=1$

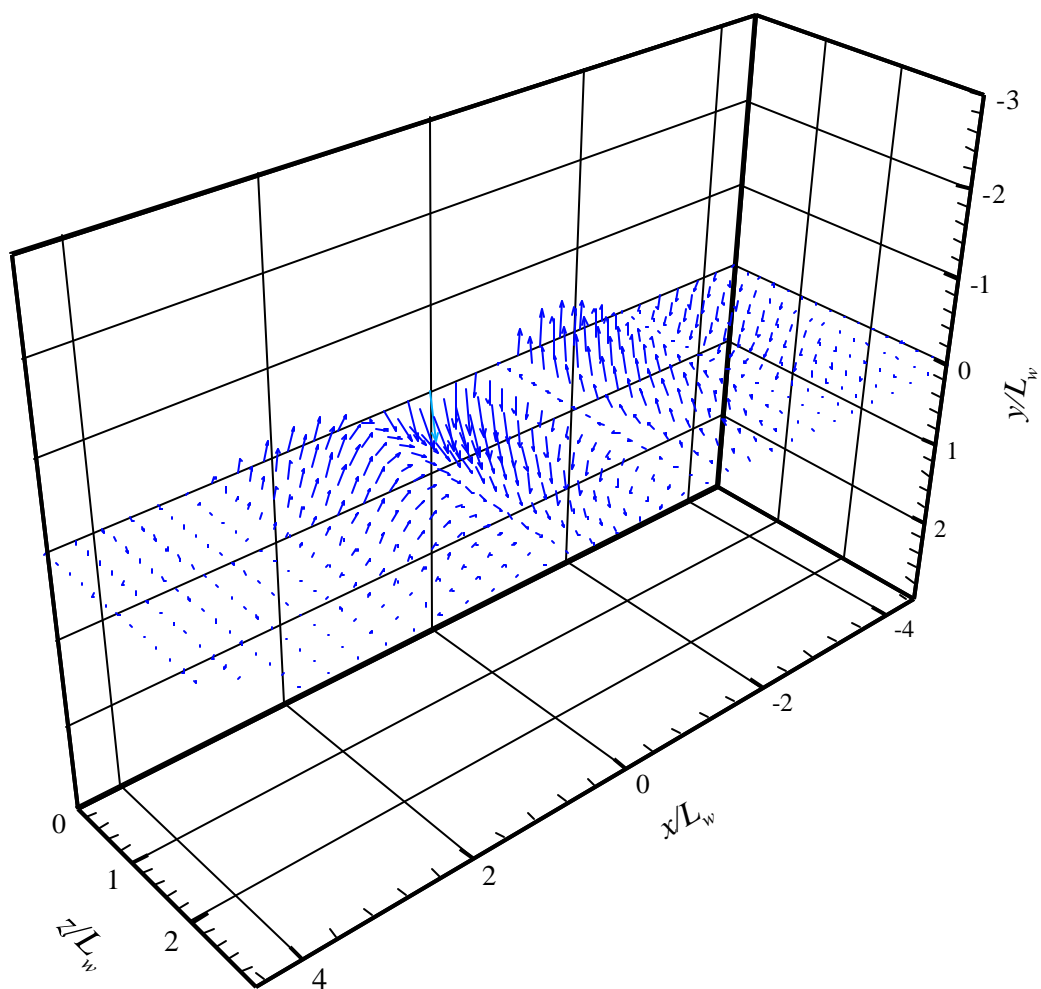


Figure 36(b). Linear stochastic estimate of the velocity field associated with a v fluctuation at $y/L_w=1$

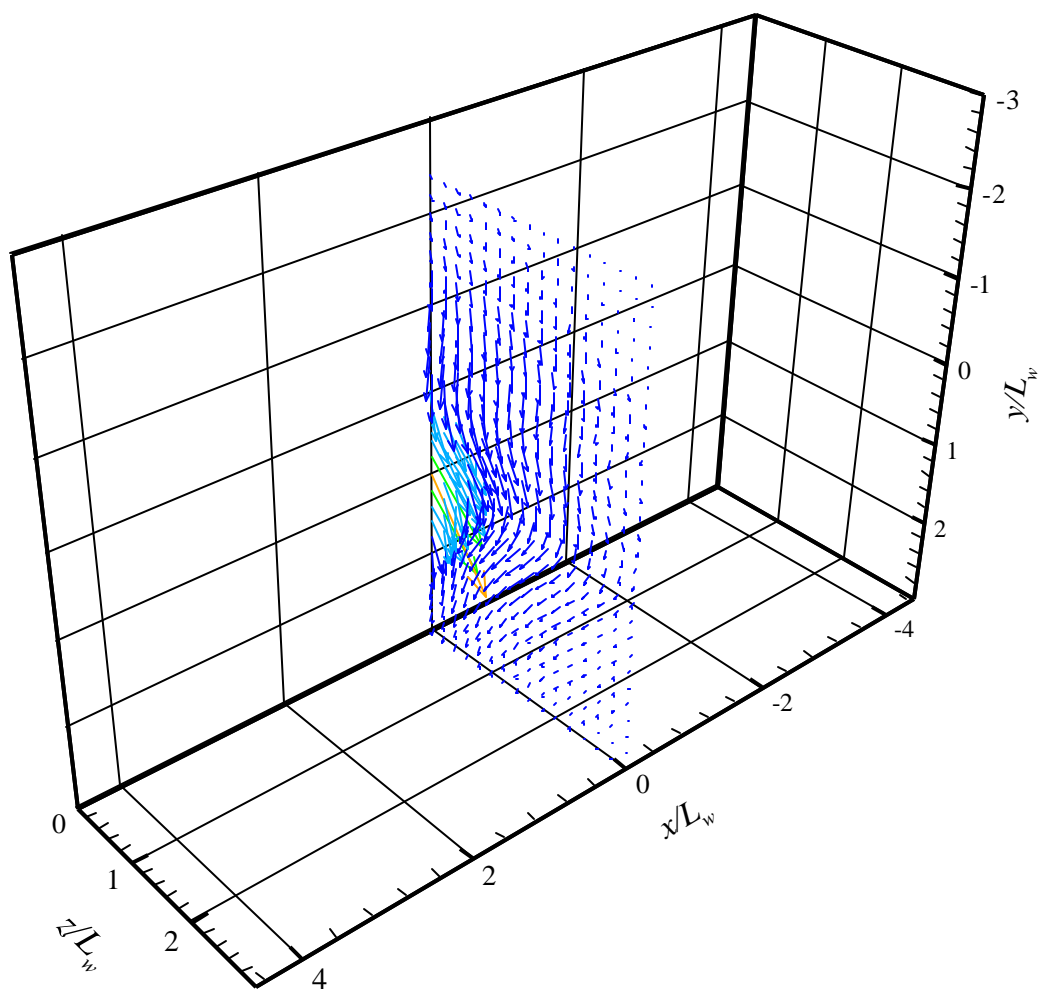


Figure 36(c). Linear stochastic estimate of the velocity field associated with a v fluctuation at $y/L_w=1$

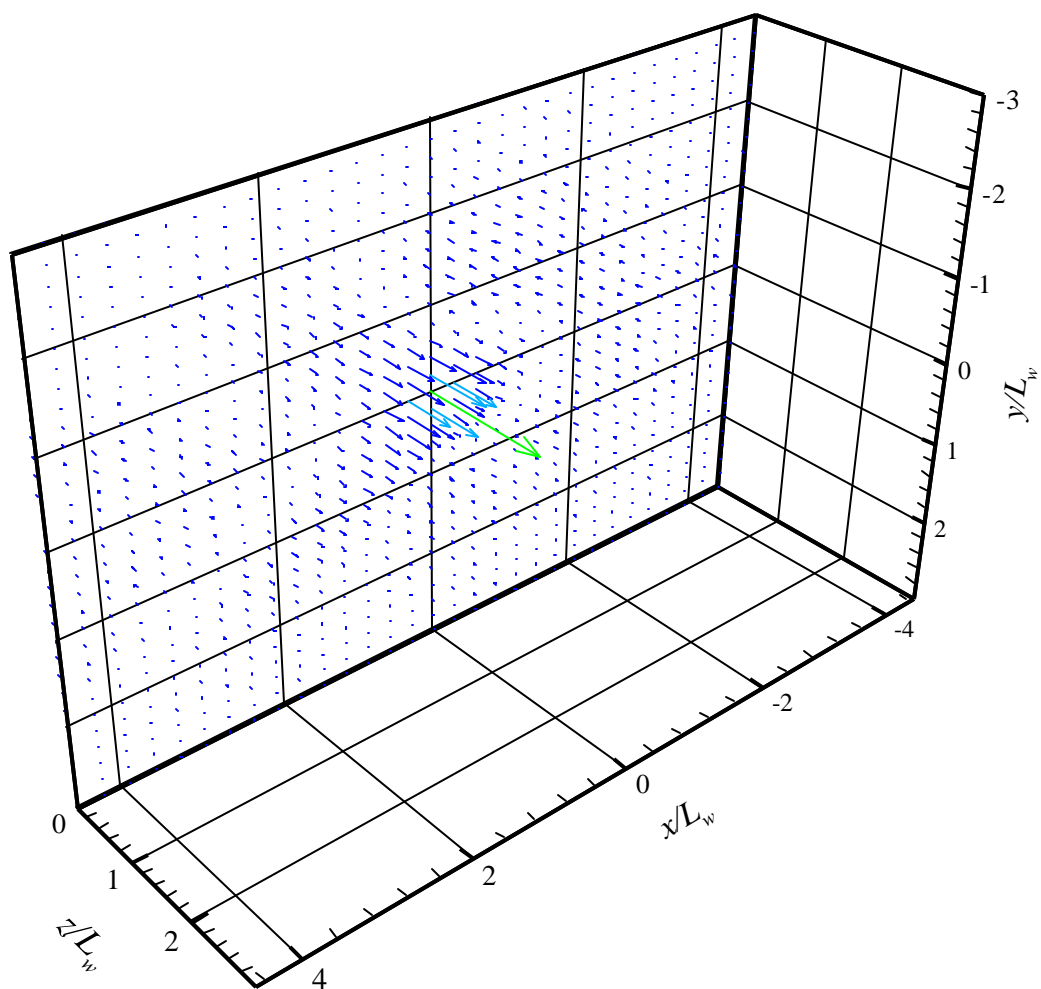


Figure 37(a). Linear stochastic estimate of the velocity field associated with a w fluctuation at $y/L_w=0$

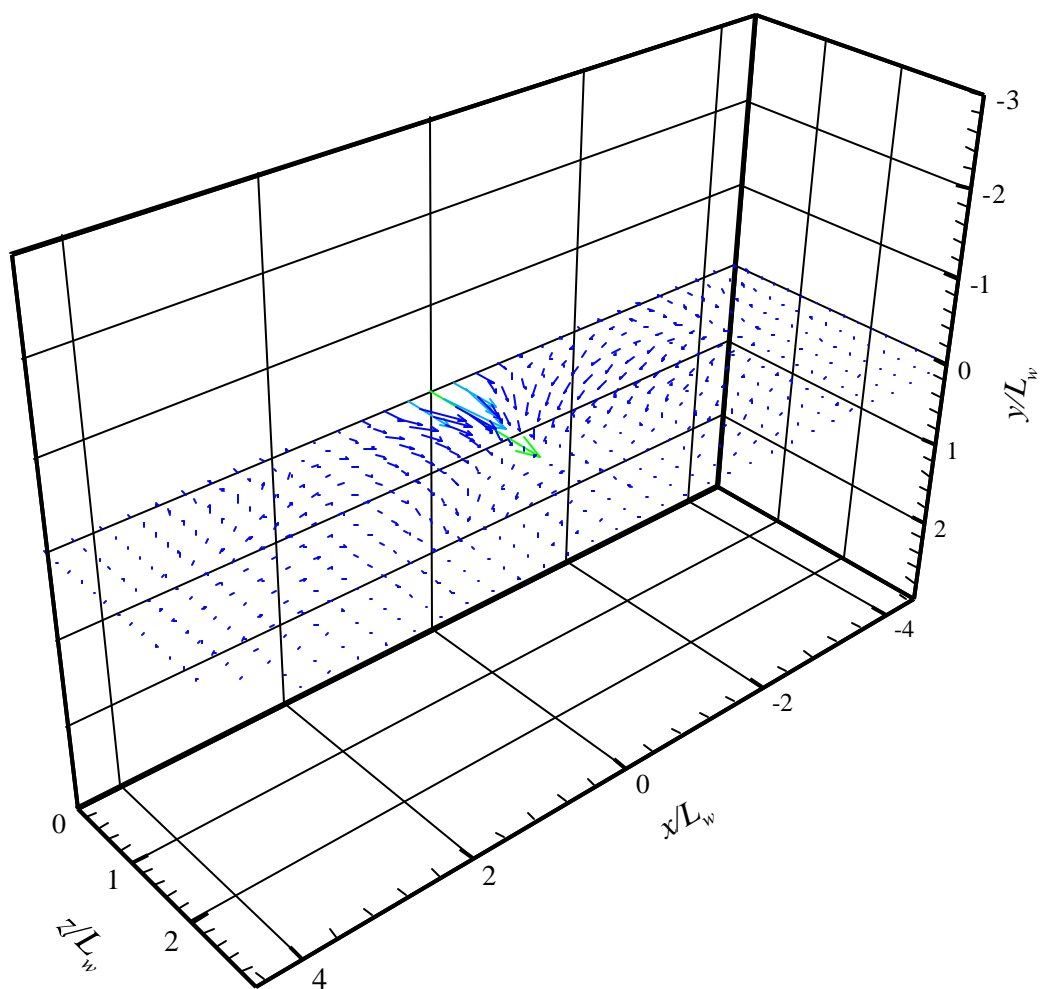


Figure 37(b). Linear stochastic estimate of the velocity field associated with a w fluctuation at $y/L_w=0$

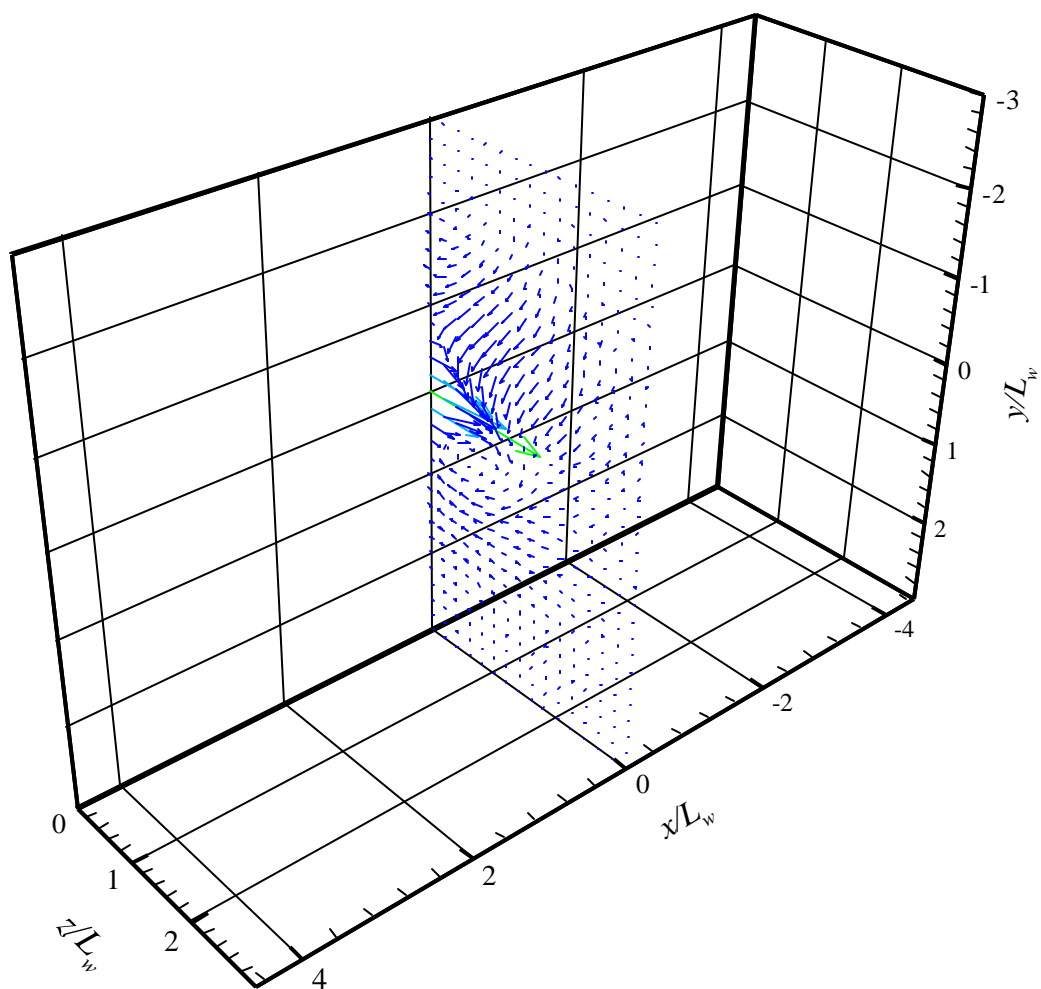


Figure 37(c). Linear stochastic estimate of the velocity field associated with a w fluctuation at $y/L_w=0$

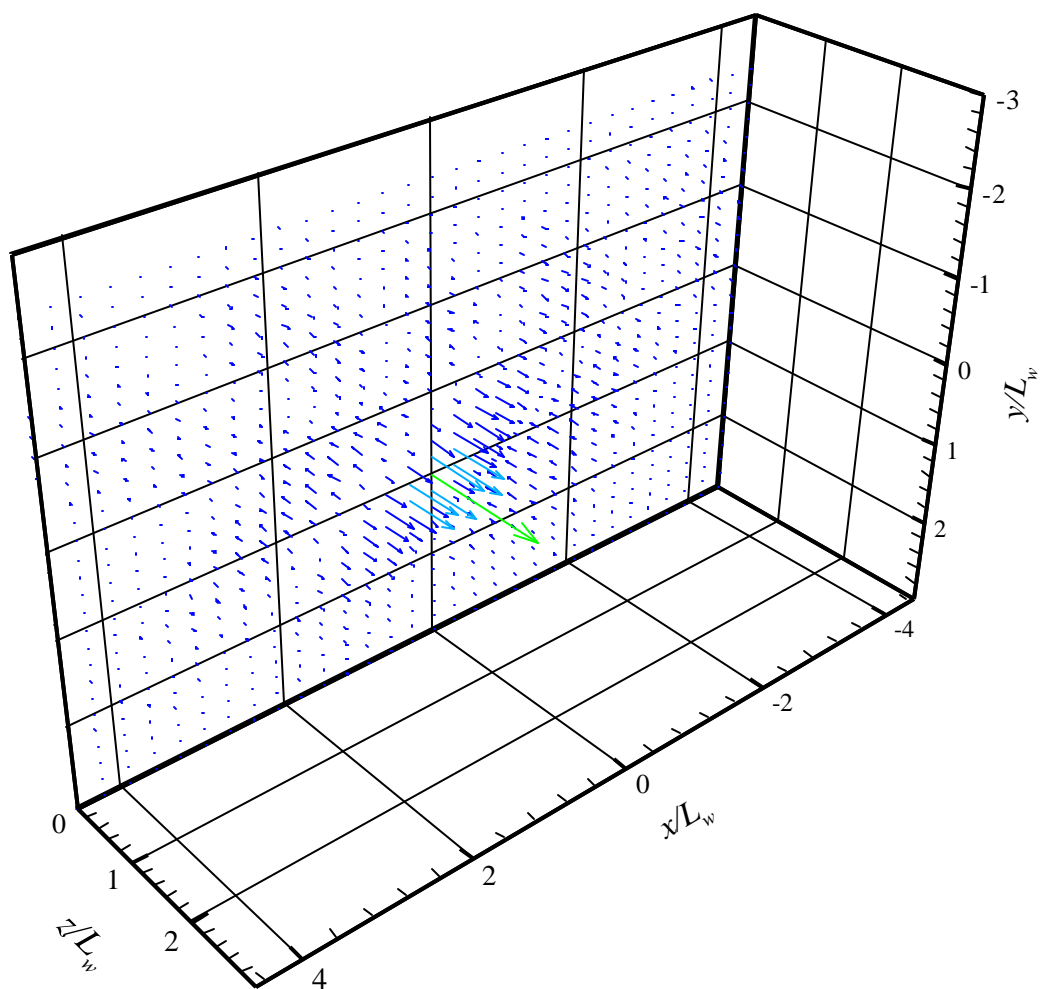


Figure 38(a). Linear stochastic estimate of the velocity field associated with a w fluctuation at $y/L_w=1$

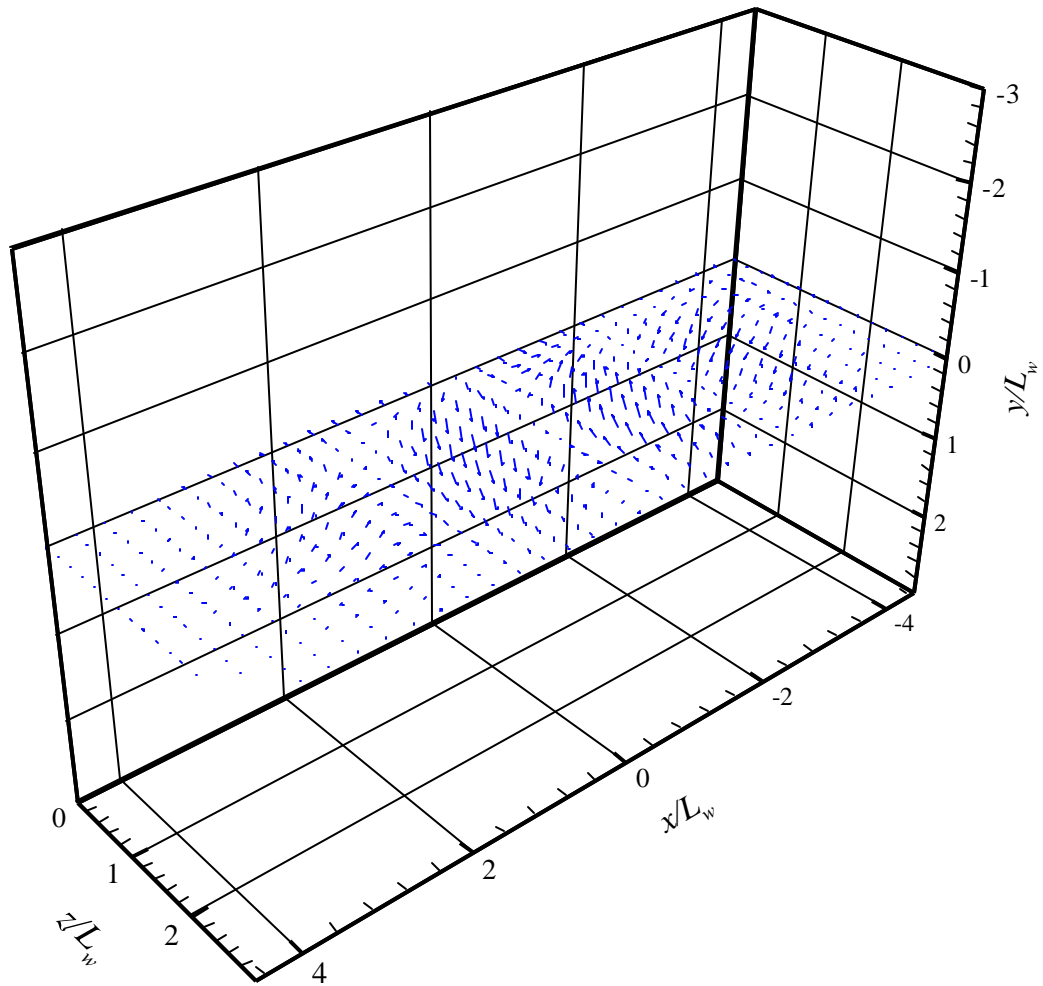


Figure 38(b). Linear stochastic estimate of the velocity field associated with a w fluctuation at $y/L_w=1$

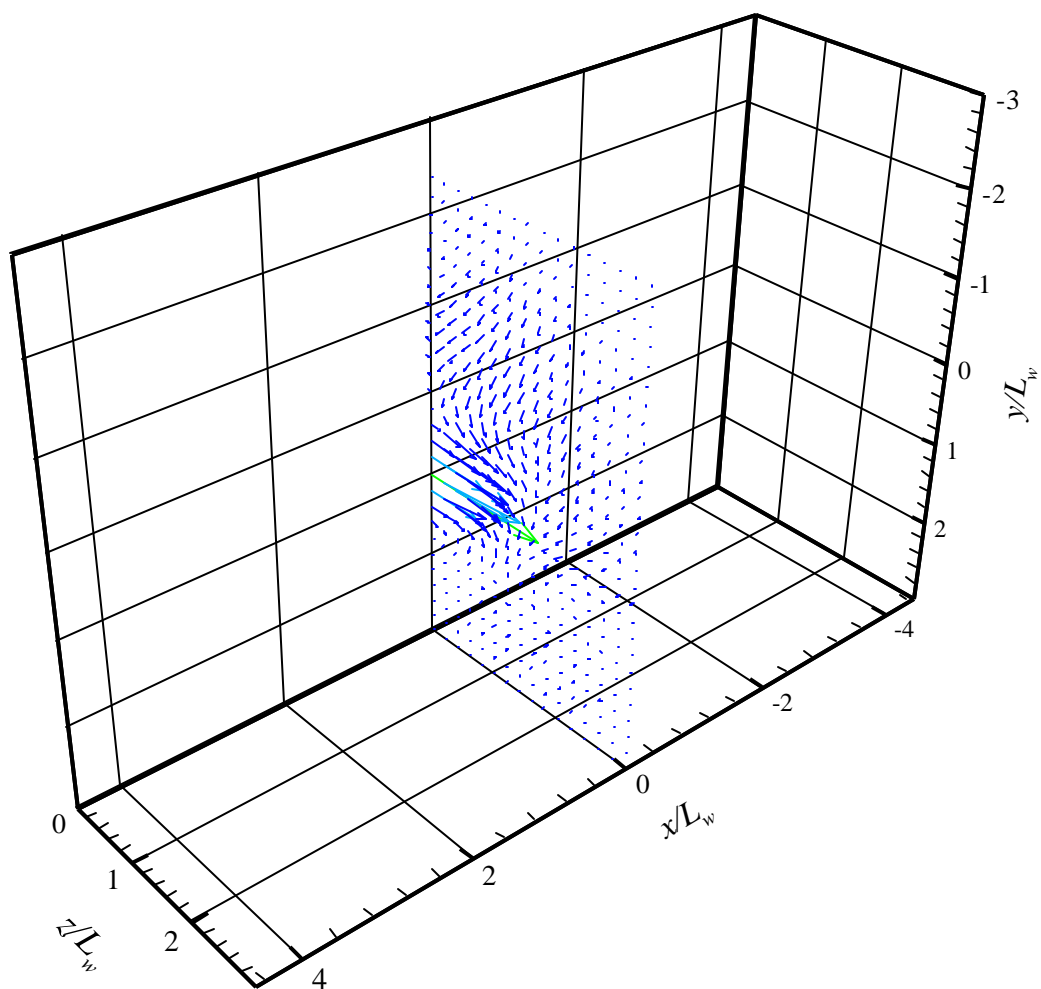


Figure 38(c). Linear stochastic estimate of the velocity field associated with a w fluctuation at $y/L_w=1$

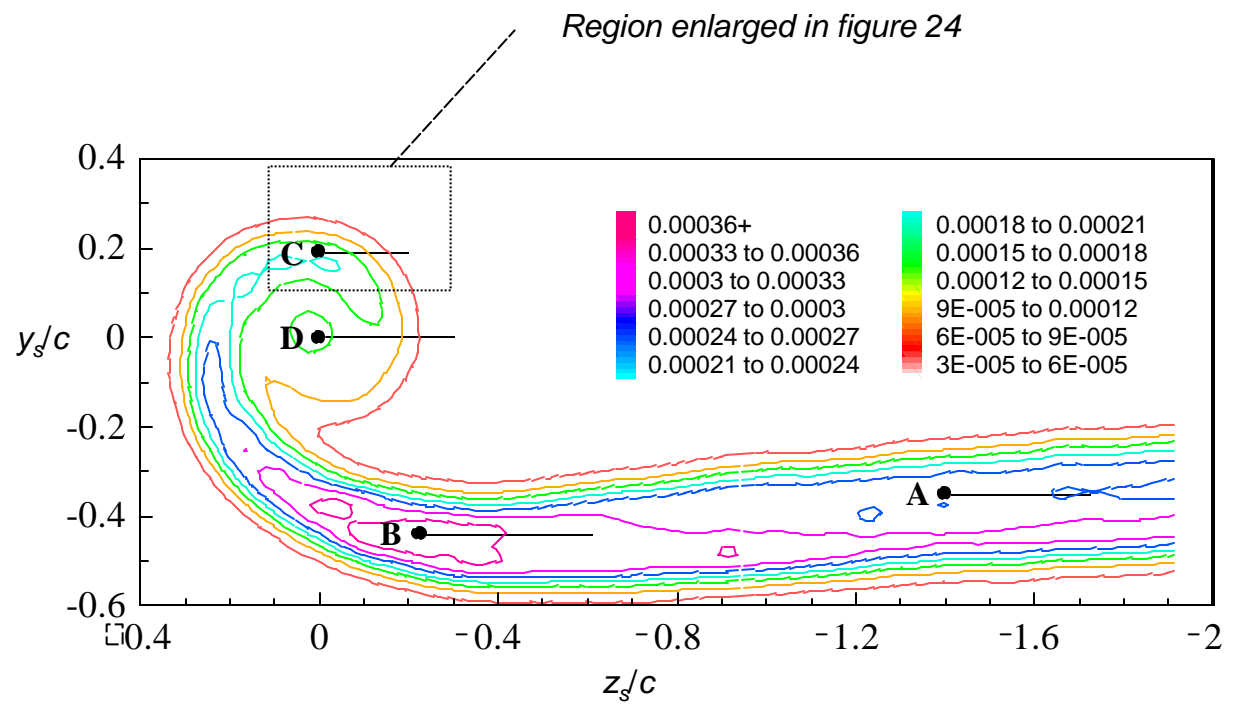


Figure 39. Contours of axial turbulence normal stress normalized on edge velocity for the lifting wake flow of Miranda (1996), Devenport *et al.* (1998) and Wenger (1999). Points/lines A, B, C and D show locations of two-point measurements.

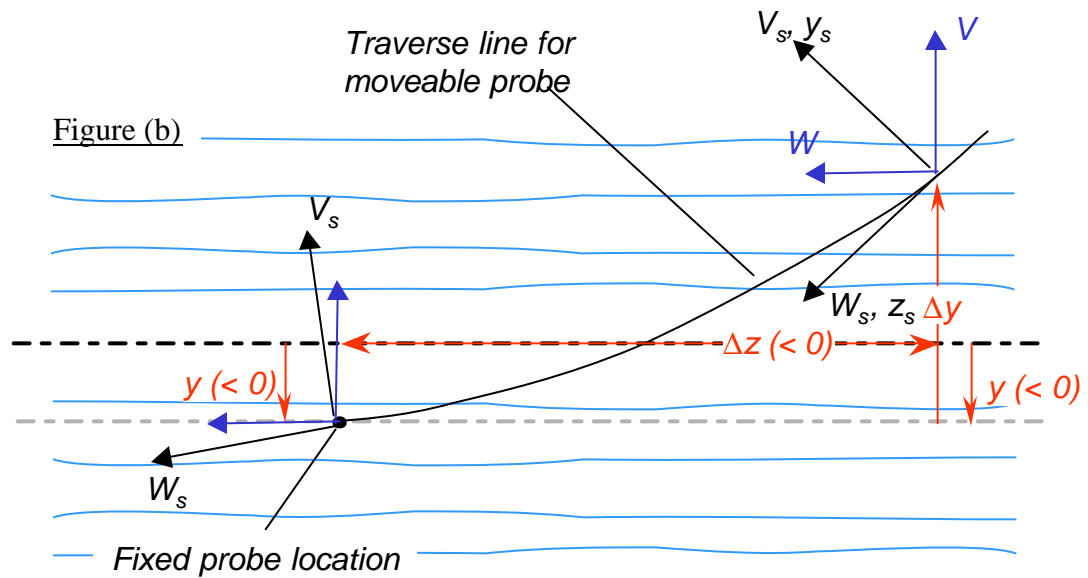
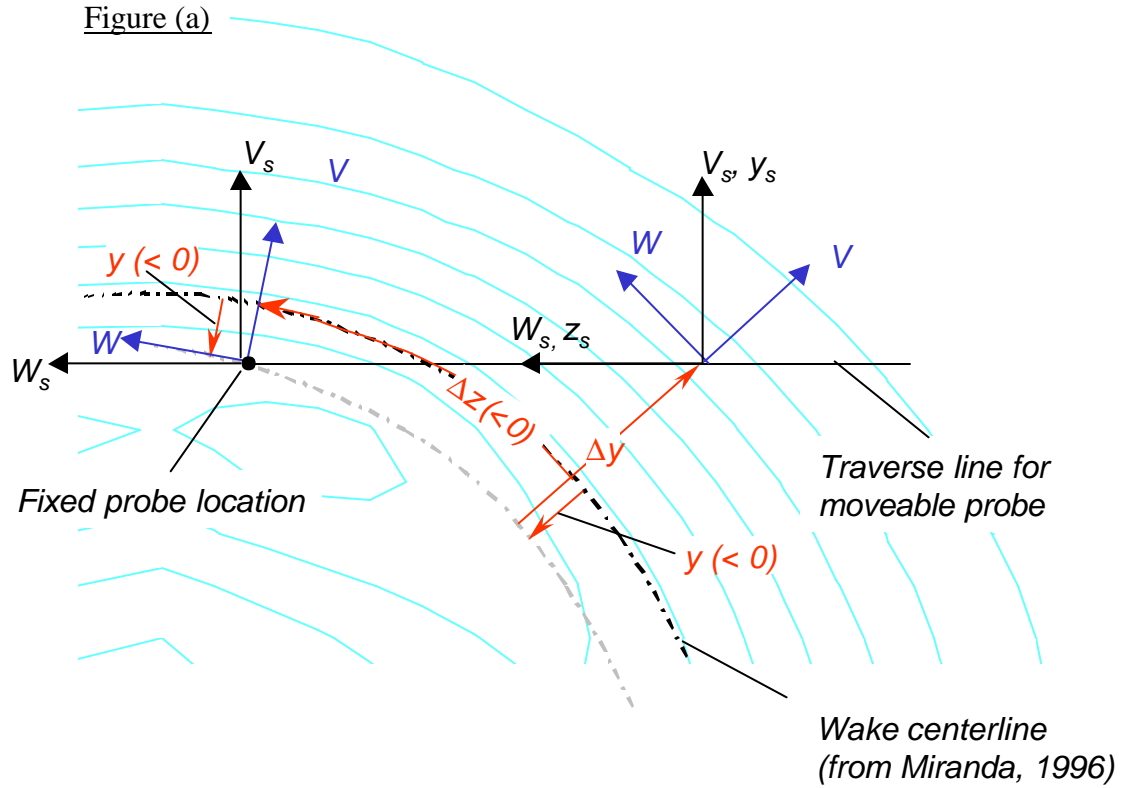


Figure 40. Relationship between (a) curvilinear coordinate system based on spiral-wake centerline and two-point traverse line, and (b) cartesian coordinate system of plane wake two-point correlation data. Coordinates x , x_s and components u , u_s are directed in the flow direction out of the paper.

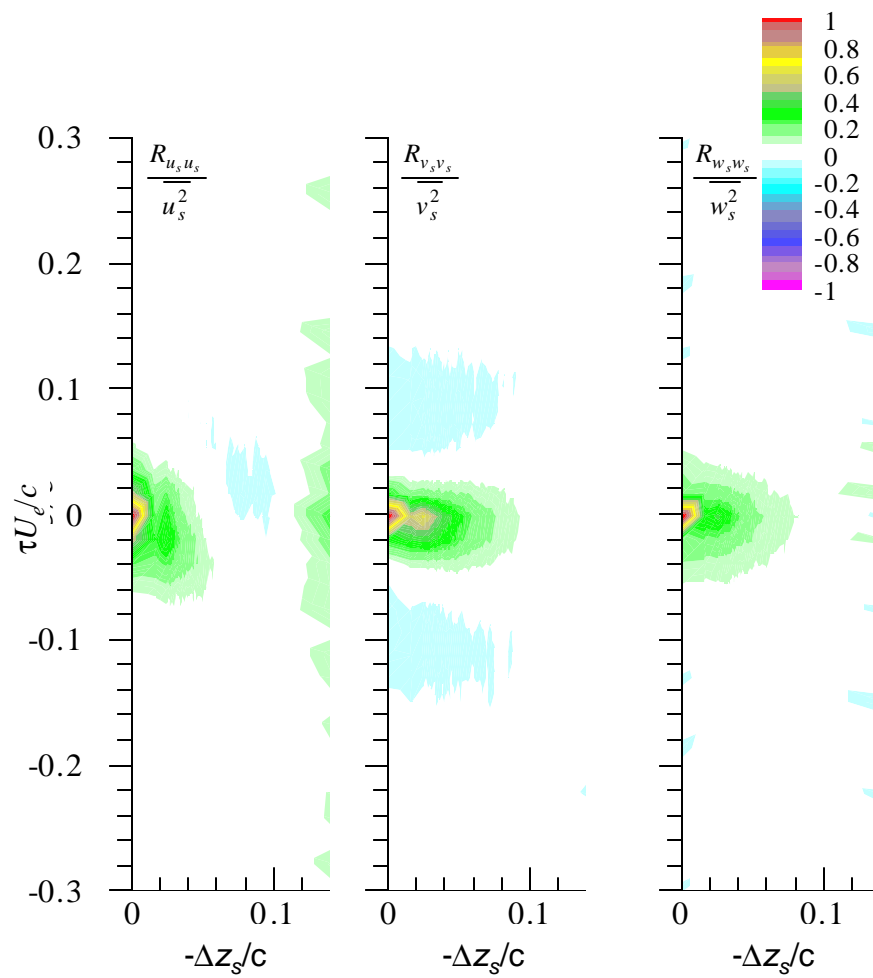


Figure 41(a). Space time correlation maps for the spiral wake, point/line C, as measured by Devenport *et al.* (1998).

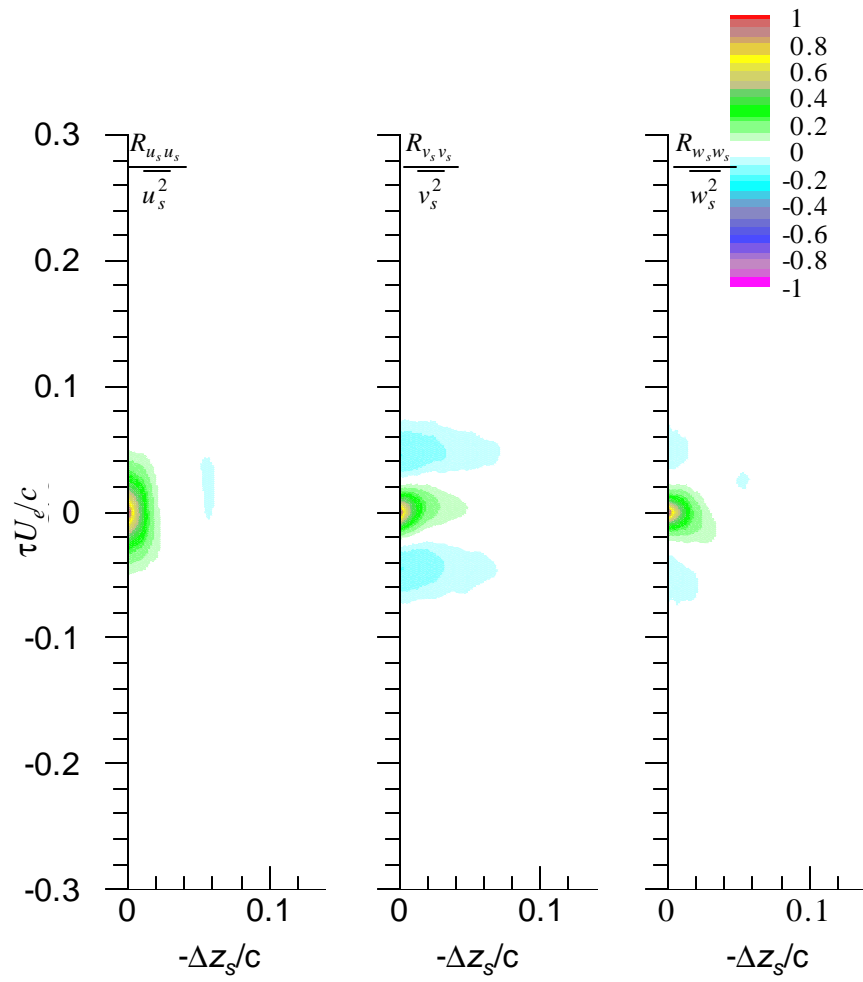


Figure 41(b). Space time correlation maps for the spiral wake, point/line C, estimated from plane wake data with $L_w/c = 0.0276$.

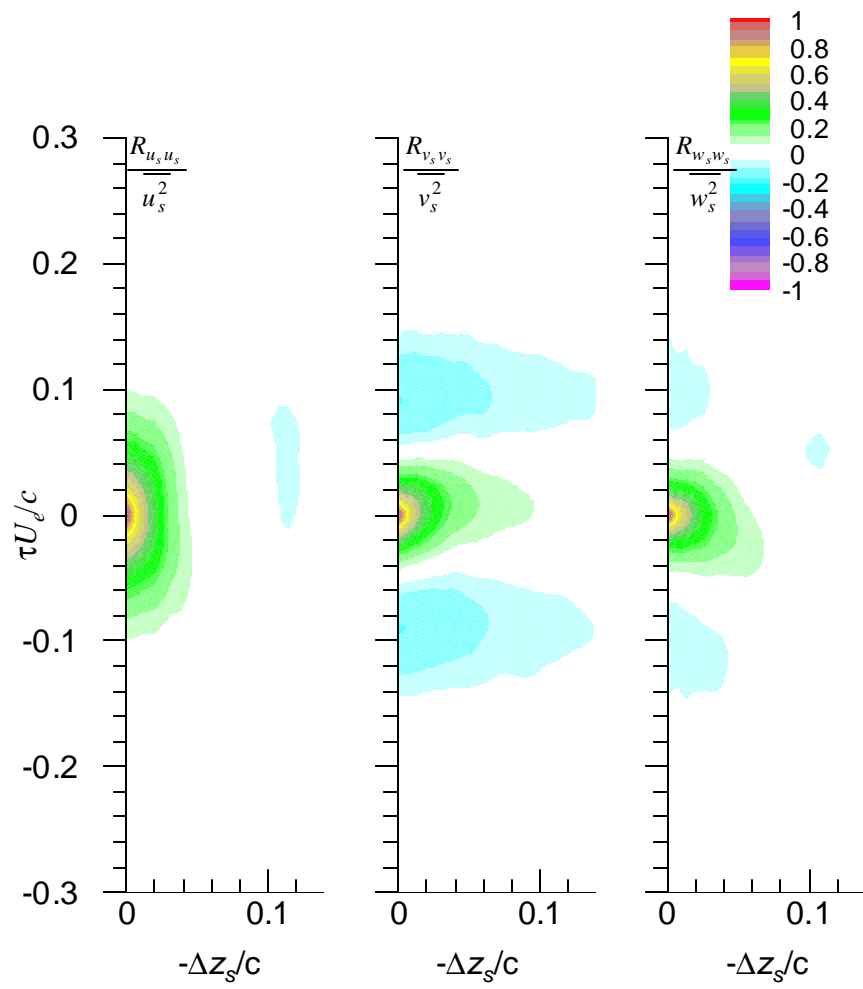


Figure 41(c). Space time correlation maps for the spiral wake, point/line C, estimated from plane wake data with $L_w/c = 0.0551$.

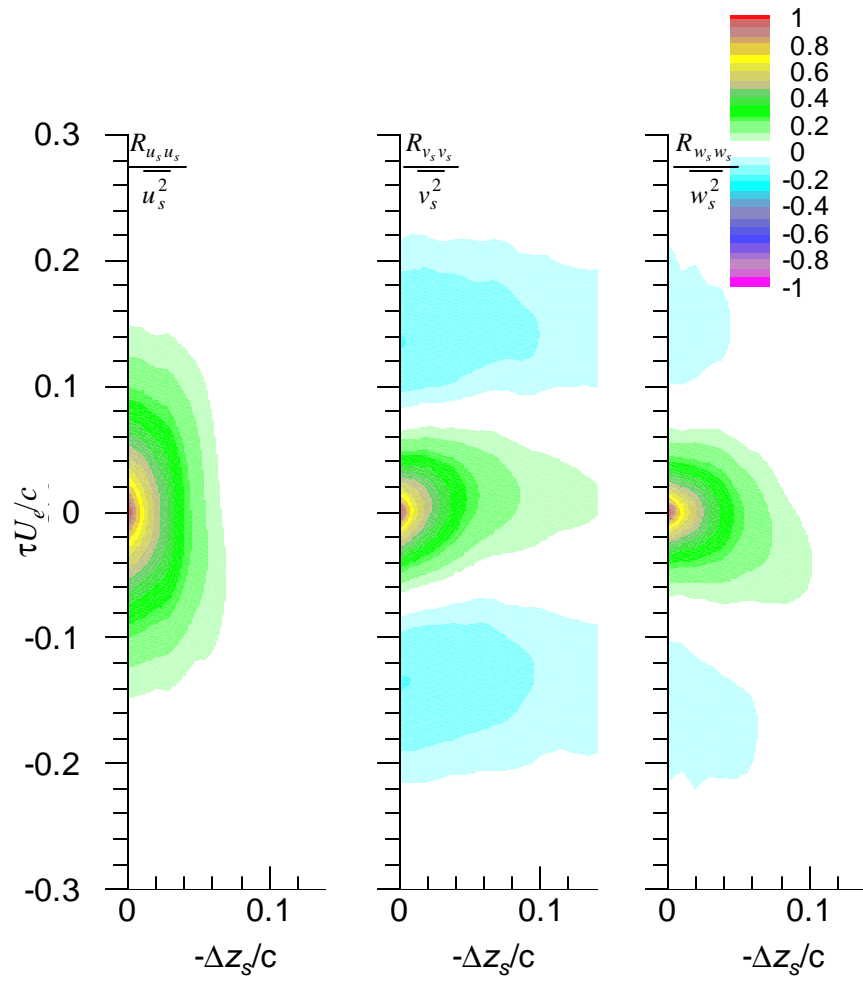


Figure 41(d). Space time correlation maps for the spiral wake, point/line C, estimated from plane wake data with $L_w/c = 0.0827$.

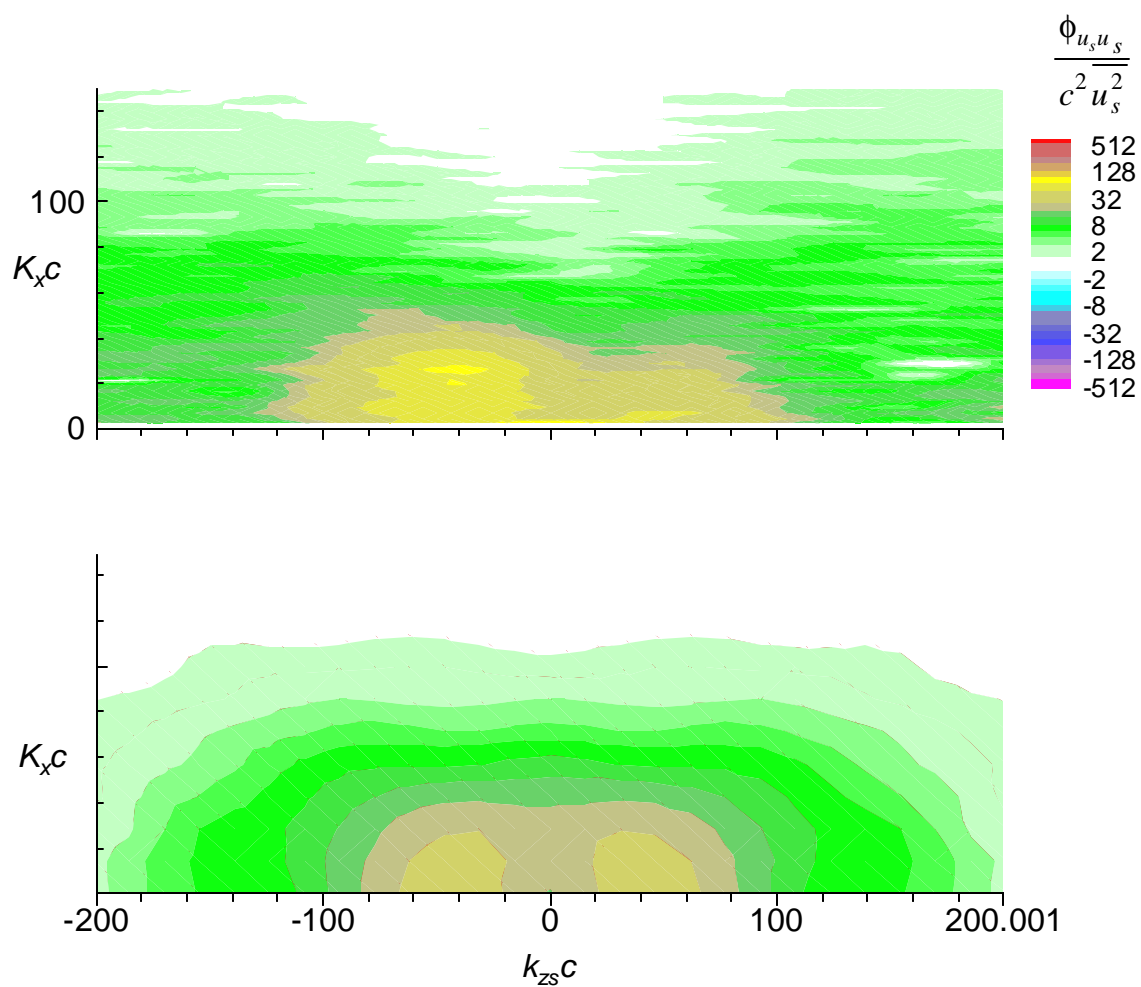


Figure 42. Pointwise wavenumber frequency spectra for the spiral wake, point/line C, u_s component. Top - measured, bottom - estimated from plane wake data. (a) $L_w/c = 0.0276$.

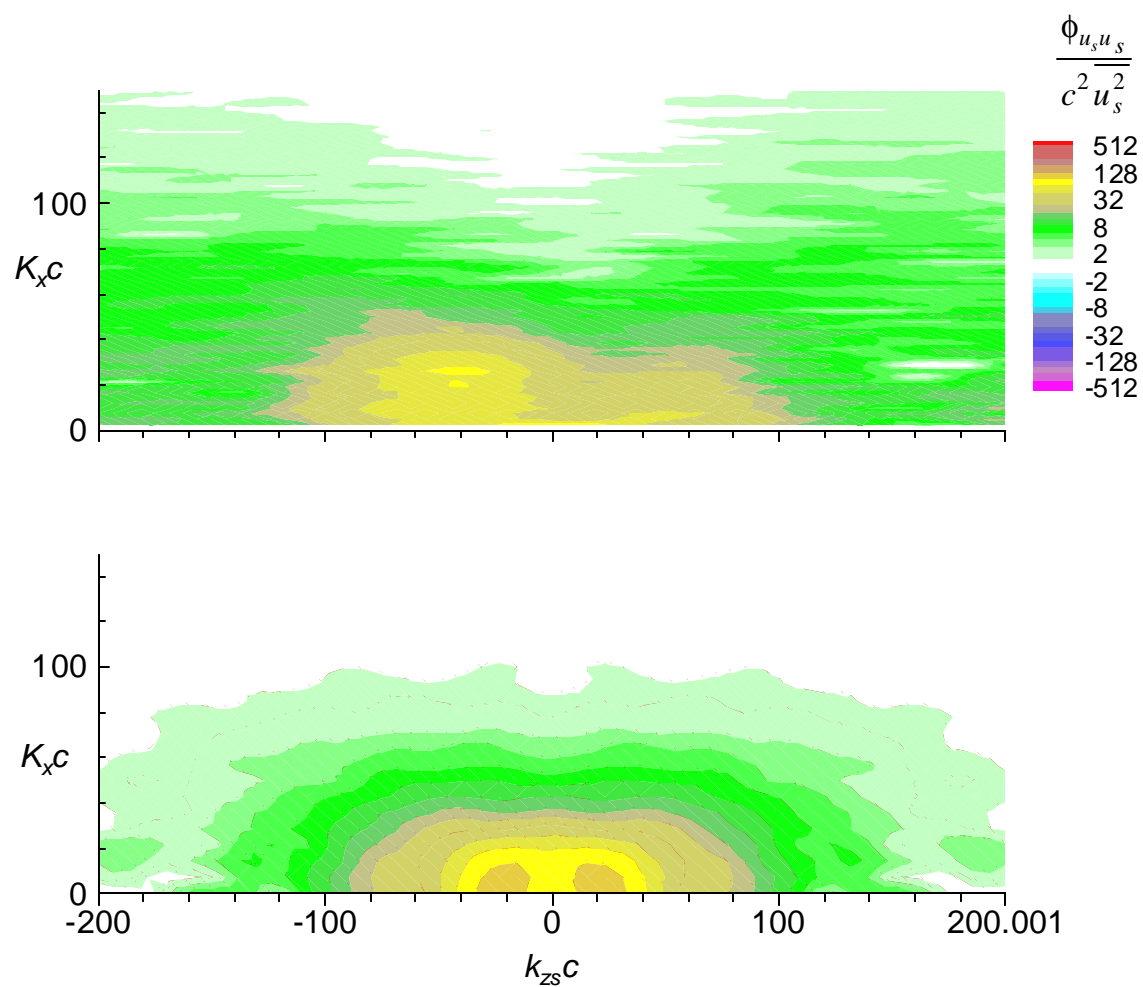


Figure 42. Pointwise wavenumber frequency spectra for the spiral wake, point/line C, u_s component. Top - measured, bottom - estimated from plane wake data. (b) $L_w/c = 0.0551$.

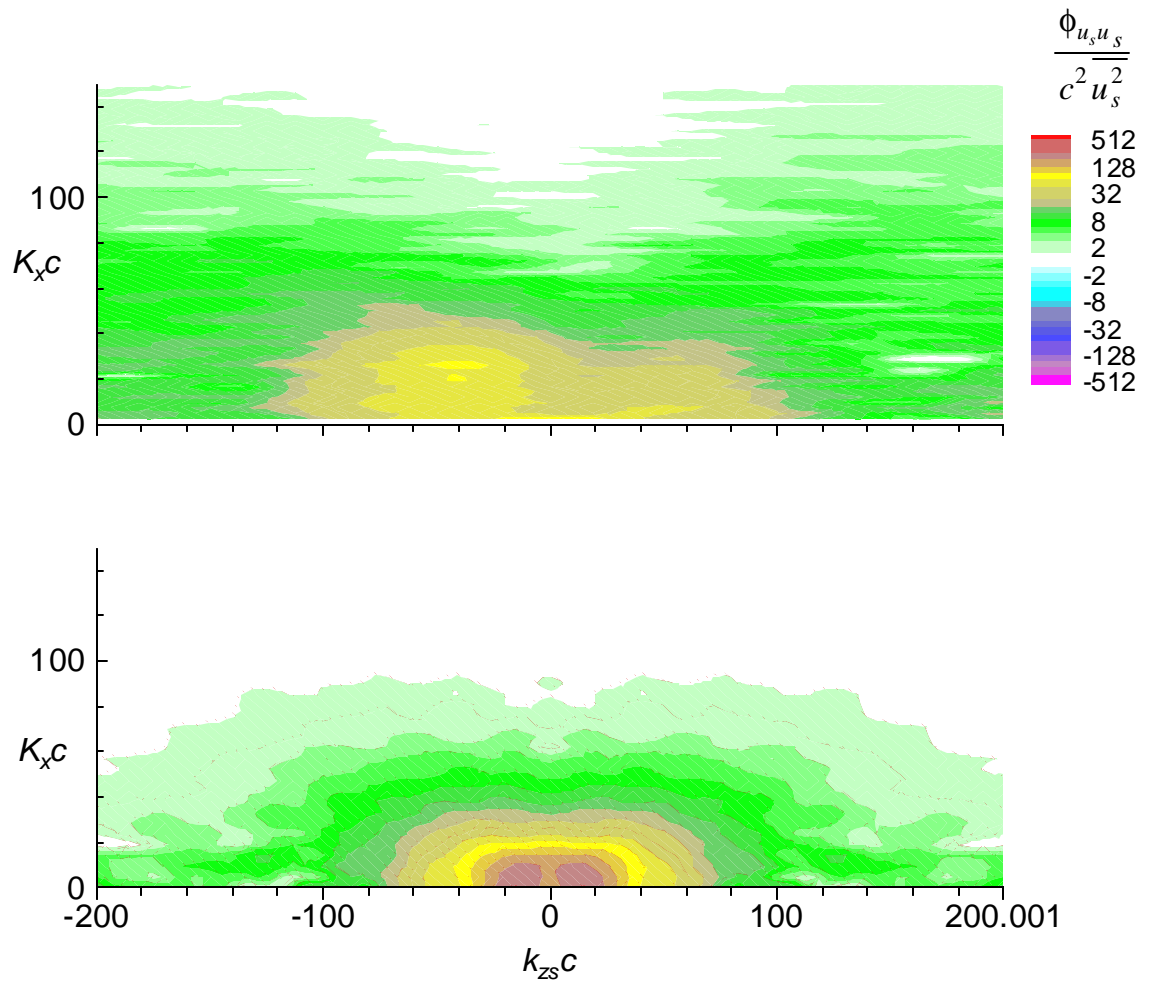


Figure 42. Pointwise wavenumber frequency spectra for the spiral wake, point/line C, u_s component. Top - measured, bottom - estimated from plane wake data. (c) $L_w/c = 0.0827$.

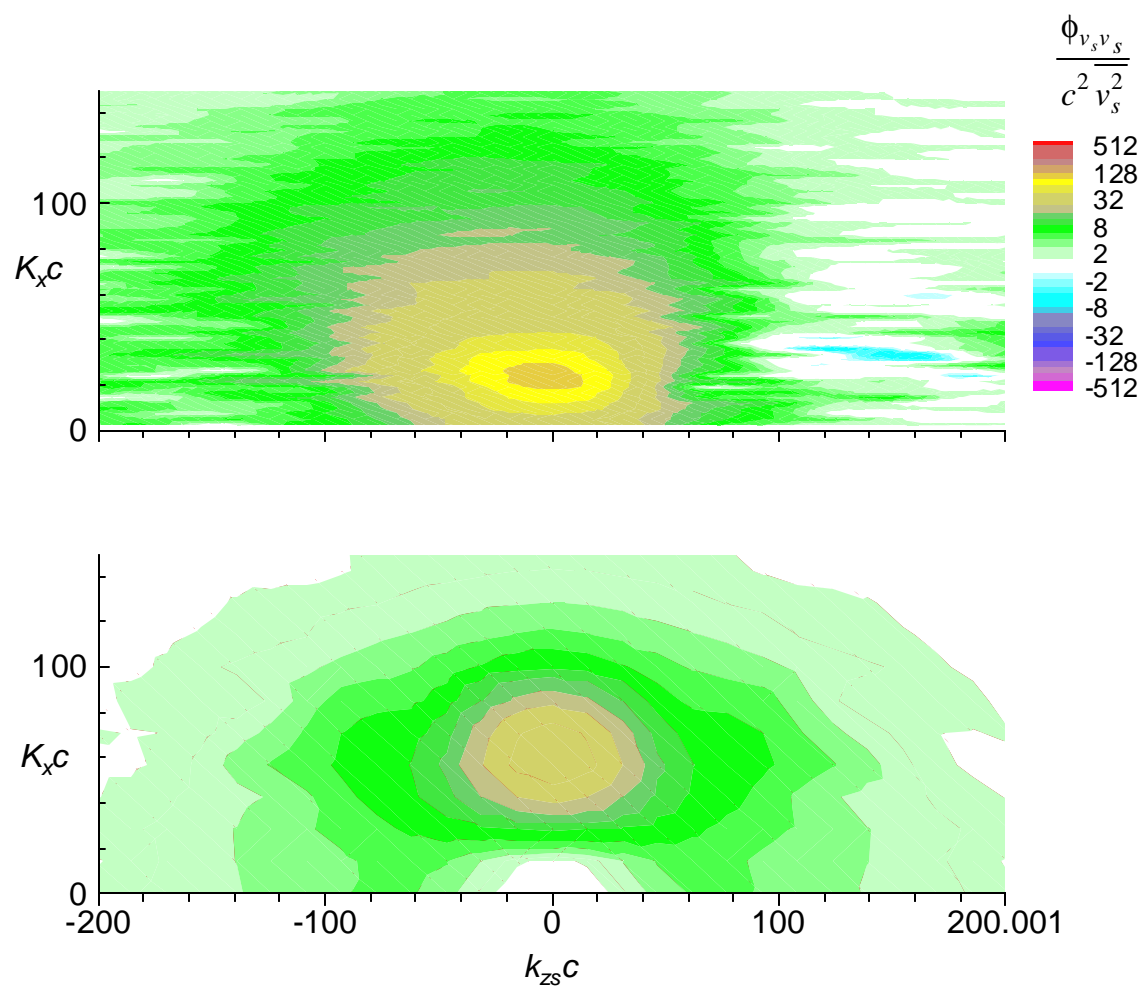


Figure 43. Pointwise wavenumber frequency spectra for the spiral wake, point/line C, v_s component. Top - measured, bottom - estimated from plane wake data. (a) $L_w/c = 0.0276$.

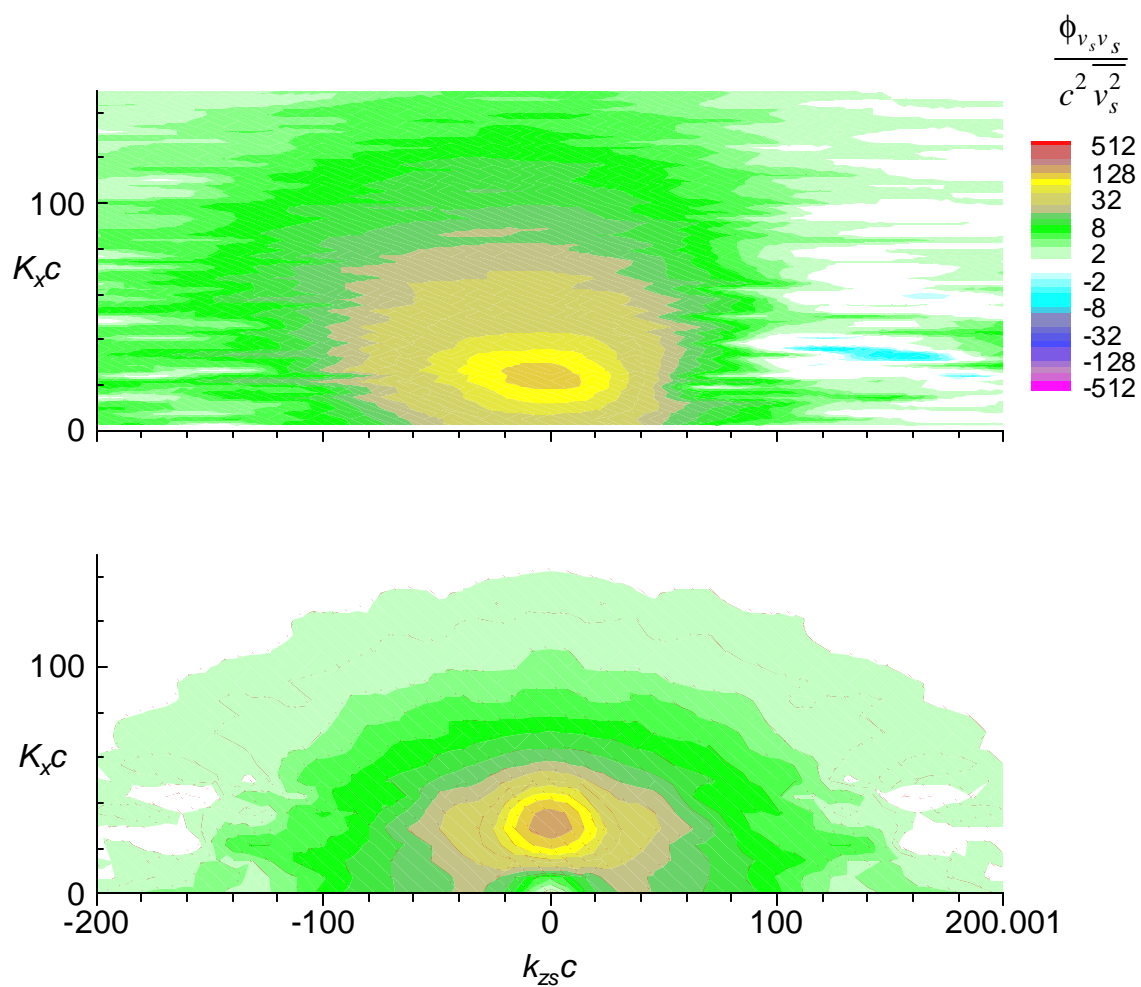


Figure 43. Pointwise wavenumber frequency spectra for the spiral wake, point/line C, v_s component. Top - measured, bottom - estimated from plane wake data. (b) $L_w/c = 0.0551$.

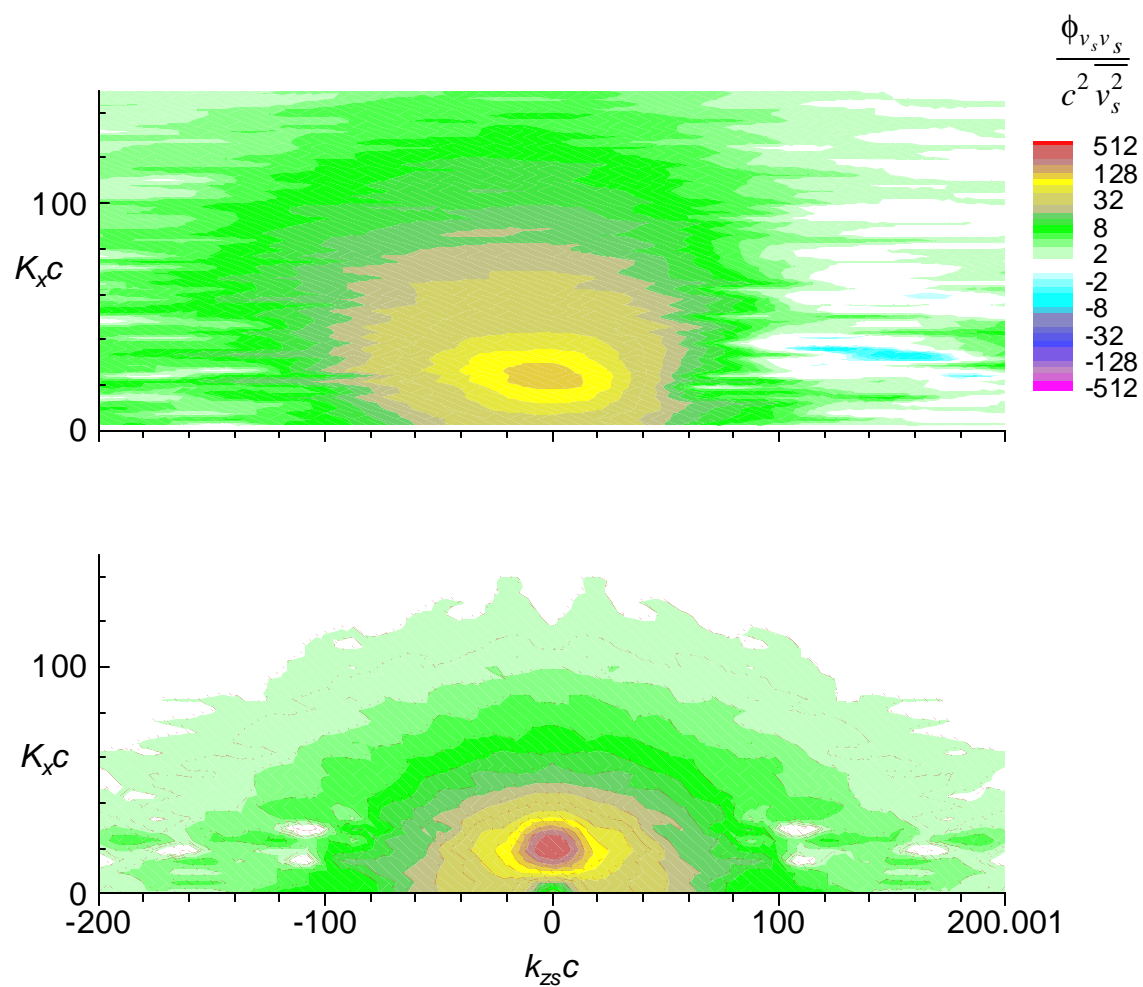


Figure 43. Pointwise wavenumber frequency spectra for the spiral wake, point/line C, v_s component. Top - measured, bottom - estimated from plane wake data. (c) $L_w/c = 0.0827$.

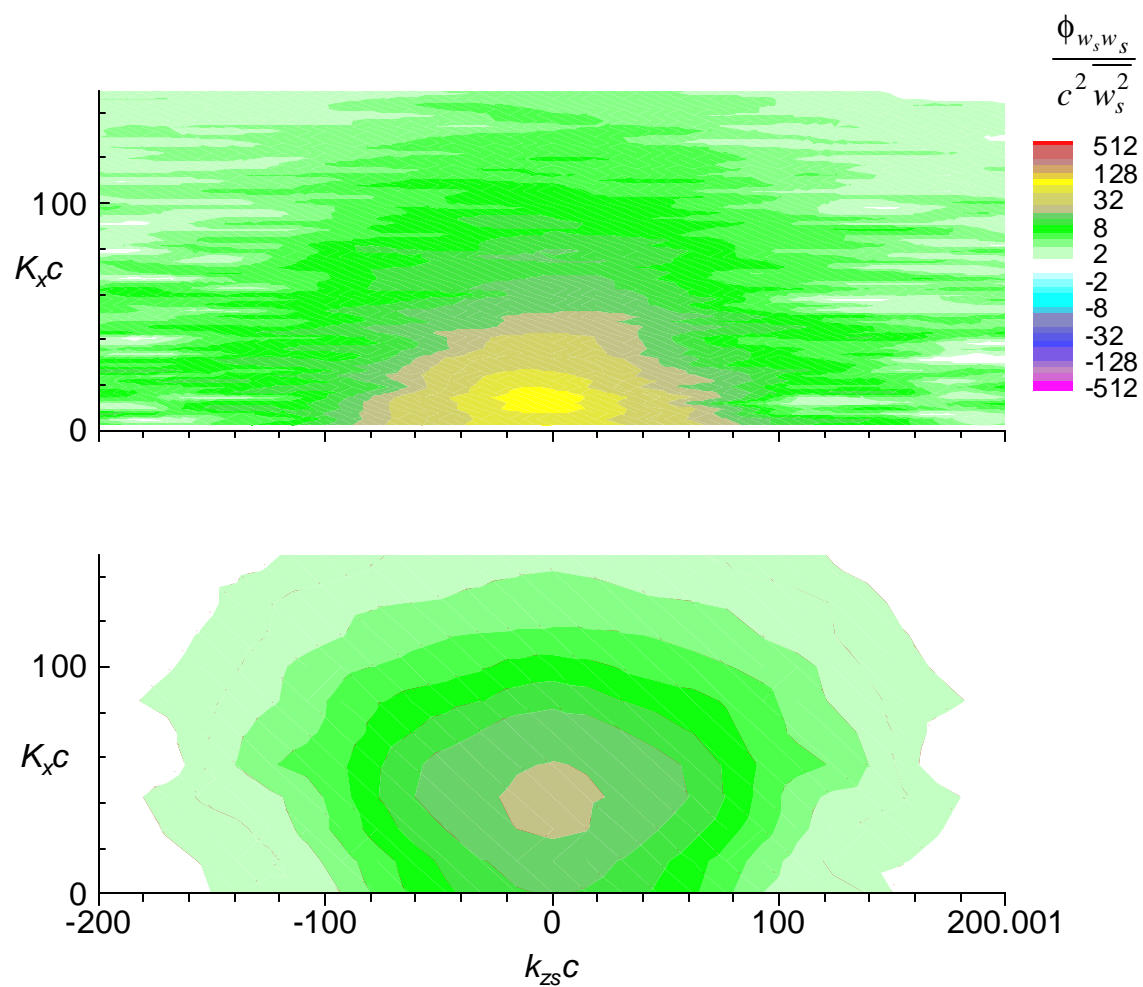


Figure 44. Pointwise wavenumber frequency spectra for the spiral wake, point/line C, w_s component. Top - measured, bottom - estimated from plane wake data. (a) $L_w/c = 0.0276$.

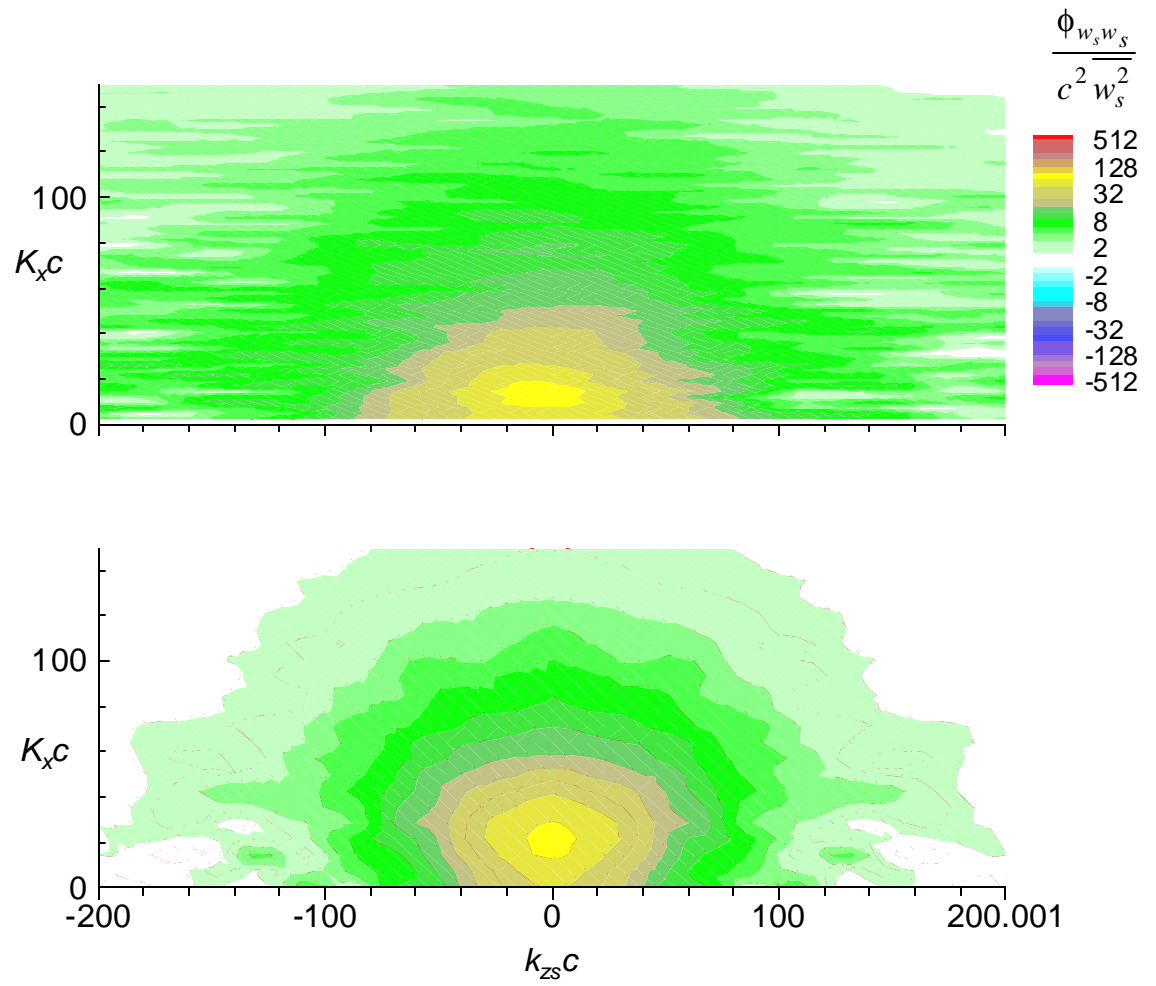


Figure 44. Pointwise wavenumber frequency spectra for the spiral wake, point/line C, w_s component. Top - measured, bottom - estimated from plane wake data. (b) $L_w/c = 0.0551$.

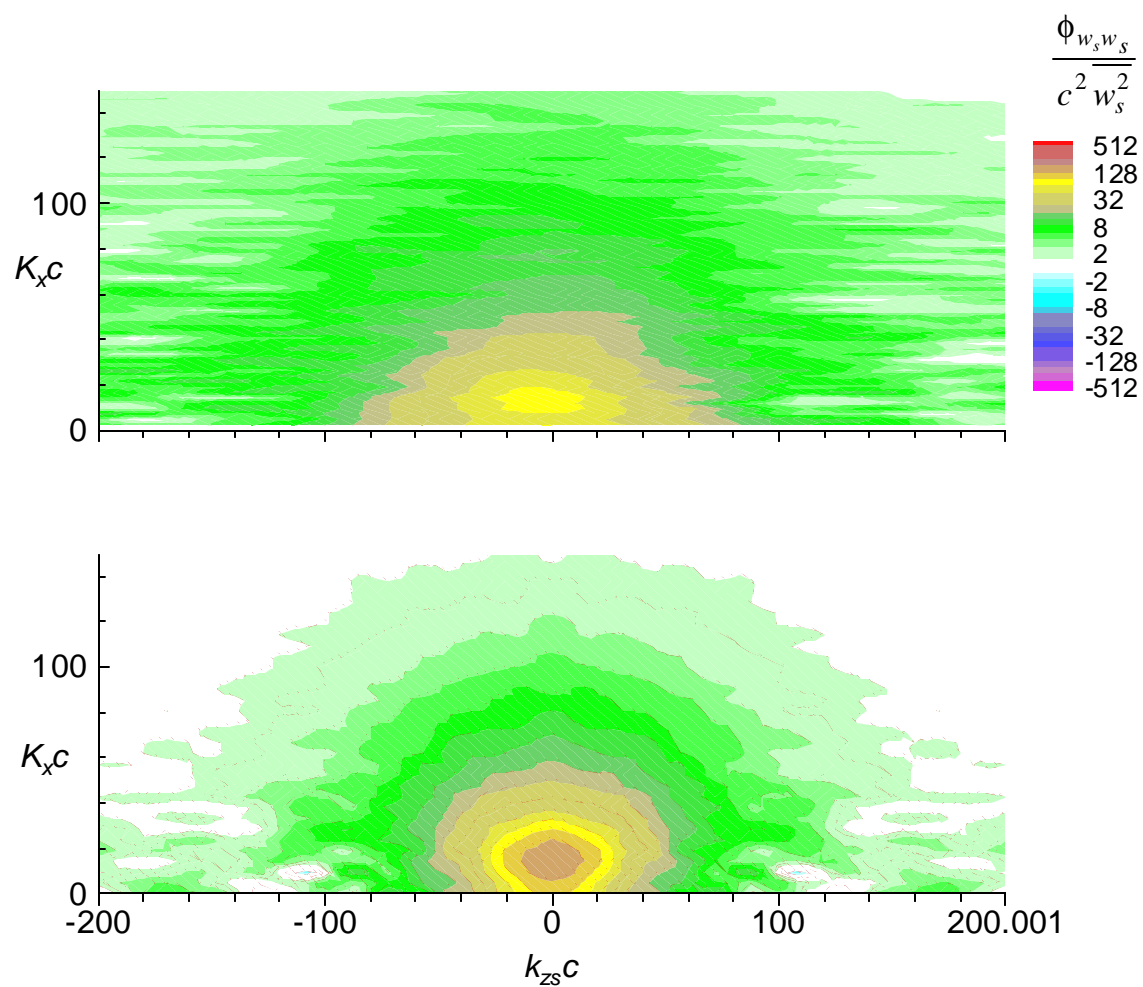


Figure 44. Pointwise wavenumber frequency spectra for the spiral wake, point/line C, w_s component. Top - measured, bottom - estimated from plane wake data. (c) $L_w/c = 0.0827$.

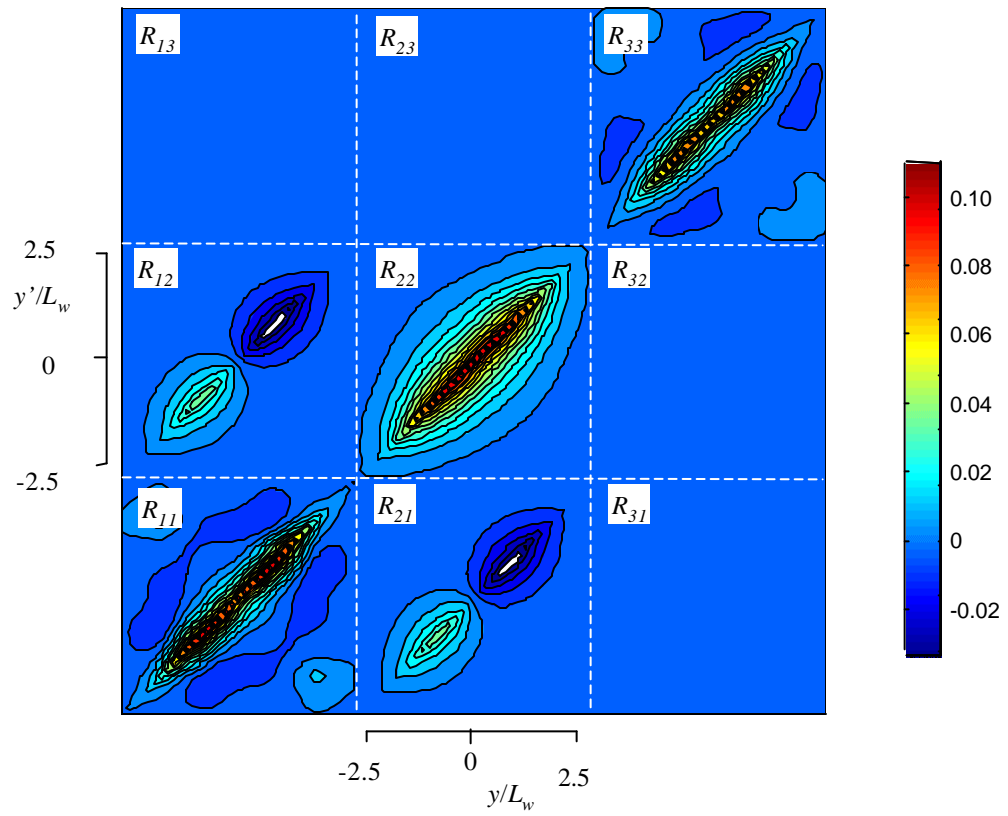


Figure 45. Correlation maps for zero time delay (Δx) and spanwise separation $R_{ij}(y, y', 0, 0) / U_w^2$ computed using the model (compare with figure 23).

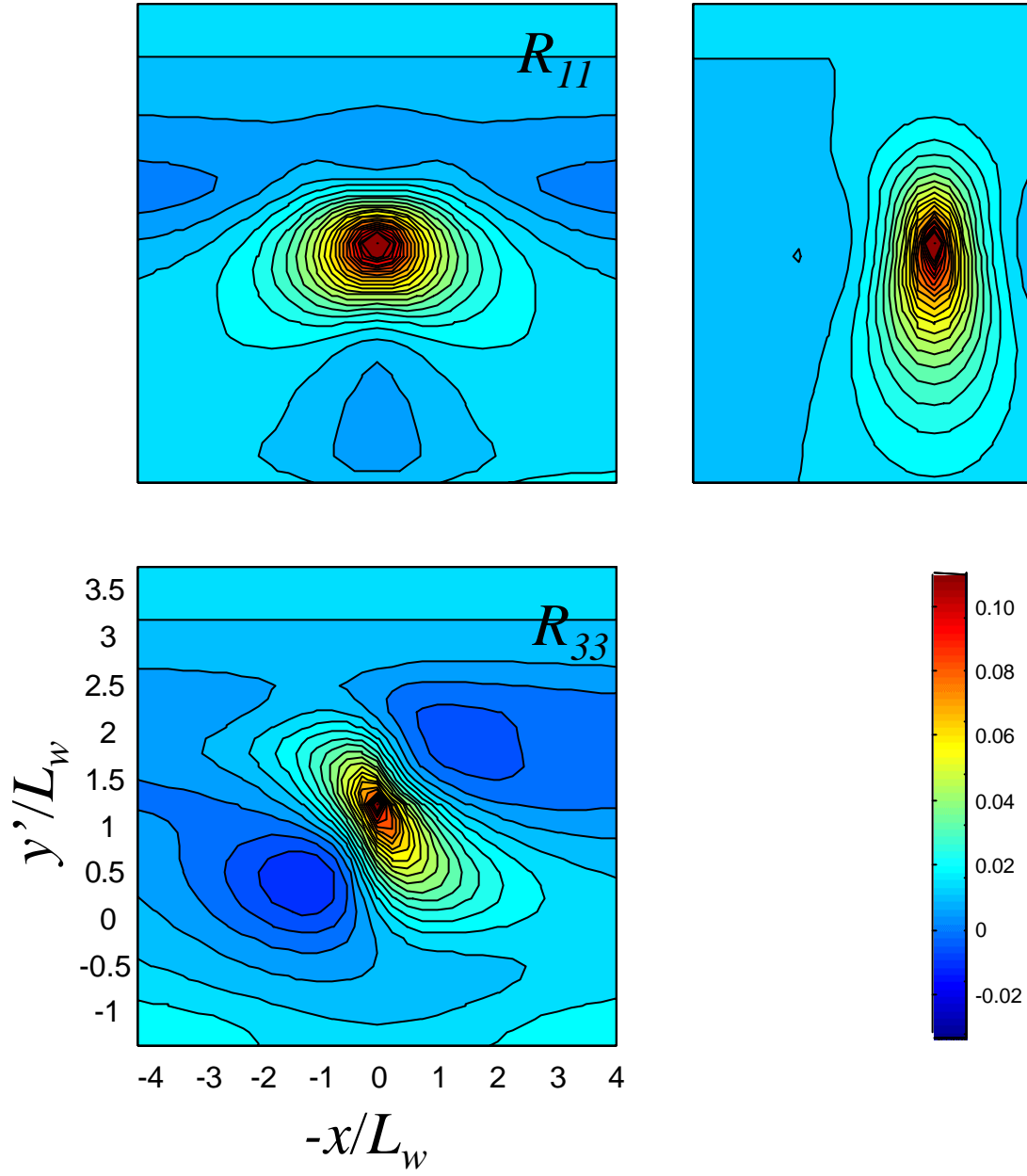
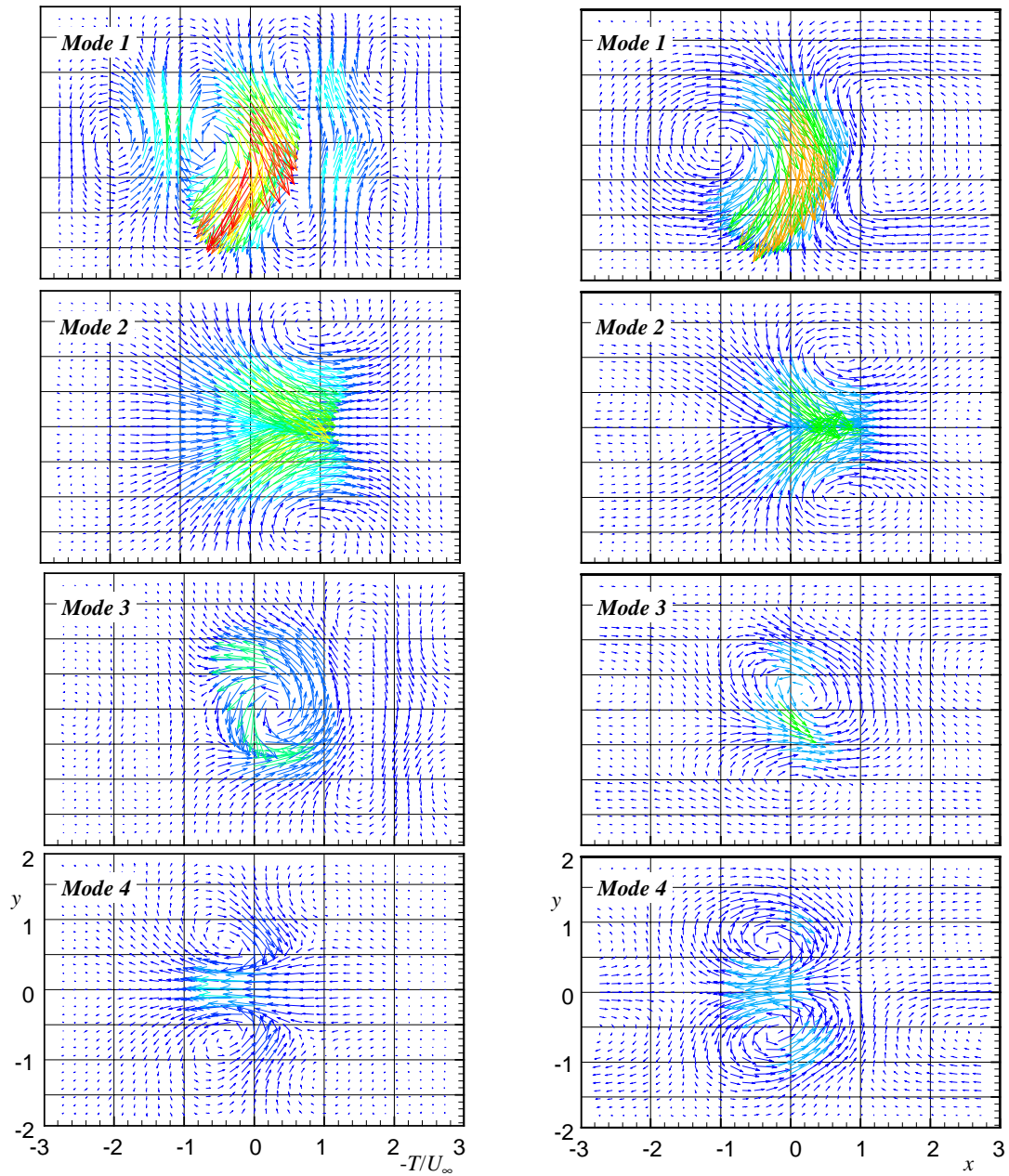


Figure 46. Correlation maps for zero spanwise separation about a fixed probe position of $y/L_w=1.16$: $R_{ij}(1.16L_w, y', 0, x)/U_w^2$ computed using the model.



(a) Deduced from the measured two-point correlation tensor.

(b) Deduced from the model two-point correlation tensor.

Figure 47. Side-by-side comparison of characteristic eddy structures corresponding to the first 4 modes deduced from the measured and model two-point correlation tensors. Distances in inches, $L=0.686''$.